Intrinsic magnetic after effect

Hunter, J.

INTRINSIC MAGNETIC AFTEREFFECT

J. Hunter

Presented in candidature for degree for
Doctor of Philosophy at Durham University,
September, 1973

ABSTRACT

Specimens of the pseudobinary series, $Dy(Co,Ni)_2$, were made in order to investigate the variation in the shape of the hysteresis loop across the series.

A pulsed-field magnetometer was used to obtain oscillograms of the loops and also to derive the ordering temperature and molecular moment for each specimen. Using this data, the variation of critical field with composition was explained and demonstrated by assuming the domain walls in those materials to be very narrow (of the order of ten atomic spacings) and to be intrinsically pinned.

The applicability of the models of thermal activation and, at lower temperatures, tunnelling of the domain wall through the barrier, due to Taylor and also those proposed by Egami were tested by studying the variation of the initial part of the magnetisation curve (i.e., below the critical field at which the magnetisation increases abruptly) with field sweep rate, composition, and temperature.

Measurements of the magnetisation rate, $\frac{dM}{dt}$, were also taken to understand the variation of domain wall mobility with applied field and temperature and hence examine the applicability of Taylor's and Egami's models further.

ACKNOWLEDGEMENTS

I would like to take this opportunity of expressing my appreciation to Professor K N R Taylor for his encouragement, interest and guidance throughout the major part of this work which was carried out under his supervision. I would also like to thank Dr W D Corner most sincerely for helping me to complete this thesis.

My gratitude also goes to the entire Physics Department of Durham University, particularly to Professor G D Rochester, the Head of the Department, and to my colleagues in the Solid State Group for their assistance and for reading my thesis.

Finally, I would like to thank Miss E Kemp and Mr S Bonnington for drawing the diagrams in the thesis, and Mrs B Billinghurst for typing the thesis.

CONTENTS

CHAPTER TWO : DOMAIN WALLS

CHAPTER THREE : EXPERIMENTAL TECHNIQUES

CHAPTER FOUR : EXPERIMENTAL RESULTS

CHAPTER ONE

INTRODUCTION

1.1 A BRIEF HISTORY OF RARE EARTH INTERMETALLIC COMPOUNDS

For more than one and a half centuries the existence of rare earths has been known. During the major part of this time, however, only superficial work was undertaken, due mainly to the unstatisfactory purity of the elements obtained from the wet chemical process then used.

However, with the advent of new techniques, notably the ion-exchange method, more serious investigations into their physical properties have been undertaken on the purer specimens.

After some of the rare earth-cobalt intermetallic compounds were found to be extremely good materials for permanent magnets, applied research into rare earth intermetallic compounds also blossomed.

Numerous workers have been involved in an effort to establish general rules governing the existence and stability of intermetallic compounds. Nevitt (1) has suggested that two of the main aims of research into the metallurgy of intermetallic compounds should be to:-

a) attempt to understand the factors influencing the stability of various phases,

and,

b) associate the structural properties with the bond distribution between atoms.

Many of the above rules have now been discussed at length by Westbrook (2). As the major part of this present study is

concerned with intermetallic compounds, which form in what are known as Laves phases, an outline of these phases is given below.

1.2 LAVES PHASES

The rules governing the formation of the Laves phases were studied by Laves(3), who found the role of atomic radius ratio to be of prime importance in structure determination.

Laves examined the ease with which atoms of different atomic radii may be stacked into different dense structures. The AB_2 phases (A is a rare earth element and B a transition metal) are classic examples of these structures and are represented by three types, namely C14, C15 and C36. These phases occur for radius ratios between 1.1 and 1.3(1).

The existence of compounds of this type is governed primarily by space filling requirements, and it appears that the size ratios play little or no part in deciding which of the three Laves phases will be the most stable(3).

It is now generally concluded that the dominant factor in determining the stable crystal structure is the electronic structure(4). The parameter of importance is the valence electron concentration.

It must be remembered, however, that the difference in energy between structures is small. Consequently, the formation of one phase as opposed to another may be due to second order effects, e.g., the degree of filling of incomplete shells, such as the 3d states in the transition metal compounds, or with the presence of strong magnetic or electrostatic interactions between

the ions.

1.3 MAGNETIC INTERACTIONS

The vast majority of the rare earth intermetallic compounds which have been examined exhibit magnetic ordering over some temperature ranges. In the compounds with non-magnetic elements, such as aluminium and zinc, the Curie temperatures are usually low ($< 100^{\circ}K$), and the only interaction requiring consideration is that between the rare earth ions. When the other component of the compound is a 3d transition metal, as is the case for the compounds in this study, the magnetic ordering temperatures are frequently comparable to that of iron In these cases it is also necessary to allow for the exchange interactions occurring between the transition metal ions and between the transition metal and rare earth ions.

In the following sections these three interactions are briefly outlined separately.

1.3.1 Magnetic Properties of Rare Earths

Before considering the exchange interactions between the magnetic rare earth ions, a review of the magnetic properties of the rare earth family is given below.

The initial member of the family of fifteen elements, known as the rare earths, is lanthanum with atomic number 57 in the periodic table, and the final member, lutetium, is at atomic number 71.

Lanthanum has the electron configuration:-

$(1s^2\ 2s^2\ 2p^6\ 3s^2\ 3p^6\ 3d^{10}\ 4s^2\ 4p^6\ 4d^{10}\ 5s^2\ 5p^6)4f^0\ 5d^{(1)}\ 6s^{(2)}$

where the configuration within the brackets is that of Xenon.

It will be noted that the 4f shell is unoccupied, whereas there is one electron in the 5d shell. This is because the inner 4f shell is at a higher energy than the more extensive 5d orbital.

The 4f shell has an angular quantum number, l, equal to three and therefore has $2(2l + 1)$, i.e., 14 available electron states (seven orbital states and two spin states for each). It is the filling of these states from $4f^0$ for lanthanum to $4f^{14}$ for lutetium that characterises the rare earth series. While this is happening the outer-lying electron states are essentially unchanged and it is for this reason that the rare earth elements are so chemically alike. This is also the reason for the difficulty in separating rare earth elements from aqueous solution as in the wet chemical process mentioned in the initial section.

The parenthesis in the 5d state for the element lanthanum is used to indicate that in many of the elements, once the 4f shell contains electrons, the 5d electron is transferred to the 4f shell. There is also a tendency to retain the stable half- or completely full structure.

The outer $5d^{(1)}$ and $6s^{(2)}$ electrons are readily removed to become conduction elements, leaving a trivalent ion - where the 5d electron has transferred to the 4f shell one conduction electron comes from this shell.

It is the unpaired 4f electrons which give the rare earth

ion its permanent magnetic moment, the magnitude of which is governed by Hund's Rules. These state simply that the magnitude of the moment associated with an incomplete ionic shell is given by (i) an arrangement of the electron spins such that the ion has the maximum number of unpaired electron spins consistent with the Pauli exclusion principle and (ii) a combination of orbital moments to give the maximum value of L allowing for both condition (i) and the exclusion principle. The total moment is then calculated from $\mathcal{J} = L - S$ for a less than half-filled shell and $\mathcal{J} = L + S$ for a more than half-filled shell. Provided that the lowest 4f energy levels of the ions are well separated, the magnetic susceptibility for such a material is given by the relation:-

$$\chi = N^2 g^2 \mu_B (\mathcal{J}(\mathcal{J}+1))/3kT$$

where N is the number of magnetic ions per unit volume, μ_B is the Bohr magneton, g the gyromagnetic ratio, and T the temperature ($^{\circ}K$). If, however, the level splitting is not sufficiently great, then electron excitation into these higher levels will occur, so leading to second or higher terms being necessary. The additional term (then needed) in evaluating the susceptibility has been derived by Van Vleck (4a).

The spin-orbit coupling of the 4f electrons is large ($\sim 10^{\circ}K$) and is at least one order of magnitude greater than the crystal field whose influence is considerably reduced by the screening of the more radially extensive 5s and 5p states. For this reason the metallic rare earth systems can be represented by an assembly of tri-positive rare earth isolated free ions with the crystal field as a perturbation, to a first order approximation.

The rare earths exhibit magnetic ordering over certain temperature ranges. The exchange between ions is not direct, however, as there is little overlap of wave functions for the 4f electrons. The exchange interaction is therefore indirect and is outlined in section 1.3.2.

Neutron diffraction work has shown the configurations of the magnetic moments in such ordered states are quite complex. In the antiferromagnetic phase, the most commonly found configuration is the helical spin structure shown in Figure 1.1. In this ordered state, the magnetic moments of the ions in any one place of the h.c.p. structure are aligned ferromagnetically. The directions of these moments vary from one plane to another by a constant angle, W. It is found that W, the "turn angle" as it is called, increases with temperature. Terbium and dysprosium are good examples of this behaviour.

Applying a magnetic field in the basal plane to this configuration distorts the helix until the field is large enough to cause rotation of those spins in the reverse direction to the field. A further increase in field then brings about the collapse of this "fan" configuration giving saturation when all the spins are aligned in the direction of the field, H (Figure 1.2).

Holmium is similar to both dysprosium and terbium in the antiferromagnetic range, but below the Curie temperature develops a ferromagnetic component of the moment parallel to the c-axis of the crystal, while maintaining the helical structure in the basal plane.

Figure 1.3 shows the zero-field moment configurations of the heavy rare earth metals in the antiferromagnetic and ferromagnetic states.

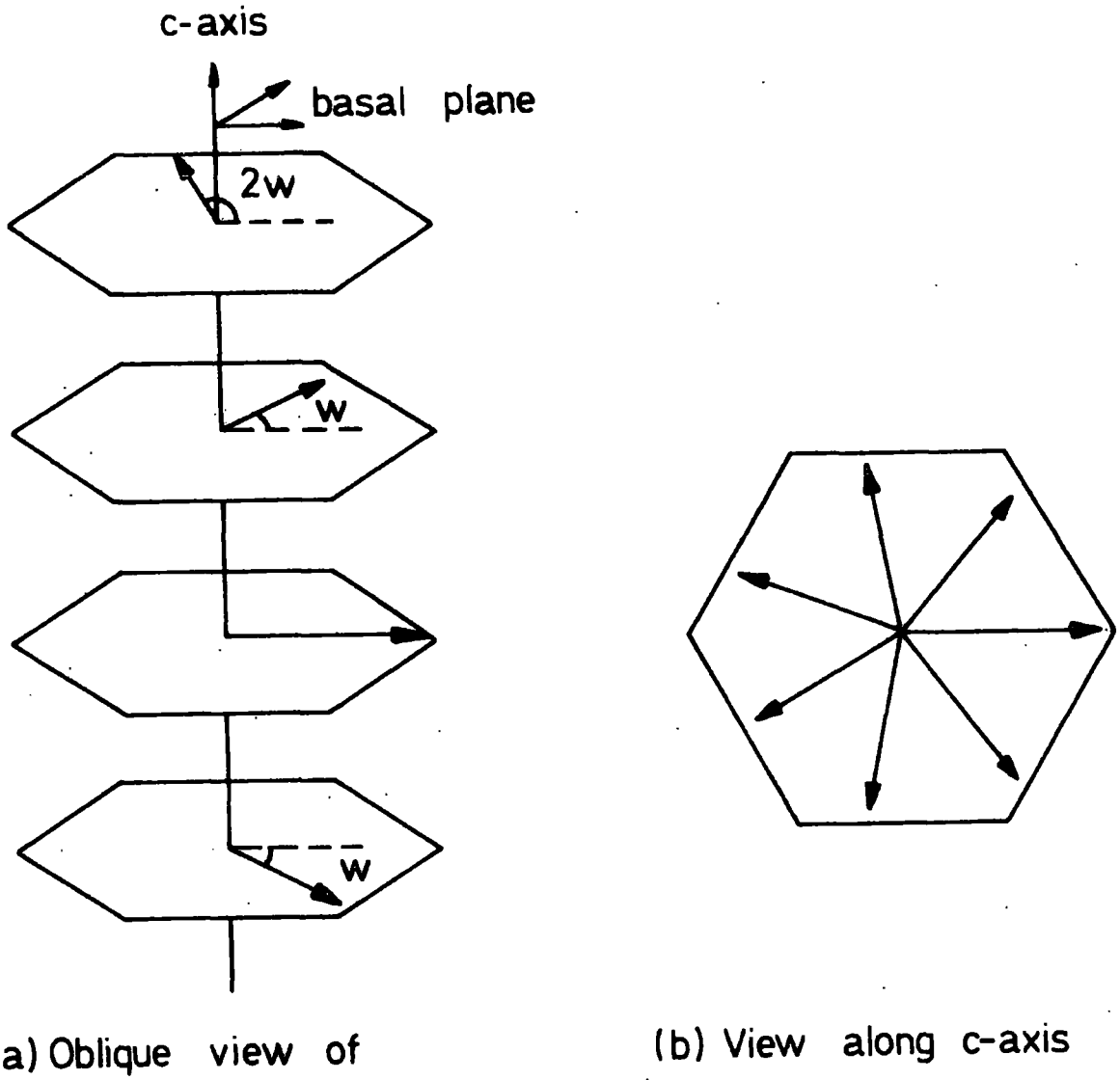

(a) Oblique view of hexagonal plans showing moment directions.

(b) View along c-axis

FIG. 1.1

A simplified view of the helical spin structure, in which the ordering in any plane is ferromagnetic, but the moment direction from plane to plane changes through a constant "turn angle", w, resulting in overall antiferromagnetic behaviour (from Taylor(13)).

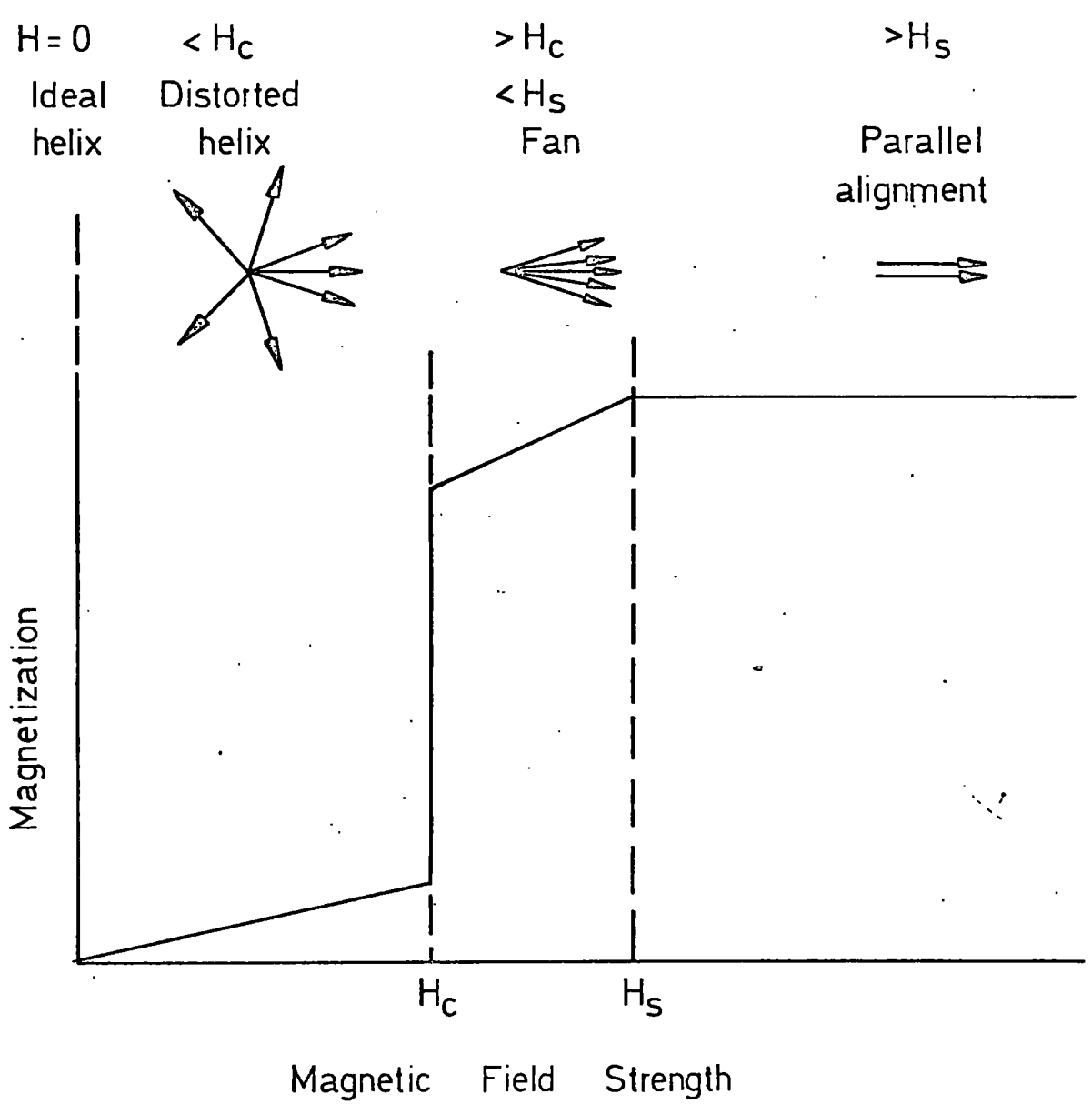

FIG. 1.2

Change in helical structure with applied field (from Taylor(13))

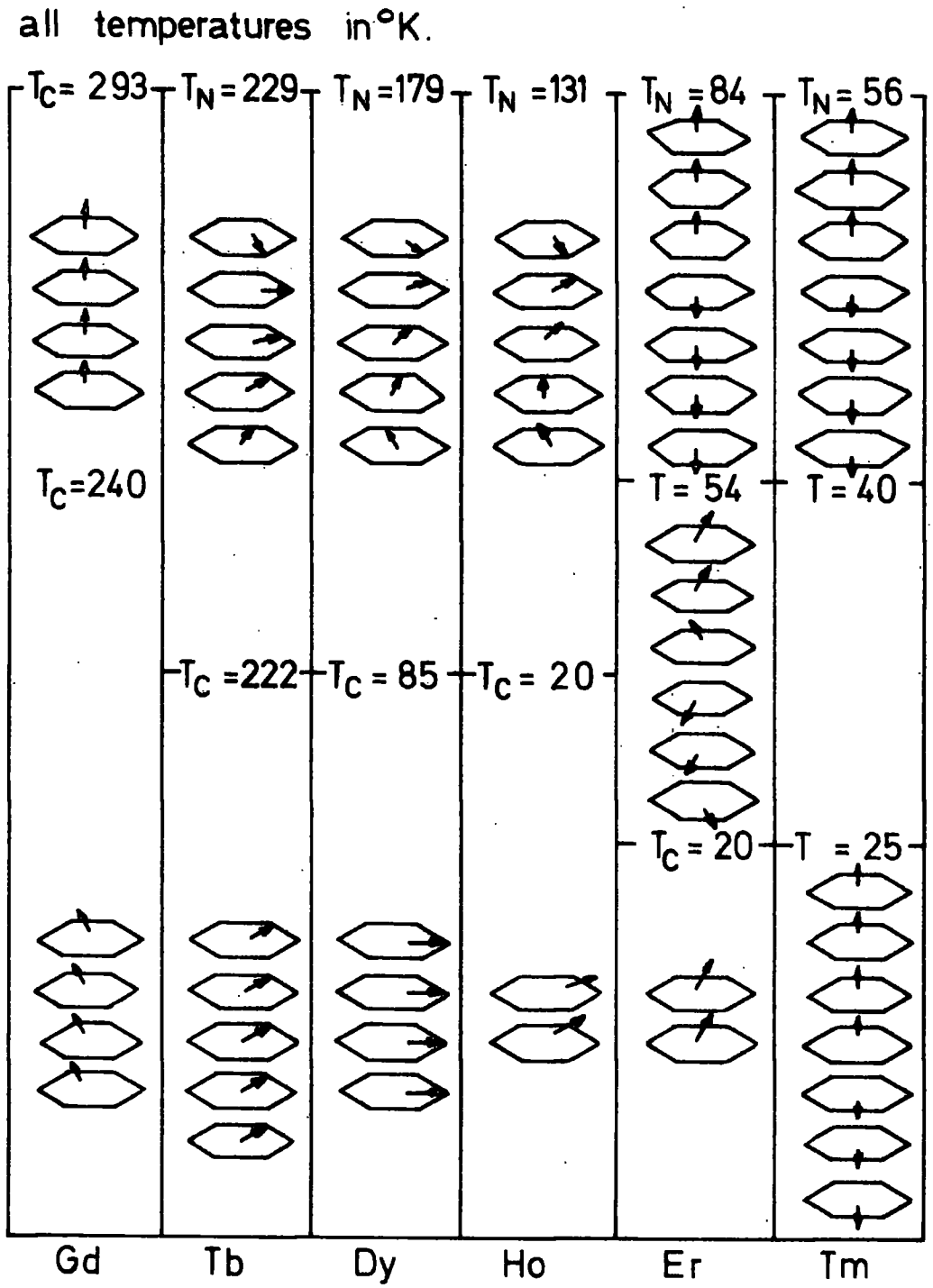

FIG. 1.3

Zero field magnetic structures of heavy rare earth metals and transition temperatures (from Taylor(13)).

The theory of indirect exchange between rare earth ions, which accounts for the wide variety of magnetic spin structures, was originally developed by Rudermann and Kittel(5) in connection with N.M.R. in metals. This theory was subsequently adapted by Kasuya(6) and Yosida(7) and is now frequently referred to on the RKKY theory.

1.3.2 RKKY Interaction

It is the polarisation of the conduction electrons in the rare earth metals which gives rise to the indirect exchange between the ions. These interactions are long-range and have the oscillating nature necessary to account for the helical spin structure outlined previously.

The exchange integral for the interaction between the localised f electrons and the conduction s electrons can be written:-

$$A(\underline{k},\underline{k}^1)i = \sum_{\text{spins}} \int\cdots\int \Big[\chi(\underline{r}^1,\underline{k}) \quad {}_{4f}(\underline{r}_1, \underline{r}_2 \cdots \underline{r}_i \cdots \underline{r}_n) \times \frac{e^2}{|\underline{r}_i - \underline{r}^1|} \chi(\underline{r}_i,\underline{k}^1) \quad {}_{4f}(\underline{r}_1, \underline{r}_2 \cdots \underline{r}^1 \cdots \underline{r}_n) \Big] \times \underline{dr}^1 \, \underline{dr}_1 \cdots \underline{dr}_n$$

where $\chi(\underline{r},\underline{k})$ and χ_{4f} are the wave functions representing the conduction electrons and the electrons in the incomplete 4f shell respectively.

It is usually assumed, for simplicity, that the exchange integral is isotropic and a function of $q = |\underline{k}^1 - \underline{k}|$ only. Further, within the RKKY theory, $A(\underline{q})$ has been taken as a constant, Γ say.

Writing the exchange integral in real space as $A(\underline{r})$ leads to an exchange interaction between the conduction and f electrons of the form

$$\mathcal{H}_{sf} = -A(\underline{r} - \underline{R})\underline{s}.\underline{S}$$

where $\underline{s}$ and $\underline{S}$ are the spins of the conduction electron and ion at $\underline{r}$ and $\underline{R}$ respectively. In an extended zone scheme, and for plane "electron" waves

$$A(\underline{r}) = \sum_q A(q) \exp(i\underline{q}.\underline{r})$$

In the RKKY approximation:-

$$A(\underline{r} - \underline{R}) = \Gamma \delta(\underline{r} - \underline{R})$$

Since $\mathcal{H}_{sf}$ is spin dependent, the conduction electrons of different spin will respond differently to the interaction. For example, if $A(\underline{r}) < 0$, the spin-up electrons have minimum energy in the vicinity of $\underline{S}$ and those of spin down do not. The conduction electrons are therefore polarised. The polarisation, $P(\underline{r})$, is defined as the difference between the densities of spin-up and spin-down electrons and is given by:-

$$P(\underline{r}) = \sum_k f(\underline{k}) \left[|\chi_+(\underline{r},\underline{k})|^2 - |\chi_-(\underline{r},\underline{k})|^2 \right]$$

where $f(\underline{k})$ is the occupancy of the states $\underline{k}$ and the $\chi_\pm$ are the electron wave functions in first order perturbation theory.

Considering the incident electrons as plane waves, we can re-write $P(\underline{r})$ at $T = 0^\circ K$ (thus only states below Fermi level occupied) as

$$P(\underline{r}) = \frac{9\pi}{2\Omega^2} S_z \frac{z^2}{E_F} \int F(2K_f |\underline{r} - \underline{r}^1|) A(r^1) \underline{dr}^1$$

where z is the number of conduction electrons per unit volume

and Ω is the atomic volume, and

$$F(x) = \frac{(\sin x - x \cos x)}{x^4}$$

The RKKY result, with $A(\underline{r}) = \Gamma \delta(\underline{r})$ is then long range and oscillatory, falling off approximately as $1/r^3$ at large distances.

The polarisation $P(\underline{r})$ produced by an ionic spin $\underline{Si}$ at $\underline{Ri}$ interacts with a second spin $\underline{Sj}$ at $\underline{Rj}$ through $\mathcal{H}_{sf}$, and the exchange interaction between the spins is written in second order perturbation theory (within approximations) as

$$\mathcal{H}_{ij} = -\mathcal{J}(\underline{Ri} - \underline{Rj})\, \underline{Si}.\underline{Sj}$$

where $\mathcal{J}(\underline{Ri} - \underline{Rj}) = \sum_q A^2(q)\, \chi(q) \exp\left[iq\,(\underline{Ri} - \underline{Rj})\right]$

In the RKKY model $A(q) = \Gamma$ and

$$\mathcal{J}(\underline{Ri} - \underline{Rj}) = \frac{9\pi z^2 \Gamma^2}{2\Omega^2 E_f} F(2k_f\, |\, \underline{Ri} - \underline{Rj}\, |)$$

This interaction is between ionic spins $\underline{S}$. Now, because of the strong spin-orbit coupling mentioned earlier, $\underline{L}$, the total orbital momentum, and $\underline{S}$, the total spin momentum, cannot be quantised. Instead, the total angular momentum $\underline{J}$ becomes a good quantum number, and we must replace $\underline{S}$ by $(g_J - 1)J$ in the above.

Since $(g_J - 1)$ reverses sign from negative to positive with increasing atomic number in the rare earths, it follows that interactions involving the light and heavy rare earths have opposite sign to the $\mathcal{J}$ between them.

Since $\mathcal{H}_{ij}$ has the Heisenberg form, we may use the molecular field model to give:-

$$K\emptyset p = \frac{3\pi z^2 \Gamma^2 (g_J - 1)^2 \zeta(\zeta + 1)}{\Omega^2 E_f} \sum_{\underline{Ri} \neq \underline{Rj}} F(2k_f | \underline{Ri} - \underline{Rj}|)$$

an expression frequently used to account for the observed paramagnetic Curie temperature ($\emptyset p$).

Of the three magnetic interactions (in rare earth intermetallic compounds), the rare earth - rare earth ion is the weakest. An outline of the stronger interations between transition metal ions and those between transition metal ions and rare earth ions is now given below.

1.3.3 The Direct Interaction

Unlike the rare earth - rare earth interaction discussed above, the direct exchange between the transition metals, due to the overlap of the 3d orbitals, cannot be represented with the same degree of accuracy.

Stoner and Slater(8) suggested that for Fe, Co and Ni the 3d electrons responsible for their magnetism are not tightly bound to any particular nucleus but may move freely from one ion to another through the crystal structure. Whereas this itinerant or "collective electron" model is applicable in that the 3d electron energy levels are broadened into a band which can be split by exchange to give a moment, neutron diffraction has revealed a certain amount of localisation of these moments around the transition metal ions. A compromise between the

electron being localised and being completely free is therefore necessary to account for the magnetisation results of such materials.

An outline of Stoner's theory is, therefore given below, followed by a brief discussion on the modifications necessary to account for the observed anomalies.

If we consider the paramagnetic state in such a system where two sub-bands are equally populated, one of these sub-bands must be displaced along the energy axis (Figure 1.4) to obtain a moment. This moment is due to the transfer of electrons from one sub-band to the other of a lower energy giving an excess of spins in a particular direction.

Let a small number, n electrons/atom, be transferred from the spin - down to the spin-up band. This requires an energy $n\delta E$ per atom, if $2\delta E$ is the energy difference between the two Fermi levels.

As the exchange energy is proportional to the number of electron pairs in each sub-band, the resultant exchange energy is therefore lowered by

$$\left[(p/2 + n)^2 + (p/2 - n)^2 - 2(p/2)^2\right] W = 2Wn^2$$

where W is the average exchange energy per pair of electrons and p is the number of electrons per atom.

If the total energy is lowered when the band is polarised:-

$$2Wn^2 > n\delta E$$

If $N(E_F)$ is the density of states at the Fermi level, then writing $n/N(E_F)$ for δE

$$2WN(E_F) > 1 \quad \ldots\ldots(1)$$

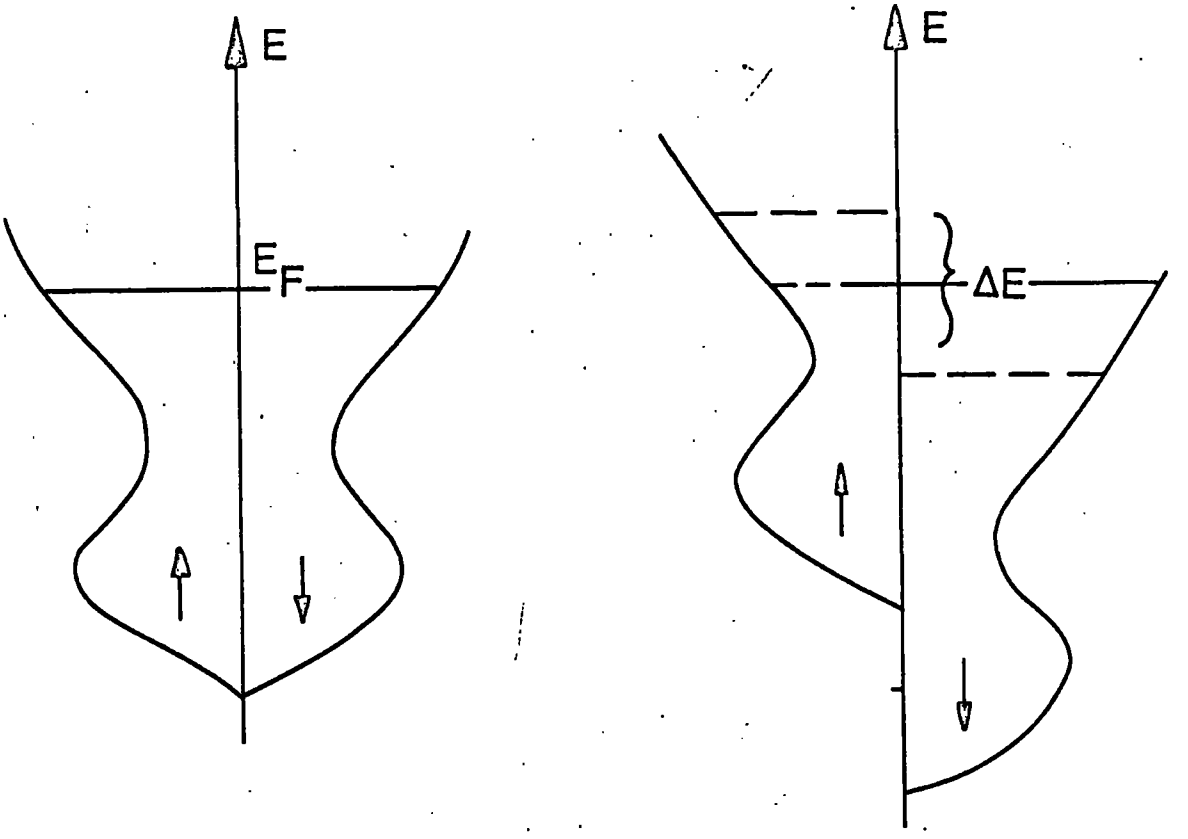

FIG. 1.4

A schematic representation of the splitting of the spin-up and spin-down sub bands of itinerant electron ferromagnet by the exchange interaction (from Taylor(13)).

This is the Stoner criterion for the occurrences of spontaneous moment.

When this inequality holds, one sub-band should begin to fill at the expense of the other until the total energy is a minimum.

It has been found, however, that the electron transfer between sub-bands does not necessarily continue until one sub-band is full, i.e., polarisation may not be complete. This is the case for iron, where the Fermi level of the sub-band is trapped at a minimum in the desnity of states and the molecular field is not large enough to provide the excess energy necessary for E_F to move through this region of low density states.

In this situation in which both sub-bands are intersected by the Fermi level, one obtains:-

$$2W > \frac{1}{\overline{N(E)}}$$

$$\text{where } \overline{N(E)} = \frac{n_o}{\Delta E} = \frac{1}{\Delta E} \int_{E_1}^{E_2} N(E)dE$$

where n_o is the total number of electrons transferred from one sub-band to another, $\overline{N(E)}$ is the average density of states between the equilibrium Fermi levels E_1 and E_2 of the two sub-bands, ($\Delta E = E_1 - E_2$).

Friedel(9) has shown that within the band model it is possible to obtain a situation in which a local moment character may appear to be associated with an ion. He considered the spatial dependence of energy about a transition metal ion and showed that such a polarisation is stable for the condition in equation (1).

In this model it is the excess spin down or deficit spin up electrons in the local populations of itinerant electrons that are of prime importance, and the size of the polarisation regions is comparable to the Fermi wavelength. Surrounding the central region is a region of fringes of spin polarisation of alternating sign, and it was proposed that the appearance of either ferromagnetic or anti-ferromagnetic states will depend upon the details of the overlap of these polarisation regions.

1.3.4 f - d interaction

It is because of the strongly localised character of the 4f electrons and the rather poor 4f - 3d mixing between rare earth (A) and transition metal atoms (B) that the RKKY interaction between them contributes most to the coupling. The rare earth moments as well as the transition metal moments will polarise the conduction electrons by means of an exchange coupling.

With the assumption that the exchange integrals do not depend on $\underline{q}$, one obtains the analytical expression(10):-

$$\mathcal{H}_{A-B} = \left(\frac{3n}{N}\right)^2 \frac{2\pi}{E_F} \mathcal{J}_A(o)\, \mathcal{J}_B(o) \sum_{nm} F(2k_F\, \underline{Anm})\, \underline{S}_n^A\, \underline{S}_m^B$$

where N represents the number of lattice points and 2n the number of conduction electrons. k_F is the $\underline{s}$-band Fermi wave vector, the summation over n and m inolves all A - B distances present in the underlying crystal structure.

The quantity $\mathcal{J}_A(o)$ represents the effective s - f exchange integral, being positive or negative according to the normal exchange integral being larger or smaller than the contributions arising through interband mixing.

$\zeta_{B(o)}$ is the effective s - d integral and, depending on the amount of s - d mixing, may have either sign. As little is known of this quantity in rare earth intermetallic compounds, the above model for A - B coupling can not be tested by comparison with experiment at the present time.

1.4 ELECTROSTATIC CRYSTAL FIELD EFFECTS IN RARE EARTHS

The rare earth metals do not interact with the crystal field to the same extent as the 3d transition metals due to the 4f shell being highly screened, as mentioned earlier. As a result, the spin-orbit coupling dominates, and the crystal field may be treated as a small perturbation on ζ, the total angular momentum, as outlined below.

For an ion with a particular configuration, the spin-orbit energy can be evaluated using the Hamiltonian:-

$$\mathcal{H}_{so} = \lambda \underline{L}.\underline{S}$$

where $\underline{L}$ is the ion's total orbital momentum and $\underline{S}$ its total spin momentum.

The value of λ, the spin-orbit coefficient, can be determined from visible spectra more easily than it can be calculated theoretically. For ground states of ions λ is normally positive if the transition shell is less than half full and negative when it is more than half full.

The addition of $\mathcal{H}_{so}$ to the Hamiltonion removes the independence of $\underline{L}$ and $\underline{S}$, and it is the total angular momentum, $\underline{J}$, of the ion which is quantised. States of equal $\underline{L}$, S, and $\underline{J}$ but different value of quantum number M_J are degenerate for a free ion. The crystal fields which act on rare earth ions in

crystals are too weak to change the magnitude of $\underline{J}$, but it does partially remove the degeneracy of such states. The number of levels which arise from the $2\underline{J} + 1$ degenerate ground state then depends upon the symmetry of the electrostatic field $V_c(\underline{r})$ and can be determined by group theory. It is found that the lower the symmetry of $V_c(\underline{r})$, the greater is the splitting of the levels, and for a given symmetry the magnitude of the splitting depends on the $\underline{J}$ value.

An important restriction in this splitting occurs for ions with an odd number of electrons, which have half-integral values of $\underline{S}$ and hence also of $\underline{J}$. In this case the states always occur in pairs which have the same charge distribution and differ only in the orientation of the magnetic moment. Each pair must, therefore, retain the same energy in an electric field, though they can be split in a magnetic field. This result was proved in a theorem of Kramers (11) and the double degeneracy of such states in an electric field is referred to as "Kramer's degeneracy".

Another general theorem from group theory which is invaluable in the understanding of the lowest energy level structure is the Jahn-Teller effect. This states that the environment of an ion with a degenerate ground state, Kramer's doublets excepted, spontaneously distorts to a lower symmetry so as to remove the degeneracy. It implies that ions with an even number of 4f electrons always have singlet ground states. This rule does not apply to the excited state.

1.5 AB_2 COMPOUNDS (A = rare earth; B = transition metal)

Most of the work undertaken in this study is concerned

with the magnetic properties of the pseudo-binary systems based on $DyCo_2$ and $DyNi_2$. For this reason a brief review of the properties of the AB_2's is given below.

From investigations of phase diagrams it is apparent that rare earths only form compounds with the 3d transition metals to the right of chromium in the periodic table. Of these, the most common stochiometry is that of the AB_2's.

The majority of these compounds form in the cubic (C15) Laves phases. The appearance of the Laves phase depends upon size filling considerations and the stable phase is determined by valence electron concentration effects, as mentioned in section 1.2.

The results of early work by Vickery (12) on the magnetic properties of the Gd/Co series showed a deep minimum in the magnetisation versus composition graph. This infers a ferrimagnetic coupling between the ions for the heavy rare earth compounds, whereas a ferromagnetic coupling was observed in the light rare earths.

In the nickel compounds, however, the saturation magnetisation has been taken to infer that the Ni ion in such compounds carries no moment.

The moment of the Co ion in such compounds has been shown by experiment to be approximately $1{\cdot}0\mu_B$. For heavy rare earths this is coupled antiferromagnetically to the rare earth moment, whereas for such compounds as $PrCo_2$, $NdCo_2$ and $SmCo_2$ they appear to be ferromagnetically coupled. This reversal in the sign of the coupling is understood in terms of an antiferromagnetic coupling of the spin angular momenta of the rare earth and transition metals, since for heavy and light rare earths we have

$\underline{J} = \underline{L} + \underline{S}$ and $\underline{\mathcal{J}} = \underline{L} - \underline{S}$ respectively (Figure 1.5).

The absence of Ni moment in compounds and the reduced moment values associated with Co compounds were originally attributed to the filling of the localised 3d states by electron transfer from the rare earth. More recent studies, however, show that it is not valid to only consider the core polarisation in the crystal field calculations.

Studies of various pseudo binary systems by Piercy and Taylor (13) indicate a non-linear variation of the transition metal moment with composition in systems such as $(Dy_{1-x}\ Y_x)Fe_2$ and $Gd(Co_{1-x}\ Ni_x)_2$. In both these series the moment of the transition metal ions changes appreciably over a small composition range - a fact which is hard to justify on the basis of electron transfer to localised 3d states. Piercy and Taylor proposed that the 3d states of the Fe, Co and Ni atoms in these compounds form a band which gives rise to an itinerant electron moment.

A simple model of the antiferromagnetic coupling of the spins of the rare earth-transition metal ions has been given by Wallace (14) and follows from the known sign of interaction between the f and d electrons with the conduction electrons.

Following work by Jaccarino et al (15) on RAl_2's, it is known that the conduction electron polarisability due to a rare earth ion is negative with respect to the spin of the ion at the ion site in the lattice and also negative at the neighbouring transition metal sites. Since in these Laves phase compounds the A - B and A - A distances are comparable, one can assume that the polarisation is also negative at the neighbouring rare earth sites and will give rise to a ferromagnetic rare earth sub-lattice.

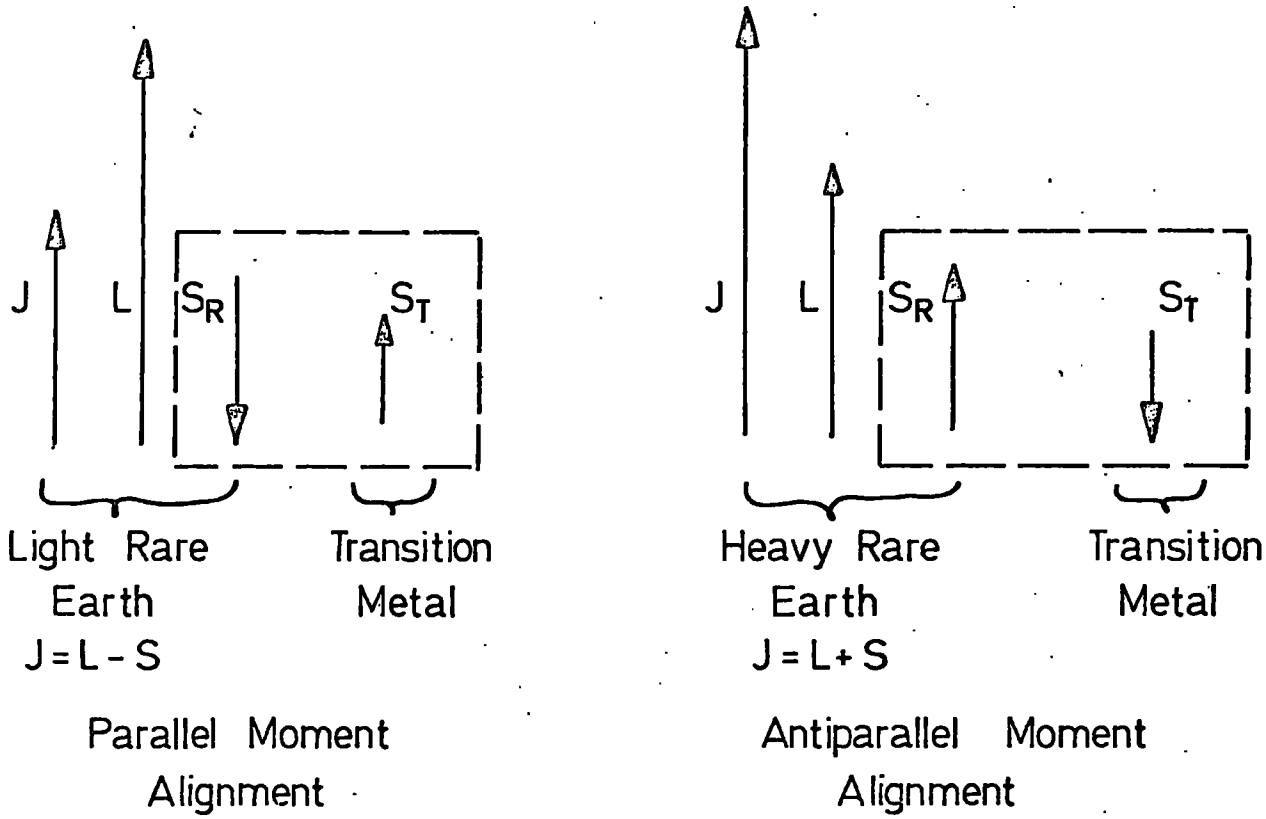

FIG. 1.5

A simple view of the relative spin orientations in the rare earth-transition metal compounds (from Taylor(13))

Wallace then treats the S - 3d interaction as positive; under these conditions the spins of the Fe or Co ions, which lie at sites equivalent to the A1 ions in $RA1_2$, will be aligned in Figure 1.6, from which it is evident that this coupling mechanism will lead automatically to ferromagnetism in the light rare earth compounds and ferrimagnetism in those formed with heavy rare earth elements.

1.6 MAGNETIC TRANSITIONS IN RARE EARTH INTERMETALLIC COMPOUNDS

As the exchange energy is small and oscillatory in the rare earth intermetallic compounds, their magnetic structures may be either ferromagnetic or anti-ferromagnetic. Furthermore, as a consequence of the high anisotropy in these materials, their domain walls are very narrow.

The magnetic transitions in the anti-ferromagnetic materials, e.g., A_3B's have been found to be caused by spin-flip, spin-flop processes, Feron(16), Taylor et al(17). For some materials, however, there has been some ambiguity over which processes are involved in the transitions. For example, Barbara et al(18) initially explained the metamagnetic transition obtained in Dy_3Al_2 in terms of anti-ferromagnetic-ferromagnetic transitions. Buschow(19), however, has shown that the observed transition is due to the high anisotropy of the material. Subsequently, Barbara et al(20) have re-interpreted their results following Buschow's approach.

Zijlstra(21) and Egami(22) have investigated materials with narrow domain walls theoretically. A resumé of Zijlstra's theory is given in Chapter 2, where it is shown that there is an intrinsic energy barrier to domain wall motion in these

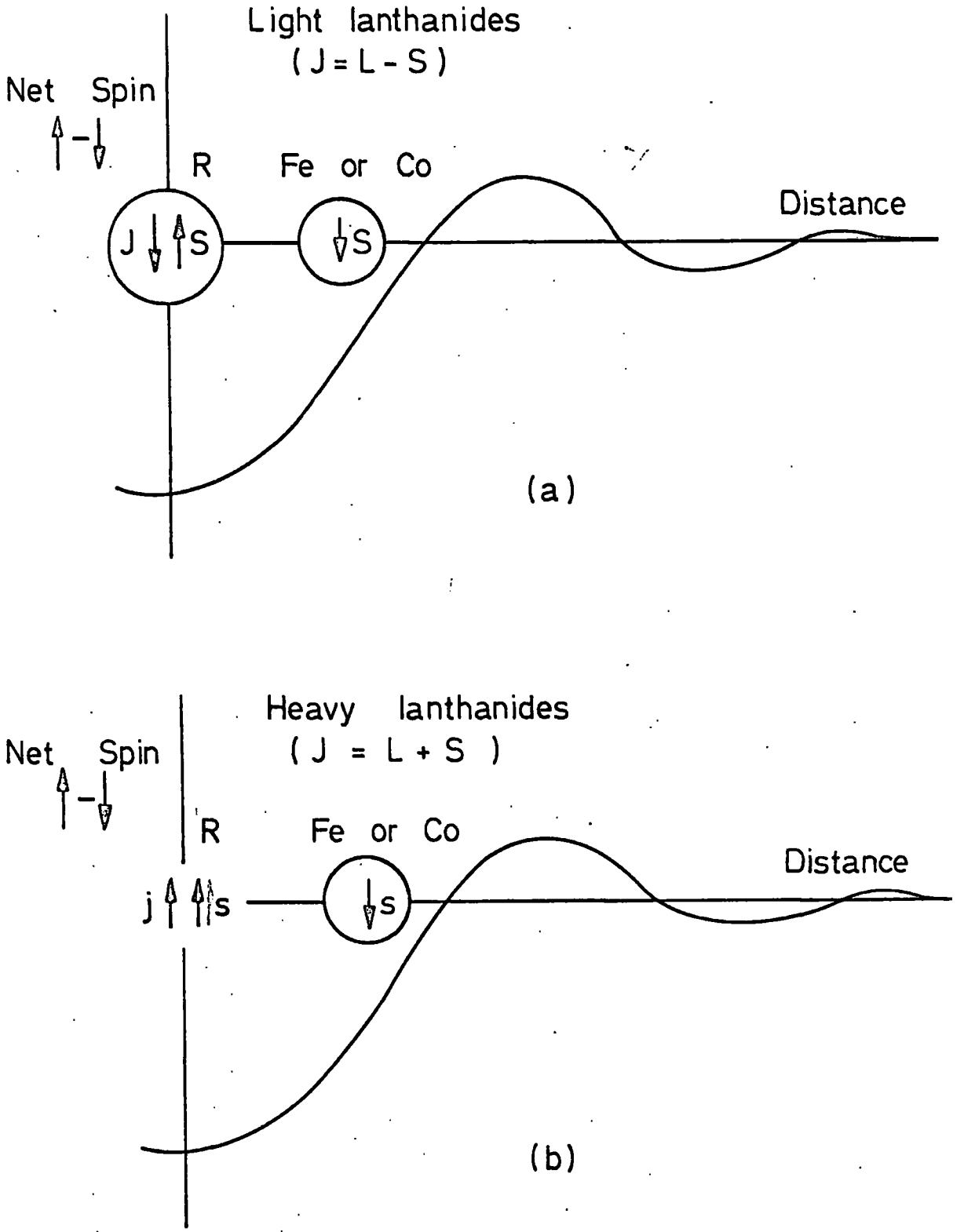

FIG. 1.6

A pictorial view of the rare earth-transition metal interaction occurring by way of the conduction electrons for (a) light rare earth elements, and (b) heavy rare earth elements (from Taylor(13)).

materials, which manifests itself as an intrinsic coercivity.

1.7 INTRINSIC MAGNETIC AFTEREFFECT

During investigations on the pseudobinary series Dy $(Co,Ni)_2$, Taylor(23) observed that the magnetisation did not increase appreciably below a critical field. Once the critical field had been passed, however, he noticed that the magnetisation increased much more rapidly and that the magnetisation was time dependent. Taylor called this effect the magnetic after-effect. He found that not only did the critical field depend upon the composition of the specimen in the series but also upon the rate at which the field was applied. The phenomenon has since been explained using Zijlstra's narrow domain wall theory.

While it appeared an unusual phenomen three years ago, it is now clear that many rare earth compounds exhibit these effects associated with narrow domain walls. Further experimental studies(24, 25) have shown that the intrinsic coercivity of these materials does not completely pin the domain wall but reduces its mobility. Egami(22) has drawn the parallel between the present situation and that of dislocations pinned by the Peierl's potential. Using this analogy, Egami has postulated(26) that the process which governs the increase in magnetisation at lower temperatures is due to quantum mechanical tunnelling, whereas for higher temperatures the domain wall is thermally activated so that it may move from its pinning site.

Taylor(24) and Egami(27) have used different expressions to describe the thermal activation process.

Taylor predicts a linear dependence between the magnetisation rate and the applied magnetic field and also a dependence upon the reciprocal of the absolute temperature, i.e.,

$$\frac{dM}{dt} \propto f(\frac{H}{T}),$$

whilst Egami expects the magnetisation rate to be dependent upon the reciprocal of the applied field and temperature for the thermal activation process, i.e.,

$$\frac{dM}{dt} \propto f(\frac{1}{HT}).$$

Further, whereas Egami has predicted a dependence upon the reciprocal of the applied field squared, i.e.,

$$\frac{dM}{dt} \propto f(\frac{1}{H^2}),$$

for the tunnelling process at low temperatures, Taylor, Barbara et al have found that for these low temperatures the results are described by the relationship:-

$$\frac{dM}{dt} \propto f(\frac{1}{H}).$$

1.8 AIM OF THIS STUDY

From oscillograms of magnetisation against applied field, the resulting critical field and its variation across the series of the compounds $Dy(Co,Ni)_2$ is investigated using a pulsed-field magnetometer.

Using the theory, due to Zijlstra, of narrow domain walls as outlined in Chapter 2, the critical fields inherent

in these materials are explained in terms of the domain wall being instrinsically pinned. The variation of the critical field with composition is explained in terms of the changing size of energy barrier to domain wall motion due to the variation in the ratio of anisotropy to exchange energy constants across the series.

The processes governing the magnetisation and the domain wall mobility at fields below the critical field are also investigated by taking measurements of the magnetisation rate of DyCoNi at various sweep rates and temperatures. Using this information the models proposed by Taylor and Egami are tested and the results compared.

CHAPTER TWO

DOMAIN WALLS

2.1 DOMAINS

It was in 1907 that Weiss (28) first conceived the idea that a ferromagnetic material is divided into domains. The transition layer which separates two adjacent domains was studied by Bloch(29), one type of transition layer now being referred to as a Bloch wall, and later by Landau and Lifschits(30) and many other workers.

It was found that there is not a discontinuous change between domains but a transition region where the change in orientation of adjacent spins occurs gradually. The thickness of this layer is governed primarily by the balance between the exchange energy, E, which favours thick walls and the anisotropy energy, K, which conversely favours thin walls.

The origin of magnetocrystalline anisotropy in the transition metals is not yet well understood because of the itinerant nature of the magnetic moment. The situation for rare earths is much clearer, however, where the result of the strong spin-orbit couplin is to bind the magnetic moment to the orbital momentum. The effect of the crystal field on the rare earth ion then depends on the ion's orientation, i.e., the large magnetic anisotopies of the rare earths come directly from the crystal field.

In many ferromagnetically ordered materials based on rare earths, large coercive forces with open hysteresis loops have been obtained. This effect has been attributed to these materials having narrow domain walls.

Trammel(31) was the first to point out that domain walls in such materials could be very narrow and in these circumstances

the normal treatment with spin direction changing continuously through the domain wall is no longer valid (section 2.2).

Egami(22), Zijlstra(32) and Barbara et al(24) have shown that in such materials a finite energy is required to move the domain wall through such a material, and this would manifest itself as a large "intrinsic coercivity".

Further, Taylor et al(25) have shown that certain materials display a "magnetic after-effect" and have attributed this to the magnetisation process associated with the thin walls.

A resumé of the classical continuum approach used for calculating the spin configuration and energy of a Bloch wall is given in the next section (for a review of this approach, see Kittel(33)). It is followed by the treatment, due to Van den Broek and Zijlstra(21), for materials with narrow domain walls.

2.2 CLASSICAL CONTINUUM APPROACH

If we assume the ferromagnetic material to be composed of magnetic ions of one kind only, which are strictly localised, we may write the exchange energy, e_{ij}, between neighbouring ions (it is further assumed that the exchange is short range):-

$$e_{ij} = EV(1 - \cos\Delta\phi_{ij}) \quad \ldots\ (1)$$

Where E is the exchange constant, $\Delta\phi_{ij}$ the angle between the ith and jth spins, and V is the volume available per magnetic atom.

If the material has uniaxial symmetry, the anisotropy energy, e_i, is then (taking only the lowest order term):-

$$e_i = KV \sin^2\phi \quad \ldots\ (2)$$

where ϕ_i is the angle between the spin and the reference axis, which is taken to be the easy axis of magnetisation.

The magnetic atoms are arranged in rows perpendicular to the easy axis and in planes perpendicular to the rows. A domain wall, in such a case, is a configuration where the magnetic moments within a plane are parallel to each other but with an orientation that differs from plane to plane. It is sufficient, therefore to discuss only a row of magnetisations (Figure 2.1) as the coupling in a plane can be taken as a constant.

If we adopt the continuum approximation, i.e., the angle between two neighbouring spins is assumed small, then

$$\Delta\phi = a \frac{\delta\phi}{\delta x} \quad \ldots\ldots (3)$$

where a is the distance between neighbouring spins.

By integrating the anisotropy energy and exchange energy from $x = -\infty$, $\phi = 0$ to $x = +\infty$, $\phi = \pi$ (for the 180° wall) the energy of the wall E_w is found to be

$$E_w = a\sqrt{8EK}$$

The angle between neighbouring moments at the centre of the wall is given by

$$\phi = \sqrt{\frac{2K}{E}}$$

It is apparent, therefore, that if the value of K approaches that of E, then $\Delta\phi$ can assume large values and in these cases the continuum approximation is no longer valid.

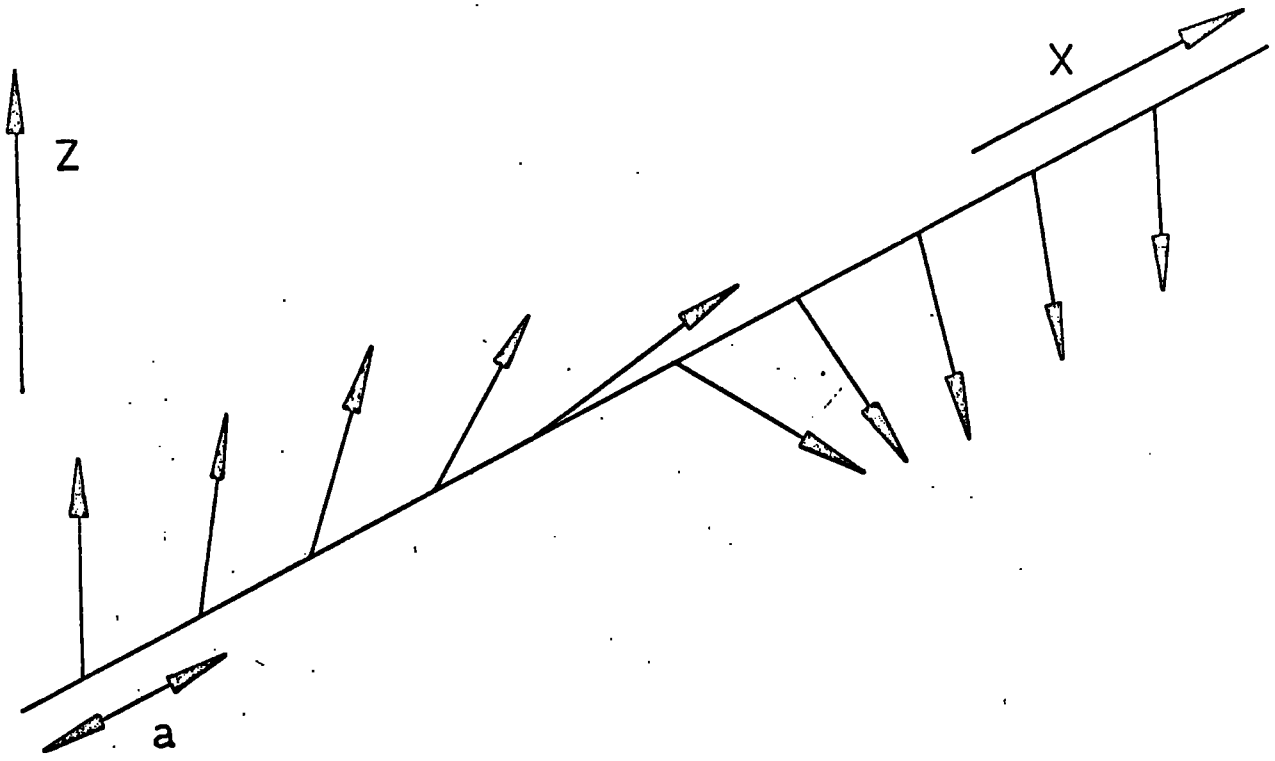

FIG. 2.1

Spin configuration along row of spins in 180° domain wall. Easy axis along Z direction (from Zijlstra(21)).

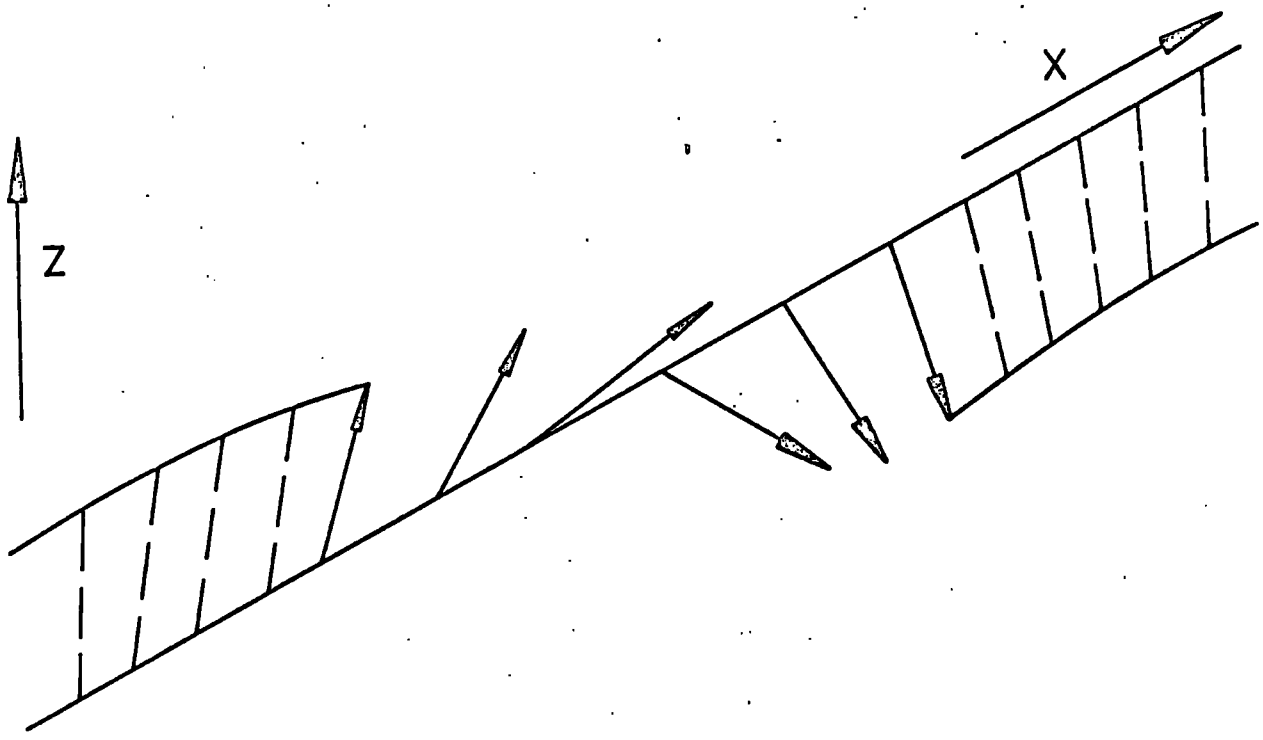

FIG. 2.2

Domain wall model consisting of centre part with discrete spins between two continuous zones (from Zijlstra(21)).

2.2.1 Domain Wall Mass

The existence of this parameter was first demonstrated by Döring(34). He showed that, to a reasonable approximation, the moving domain wall differed in energy from the wall at rest by a term due to demagnetising effects which are proportional to the square of the velocity of the wall, i.e., v^2. He was therefore able to identify this as a kinetic energy term, and he defined the constant of proportionality as one half the mass of the wall.

The demagnetising field, H_D, is a result of the spins in the wall with angles other than 0° or 180° to the domain wall precessing about the applied field, giving a component of magnetisation normal to the wall.

Kittel and Galt(35) have shown that the effective mass per square centimeter of a Bloch wall is given by:-

$$m = \frac{1}{2\pi\delta_w^2} \sqrt{\frac{K}{E}}$$

where δ_w is the wall energy density.

Therefore the effective mass of a Bloch wall is inversely proportional to its thickness. As a result, the effective mass for the Bloch walls in the materials under consideration will be appreciable.

2.3 INTRINSIC WALL PINNING

Van den Broek and Zijlstra (21) considered the discrete nature of the magnetic moments in materials with a large K/E ratio, by assuming the wall to be composed of three regions : a central region, where the spins change appreciably from moment to moment, bounded by two continuous zones where there is a small change (Figure 2.2) in spin between neighbouring ions.

Figure 2.3 shows two possible configurations viewed perpendicular to the wall. In case (b) the central spin is orientated perpendicular to the easy direction. As a result the wall in this position has a higher energy than when it is in position (a), and is therefore energetically unfavourable. As such configurations occur periodically through the crystal there will be an inherent energy barrier to the movement of a wall, even through a perfect crystal. This gives rise to the phenomenon known as "intrinsic wall pinning" and will result in the material having an "intrinsic coercivity".

2.4 ENERGY BARRIER TO DOMAIN WALL MOVEMENT IN PERFECT CRYSTALS

In this section the two configurations of a 180° domain wall will be considered; the first is the equilibrium configuration in the absence of a magnetic field (Figure 2.3(a)), and the second is the case in which the central moment is perpendicular to the easy direction (Figure 2.3 (b)). The difference in energy between these two configurations is then the energy barrier to domain wall movement.

The total energy of the wall E_w is determined by adding the energy of the two continuous zones to that of the discrete

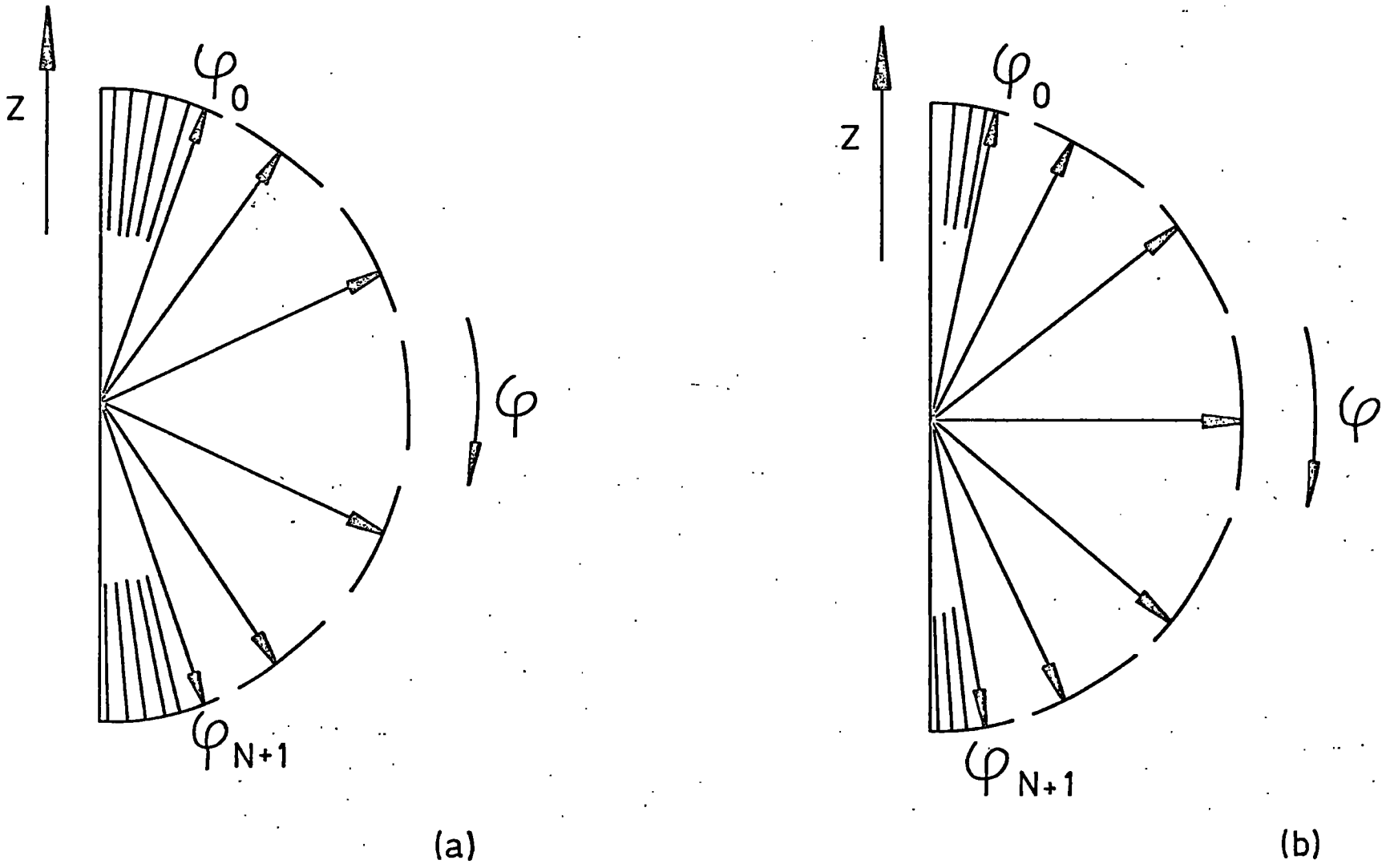

FIG. 2.3

View along row of spins perpendicular to domain wall. (a) Centre of wall between two spins; (b) centre of wall at spin site. Shaded sectors indicate continuous zone (from Zijlstra(21))

moment zone.

The energy for the first continuous zone from $x = -\infty$, $\phi = 0$, to $x = x_o$, $\phi = \phi_o$ is obtained from equations (1), (2) and (3) using variational calculus, giving:-

$$E_w(\phi_o) = a\sqrt{2EK}\ (1 - \cos\phi_o)$$

For a wall with N discrete moments in between two continuous zones in the range $0<\phi<\phi_o$, and $\phi_n + 1<\phi<\pi$, then, writing $q = \frac{K}{E}$,

$$E_w = aE\left[\sqrt{2q}\ (2-\cos\phi_o + \cos\phi_{N+1}) + \frac{q}{2}\ (\sin^2\phi_o+\sin^2\phi_{N+1})\right.$$

$$+ \sum_{i=1}^{N}\left(\left\{q\ \sin^2\phi_i + 1 - \cos(\phi_i - \phi_{i-1})\right\}\right.$$

$$\left.\left.+\left\{1 - \cos(\phi_{N+1} - \phi_N)\right\}\right)\right] \quad \ldots\ (4)$$

To find the most stable configuration, given the boundary conditions, the total energy of the wall must be minimised, giving the equations:-

$$\frac{1}{aE}\frac{\partial E_w}{\partial \phi_o} = \sqrt{2}\ \sin\phi_o + \frac{q}{2}\sin 2\phi_o - \sin(\phi_1-\phi_o) = 0 \ \ldots\ (5)$$

$$\frac{1}{aE}\frac{\partial E_w}{\partial \phi_i} = q\ \sin 2\phi_i + \sin(\phi_i - \phi_{i-1}) - \sin(\phi_{i+1} - \phi_i) = 0 \ \ldots\ (6)$$

$$(i = 1, 2, 3 \ldots N)$$

$$\frac{1}{aE}\frac{\partial E_w}{\partial \phi_{n+1}} = -\sqrt{2q}\ \sin\phi_{N+1} + \frac{q}{2}\sin 2\phi_{N+1} + \sin(\phi_{N+1} - \phi_N)$$

$$= 0 \ \ldots\ (7)$$

By using a trial value of ϕ_o in equation (1), a value ϕ_1

can be found which, with equation (2), yields ϕ_2, ϕ_3 ... ϕ_{n+1}. When the values ϕ_n, ϕ_{n+1} satisfy equation (3) it shows the initial value of ϕ_o to be correct, otherwise another value of ϕ_o must be tried in a similar manner.

In contrast to the previously outlined continuum approximation, the above calculations lead to the conclusion that the angle between central moments tends to 180° for $q \longrightarrow \frac{2}{3}$. This wall has been called a ferro-electric wall by analogy.

The increase in energy of such a wall when the central moment is perpendicular to the easy direction is shown in Figure 2.4, as a function of q. It is this periodic energy barrier which must be overcome for the wall to move through the crystal, hence these crystals have "intrinsic coercivity".

If we try the assumption that the barrier has a simusoidal form and that its height is not influenced by an applied field, we can write:-

$$E_w = E_{wo} + \frac{\Delta E}{2} \sin\left(\frac{2\pi x}{a}\right)$$

The coercive force is then:-

$$H_c = \frac{1}{2M_s}\left(\frac{\partial E}{\partial x}\right)_{max} = \frac{\pi}{2aM_s}\Delta E$$

where M_s is the saturation magnetisation per unit volume.

2.5 INTRINSIC COERCIVITY

If an external magnetic field is applied along the easy axis of a material such as described above, the moment-angle distribution in the wall will become asymmetric.

In calculations of the energy of the wall, therefore, an

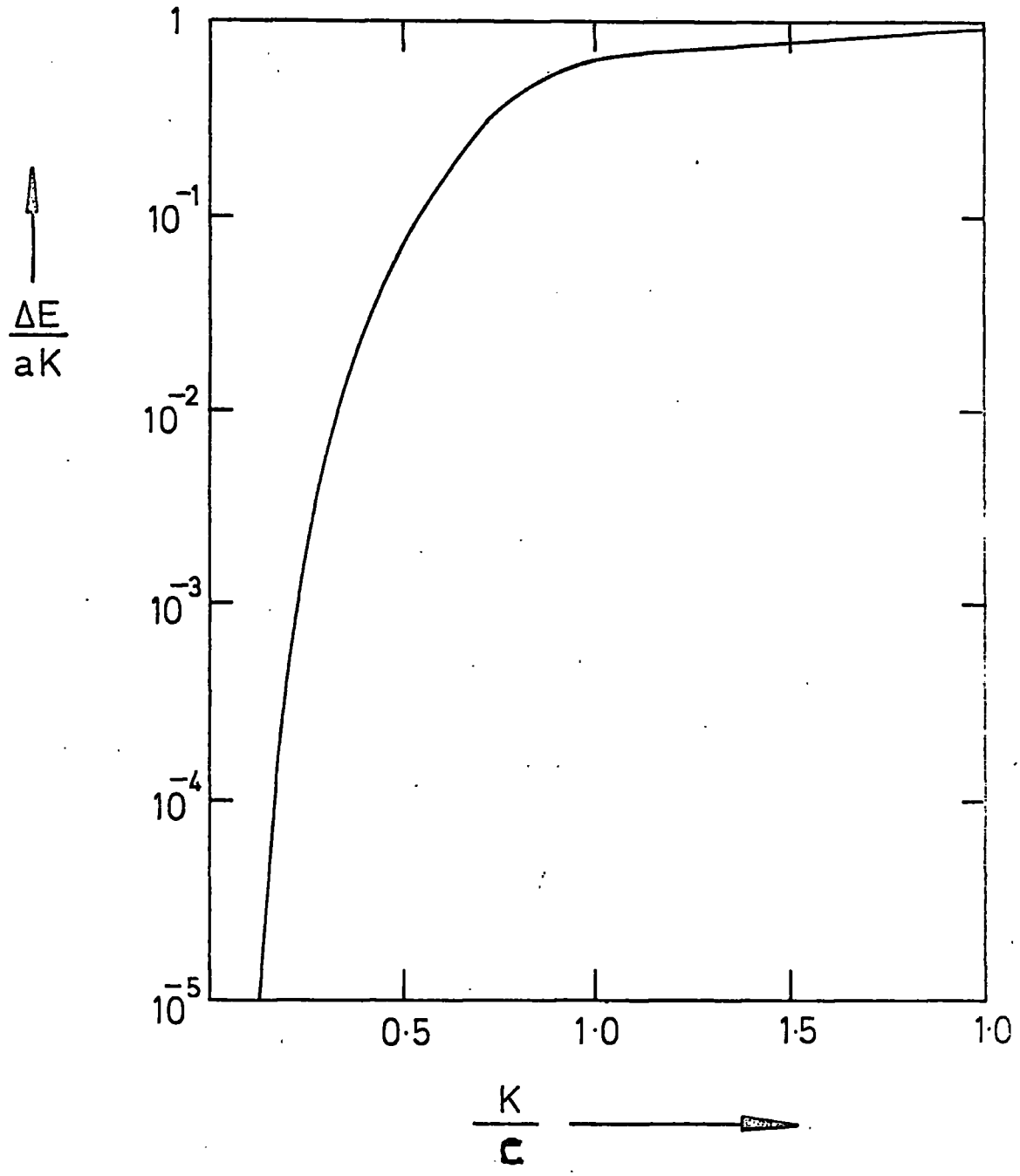

FIG. 2·4

Variation of energy difference between configurations of FIG 3(a) and 3(b) as a function of K/C. Energy measured per unit volume (from Zijlstra(21)).

extra term $e = H\ I\ V\ (1 - \cos \phi_i)$ due to the magnetostatic energy per discrete moment must be added to equation (4). It can be shown that the energies of the continuous zones are now, apart from a magnetic term, independent of angles

$$E_W = aE\sqrt{q\frac{(1 \pm L)}{2}}\ (\Delta \phi)^2$$

where $\Delta\phi$ is the acute angle between the first (or last) discrete moment and the easy axis, $h = H/H_A$, the reduced field strength, the anisotropy field $H_A = \frac{2K}{M_s}$.

However, this modification hardly affects the problem when a sufficiently large number of the discrete moments is considered. The important modification in equation (4) is that an extra term is added, viz.,

$$aE\left[\sum_{i=1}^{N} q\left\{2hq(1 - \cos\phi_i)\right\} + hq\left\{2 - \cos\phi_o - \cos\phi_{N+1}\right\}\right]$$

The only new parameter is that of h. As h varies, so does the wall configuration. However, when h reaches a critical value, no solution other than the trivial one in which all spin orientations are zero is obtainable. Physically, this means there will be no wall present in the material. It is, therefore, reasonable to interpret this critical value of h as the intrinsic coercivity of the perfect crystal.

Figure 2.5 shows the reduced coercivity as a function of q. It can be seen that $h_c \longrightarrow 1$ ($h_c = H_c/H_A$ where H_c is the coercive force) as $q \longrightarrow \infty$ in this case $K \longrightarrow \infty$ and becomes unimportant, and the individual moments are expected to reverse when the field attains a value equal to H_A, the anisotropy field.

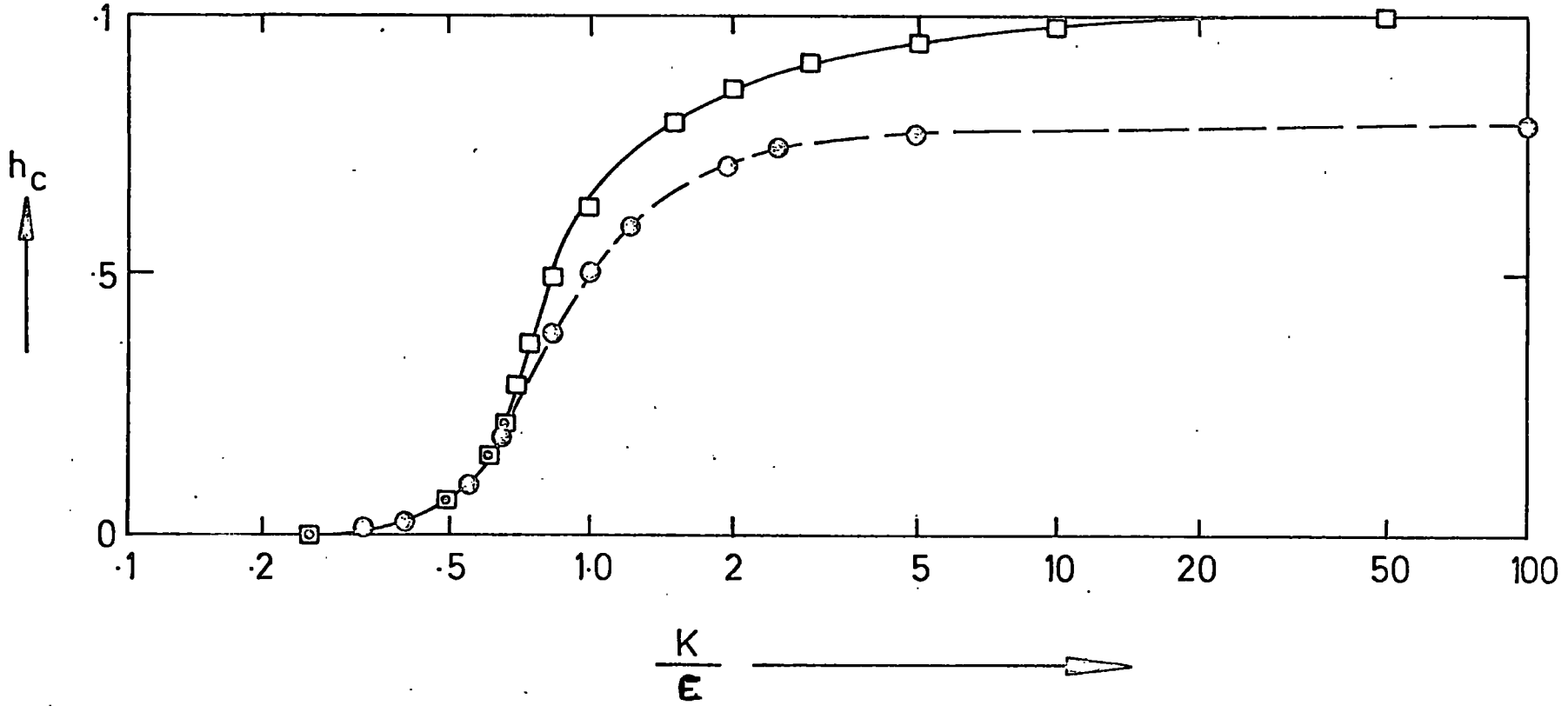

FIG. 2·5 Reduced coercivity as a function of K/ε. --- Ignoring the field influence on moment angle; —— taking the field influence into account (from Zijlstra(21))

CHAPTER THREE

EXPERIMENTAL TECHNIQUES

3.1 SPECIMEN PREPARATION

The specimens used in this investigation were made by melting together stochiometric quantities of their components in an arc furnace.

The elemental metals were obtained from Koch-Light with stated purities of 3 N's and 4 N's for the rare earth and transition metals respectively.

After weighing each component to within an accuracy of ± 0.5 mg, they were placed near to each other on the water cooled copper hearth of an arc furnace. The furnace was then evacuated, to a pressure of the order of 10^{-3} torr, and subsequently filled with an atmosphere of Purargon (Argon with less than 3 p.p.m. Oxygen). After re-evacuating, the chamber was again filled with Argon to a pressure of 300 torr. This procedure was followed to reduce the amount of Oxygen in the chamber, which would otherwise oxidise the components on melting. This amount was further reduced by melting a button of Tantalum (as a getter) for half a minute or so before the specimen melting.

Having reduced the oxygen content, the components were melted together. The melt was performed at as low a temperature as possible in order to reduce loss due to evaporation.

The resulting flat-bottomed button was reversed and remelted several times to ensure complete homogeneity.

To anneal the specimens they were wrapped in Tantalum foil and placed at intervals along a quartz tube. The quartz tube

was pumped out and flushed with Argon. After re-evacuating to a pressure of about 10^{-3} torr, the quartz tube was melted in between the specimens in order to isolate them. The specimens were then annealed in a furnace for three days at approximately $600^{\circ}K$, see Figure 3.1.

Using an 11 cm Debye-Sherrer X-ray powder camera, the absence of secondary phases was established, and values for the lattice parameter were obtained (Table 3A).

3.2 PULSE MAGNET

3.2.1 Principle

The principle of operation for a pulse magnet is that a high voltage is discharged from a capacitor bank, C, through the magnet coil which forms the inductive part of an LCR circuit (the resistive part, R, is due to the resistance of the coil winding and leads).

Using this arrangement high fields up to 500 KOe (160 KOe for the pulse magnet used in this experiment) may be obtained for short pulse lengths of the order of a few milliseconds. The field is oscillatory with a decaying amplitude, characteristic of such circuits.

The magnetic field strength and the resultant magnetisation of the specimen are measured by integrating the outputs of two pick-up coils wound round the specimen on a quartz tube which fits co-axially inside the core of the magnet. To remove any signal in the magnetisation coils due to the changing magnetic field, a fraction of the output from the field-measuring coil is

Composition	Lattice Spacing Å
$DyCo_2$	7.175
$DyCo_{1.5}Ni_{0.5}$	7.180
DyCoNi	7.174
$DyCo_{0.5}Ni_{1.5}$	7.165
$DyNi_2$	7.149

TABLE 3.A

Size of lattice spacing with composition

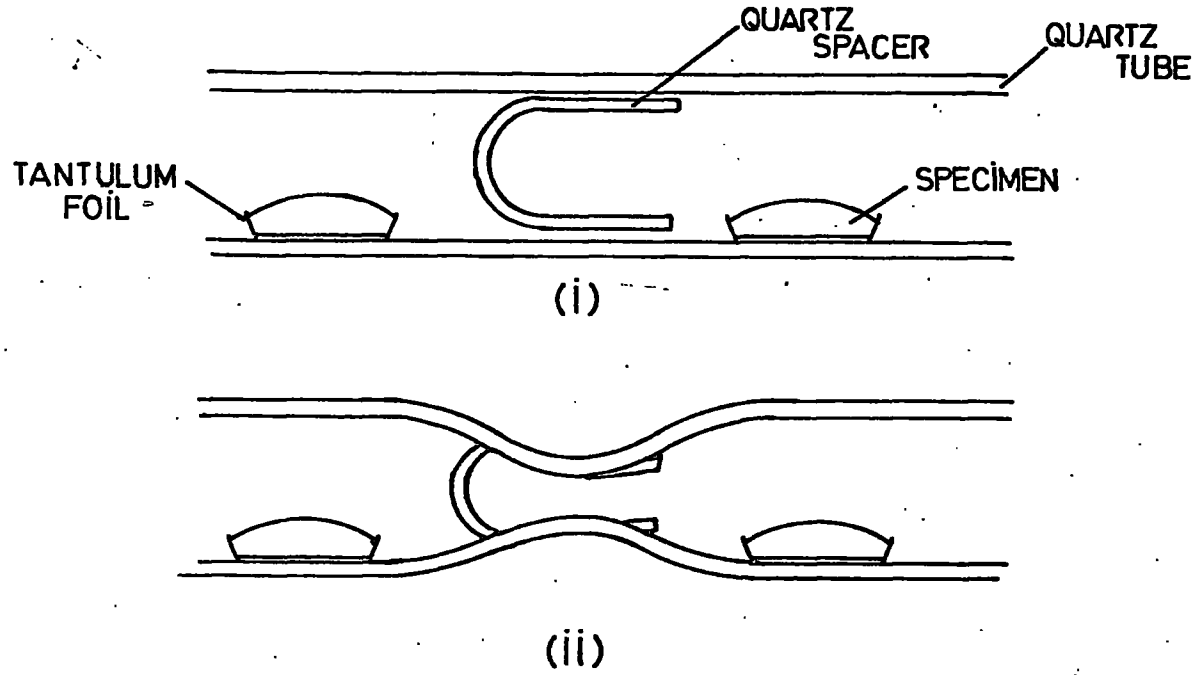

FIG. 3.1

Annealing specimens; (i) before melting and (ii) after melting to isolate the specimens

subtracted from that of the magnetisation coils. Also, any signals due to noise, such as eddy currents in the magnetic coil, are removed, or partially removed, by adding a correction signal derived from a small coil referred to as the Phase Shift Coil.

After integrating the resultant signals from the magnetic field strength and magnetisation pick-up coils, a hysteresis curve for the specimen is obtained by displaying both outputs on an oscilloscope.

3.2.2 Production of Field

The high fields were produced by discharging a 2000 μF capacitor bank through a magnet made from a Beryllium-Copper alloy. The alloy (2% Beryllium) was chosen for the magnet because, although its electrical conductivity is not as great as pure Copper, it has the much higher tensile strength needed to withstand the large forces resulting from the high magnetic fields(36).

A helix of ten turns per inch (total of 36 turns) was machined from a solid cylinder (57 mm in diameter) of the alloy, by machining a thread (width 1.27 mm) to a depth of 15 mm, leaving a core of 26 mm diameter. The threaded cylinder was potted in araldite. After allowing the araldite to harden, the one-inch core was drilled out, leaving a helix supported in araldite. The helix was then freed by burning off the araldite.

Two brass leads were hard soldered to each end of the helix. A one-inch diameter steel mandril was made with screw threads at each end. This was greased and inserted into the helix. Nylon insulation of thickness 0.5 mm was threaded between the turns. Two circular, one-inch thick tufnol end plates, each with a

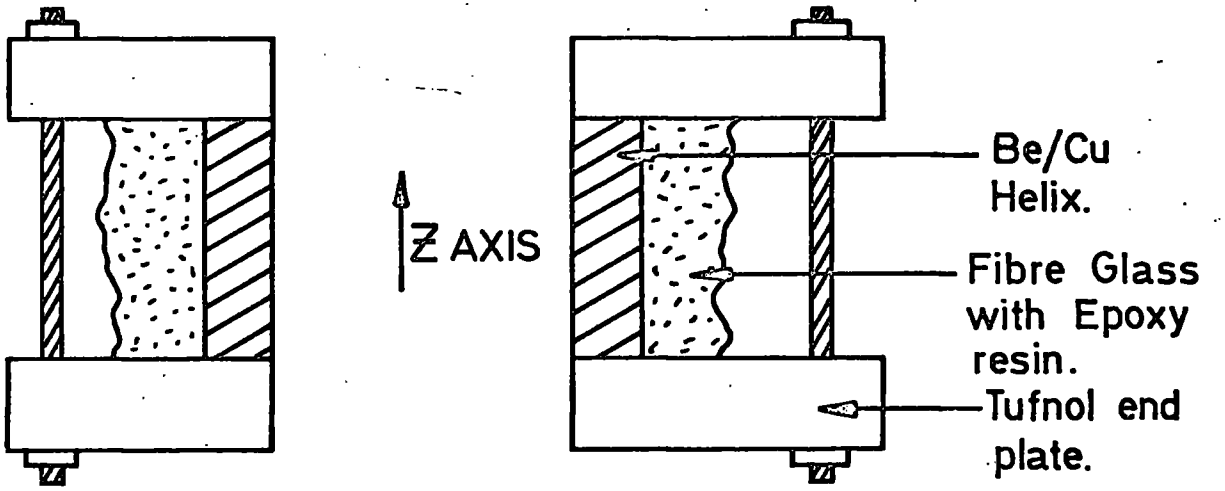

FIG. 3.2

Schematic representation of magnet used in pulsed field magnetometer showing the Z axis

central hole of one inch, were placed at either end of the helix such that the threaded ends of the mandril protruded. Two steel nuts were threaded into either end of the mandril and were used in order to compress the helix tightly such that neighbouring turns were separated only by the insulation. This is to reduce the axial rebound caused by the high magnetic field. The helix was wound on the outside with glass fibre impregnated with araldite in order to give the extra strength needed against the radial forces.

The magnet was secured from above so that the axis (z axis) of the magnet was vertical (Figure 3.2). This facilitates the immersion of the magnet into a liquid nitrogen bath which reduces the resistance of the magnet winding.

The maximum voltage obtainable from the power supply (figure 3.4) is 2 KV, giving a maximum stored energy of 4KJ (this is also limited by the maximum capacitor voltage). This large energy is discharged through the magnet by means of a mechanical switch comprised of two Molybdenum plates. The switch is opened and closed by means of a DC solenoid whose core is mechanically connected to one of the plates.

The variation of the field with time may be found theoretically by solving the differential equation for the current flowing through LCR circuit. (For a general form of the equation for the magnetic field see Appendix C). The result is as follows:-

$$I = Io\, e^{-\lambda t} \sin wt$$

where $\lambda = \frac{R}{2L}$ and $w^2 = \frac{1}{LC} - \frac{R^2}{4L^2}$

The magnetic field is therefore given by:-

$$H(z,t) = Ho(z)\, e^{-\lambda t} \sin wt$$

where z is the longitudinal axis of the magnet (Figure 3.2). The field therefore has the form of a sine wave with exponentially decaying amplitude (Figure 3.3). The period of the field was

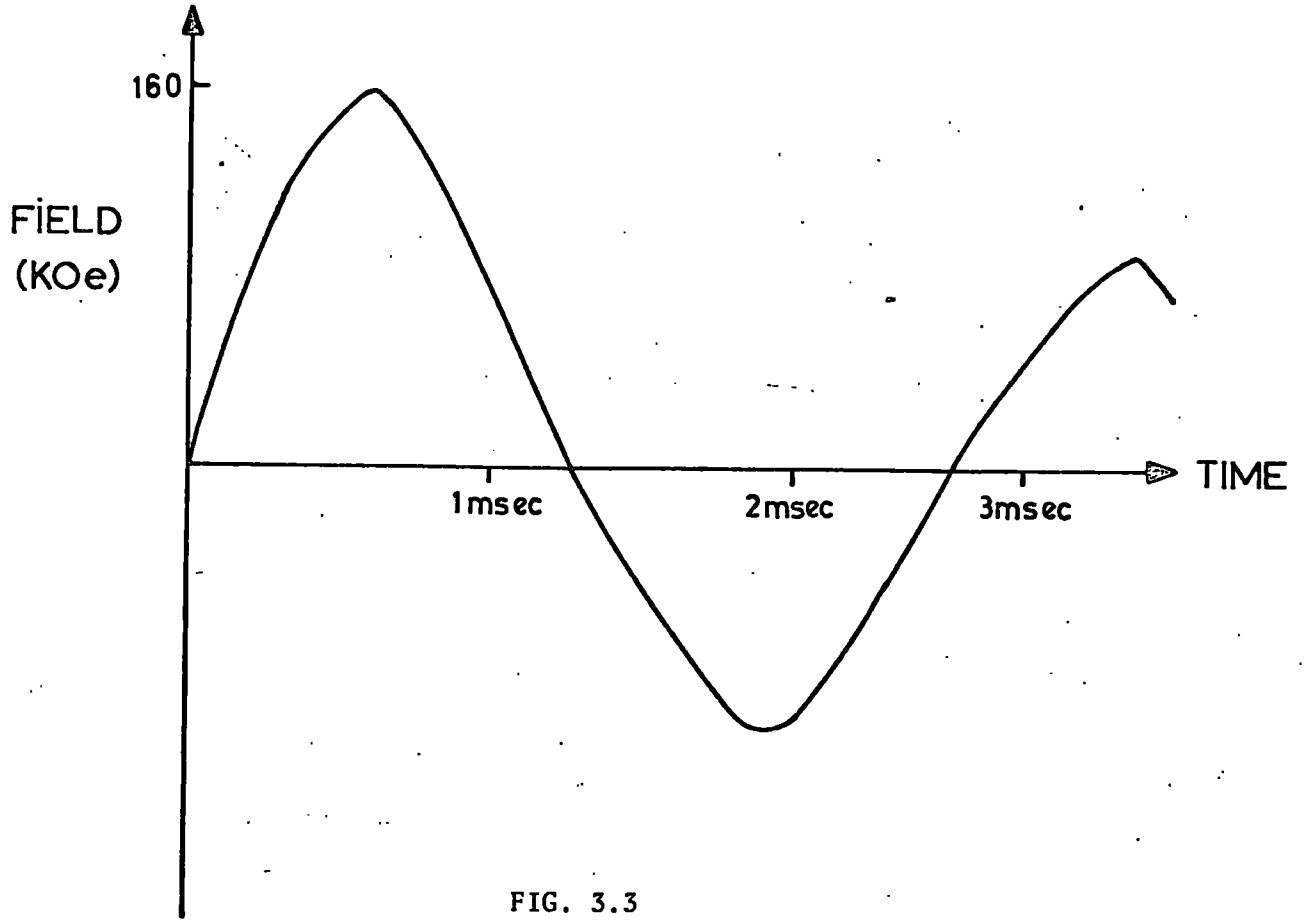

FIG. 3.3

Variation of field with time using the pulsed field magnet

found to be 1.25 milliseconds, and the maximum obtainable magnetic field was 160 KOe.

In practice, the magnetic field will not have the ideal form described above. A certain amount of noise will arise due to (a) Joule heating of the magnet, (b) eddy currents induced in the magnet helix, and (c) variation in current distribution across the cross-section of the magnet turns due to the interaction of coil current with field.

In order that these noise signals may be minimised and kept constant, and therefore be allowed for, the magnet must be at the same temperature at the beginning of each pulse. It is only then that the Joule heating is constant for pulses of equal magnitude. An interval of two minutes was found necessary between large pulses to return the magnet to its former temperature, i.e., that of liquid nitrogen. For smaller pulses, the repetition rate is correspondingly higher.

3.2.3 Measuring Systems

The specimen is held in a perspex holder (Figure 3.5) which is a tight fit on a stainless steel tube. The specimen may be either in bulk or powder form.

To measure the magnetisation of a specimen for a particular magnetic field, various pick-up coils were employed (Figure 3.6). The functions of these coils are described below.

All coils were wound using 44 SWG insulated copper wire, on a quartz tube which fits into the core of the magnet and is co-axial with it. The coils are wound on the part of the quartz tube which is in the maximum field position.

FIG. 3.4 Power Supply For Capacitor Bank

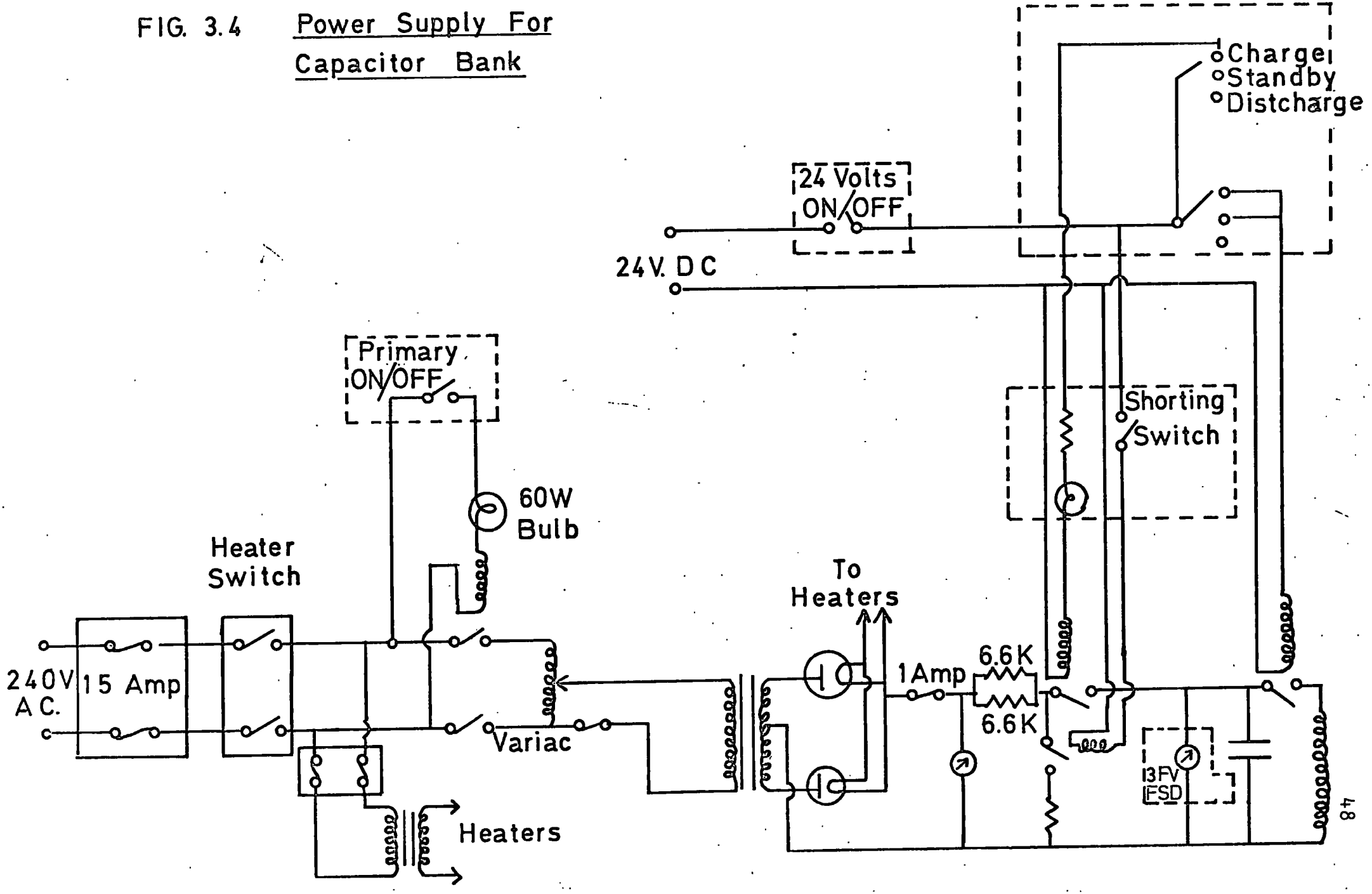

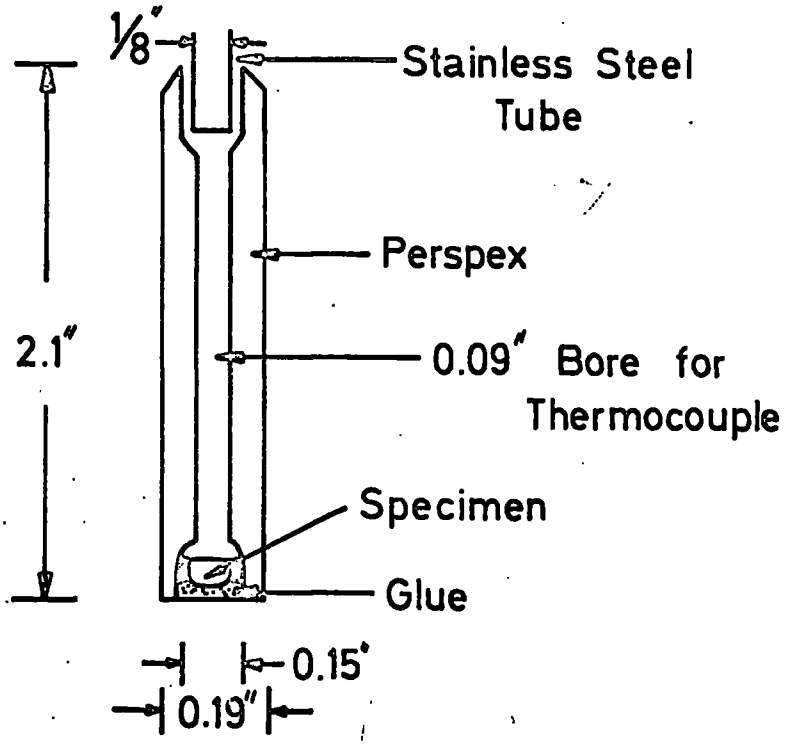

FIG. 3.5

Perspex holder used for mounting the specimen in the pulsed field magnetometer.

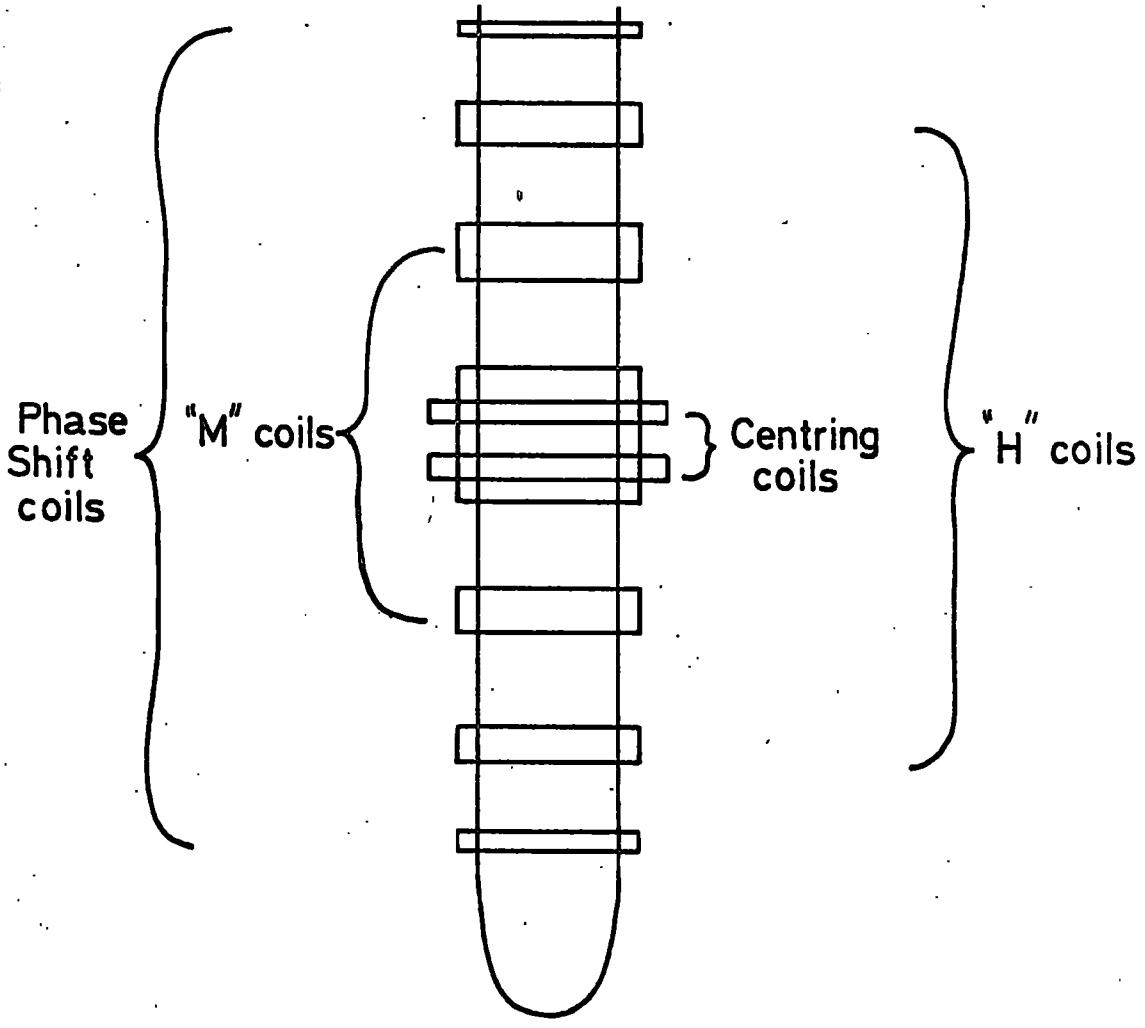

FIG. 3.6

Pick-up coil assembly used for measuring the magnetisation of a specimen in a measured applied field.

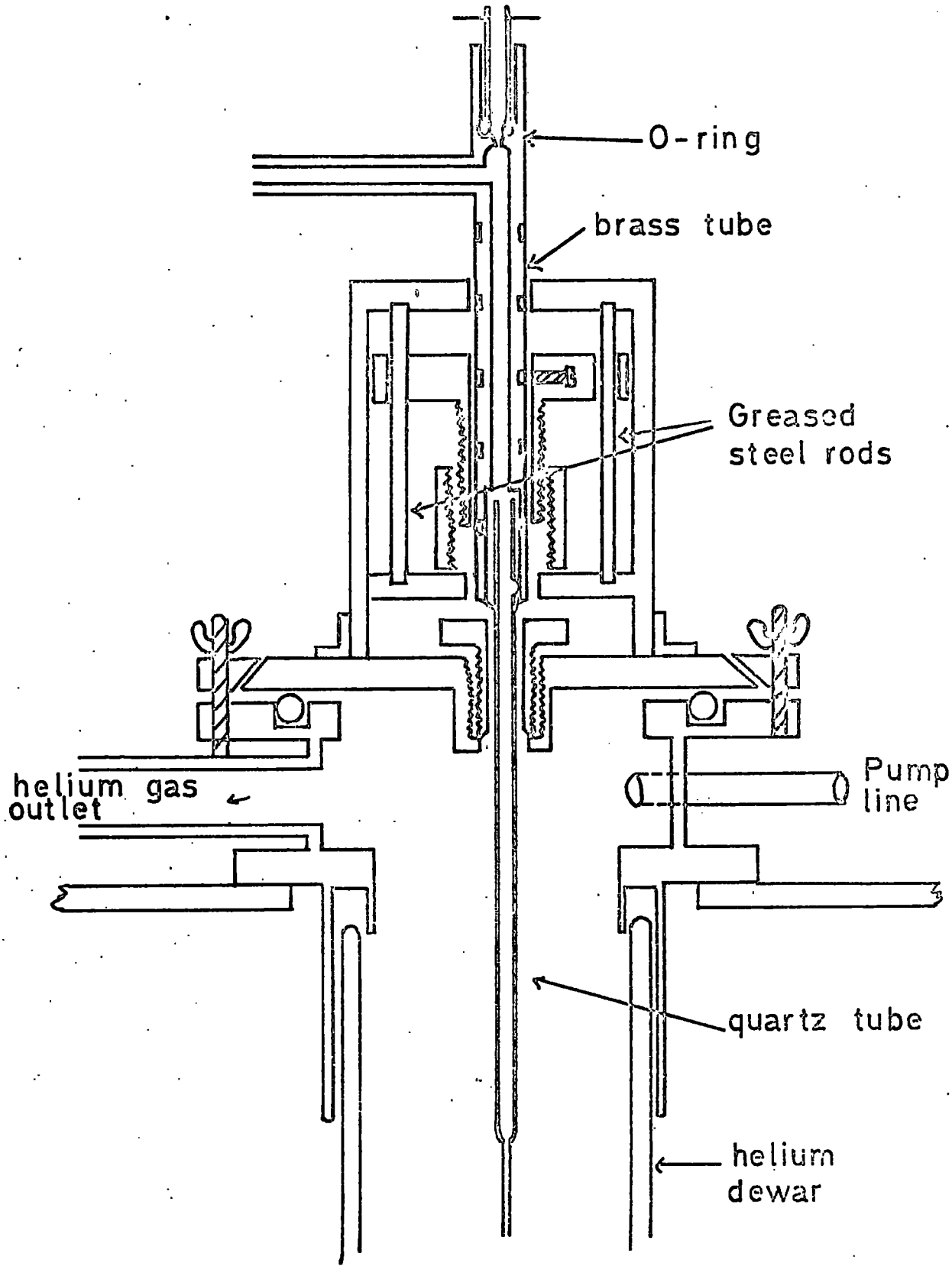

FIG. 3.7

Dewar Head and Height Adjuster

The length of the stainless steel tube is such that the specimen is held in the middle of the pick-up coil assembly. Minor adjustments to the position of the specimen could then be made using the height adjuster shown in Figure 3.7.

As the signals from the pick-up coils are proportional to the rate of change of magnetisation or field (depending on the coil in question), they have to be integrated to yield the magnetisation or field directly. The circuit used for this purpose is shown in Figure 3.8, and its operation is outlined below.

Field Measurement

The coil used for measuring the field experienced by the specimen consists of thirty turns. As the field is a function of the distance along the Z axis of the magnet as well as time, as outlined previously, the output from a single coil will vary with the coil's position. To remove this dependence on position, the coil is wound in two halves - one below and one above the plane of symmetry for the magnet (Figure 3.6). If the vertical position of the coil is now changed, the increase in the signal from one coil will then be counterbalanced by the decrease in the other coil.

The output from the two coils is integrated by means of an electronic integrator (Figure 3.9). The 10MΩ resistor in combination with the 0.01μF capacitor results in a charge leakage with a time constant of the order of 100m secs and is therefore sufficiently large not to distort the signal during the pulse period.

Magnetisation Measurement

To measure the magnetisation of a specimen, the output from a coil with a total of 140 turns is integrated using an electronic

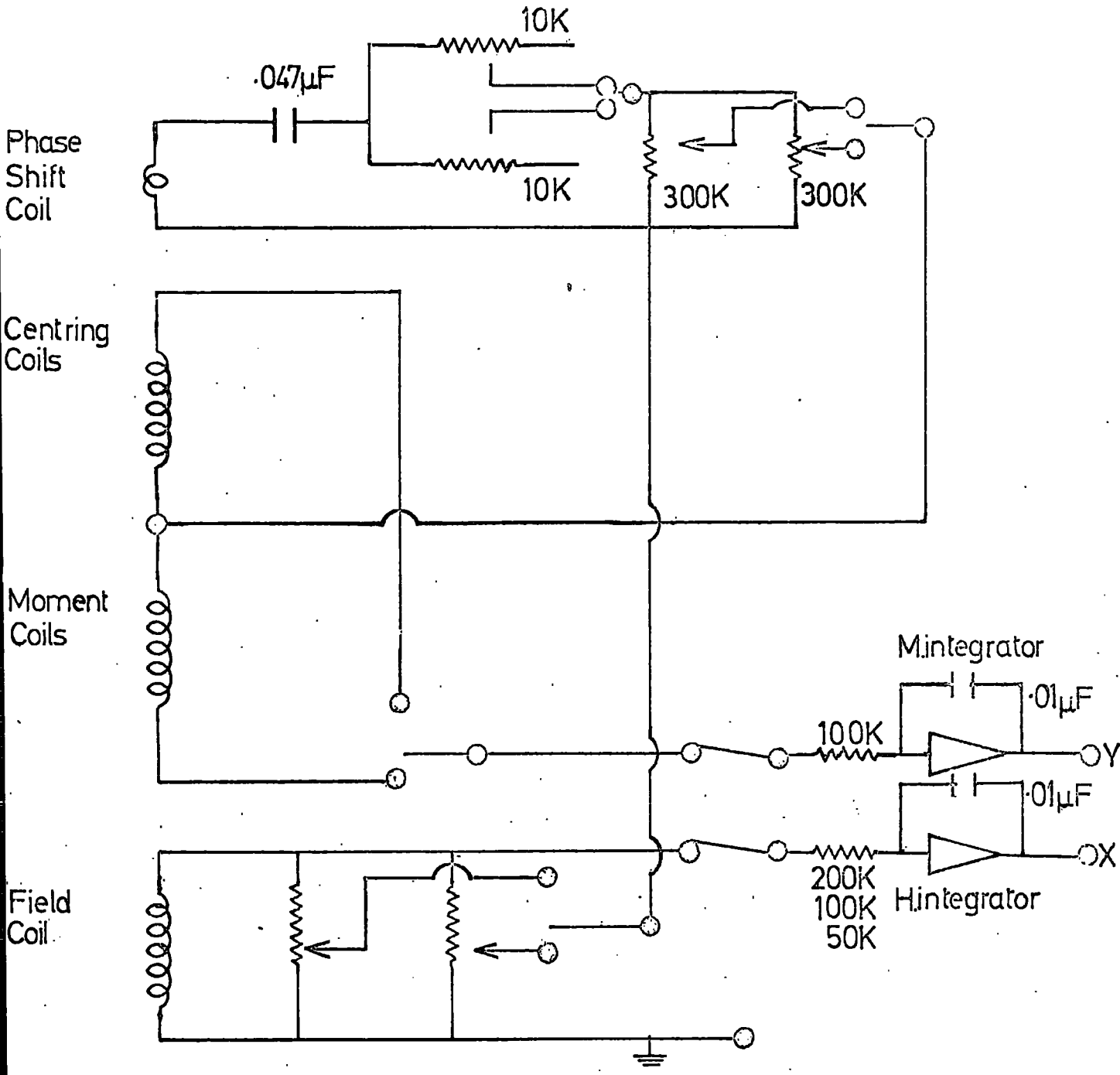

FIG. 3.8

Circuit used in pulsed field measurements

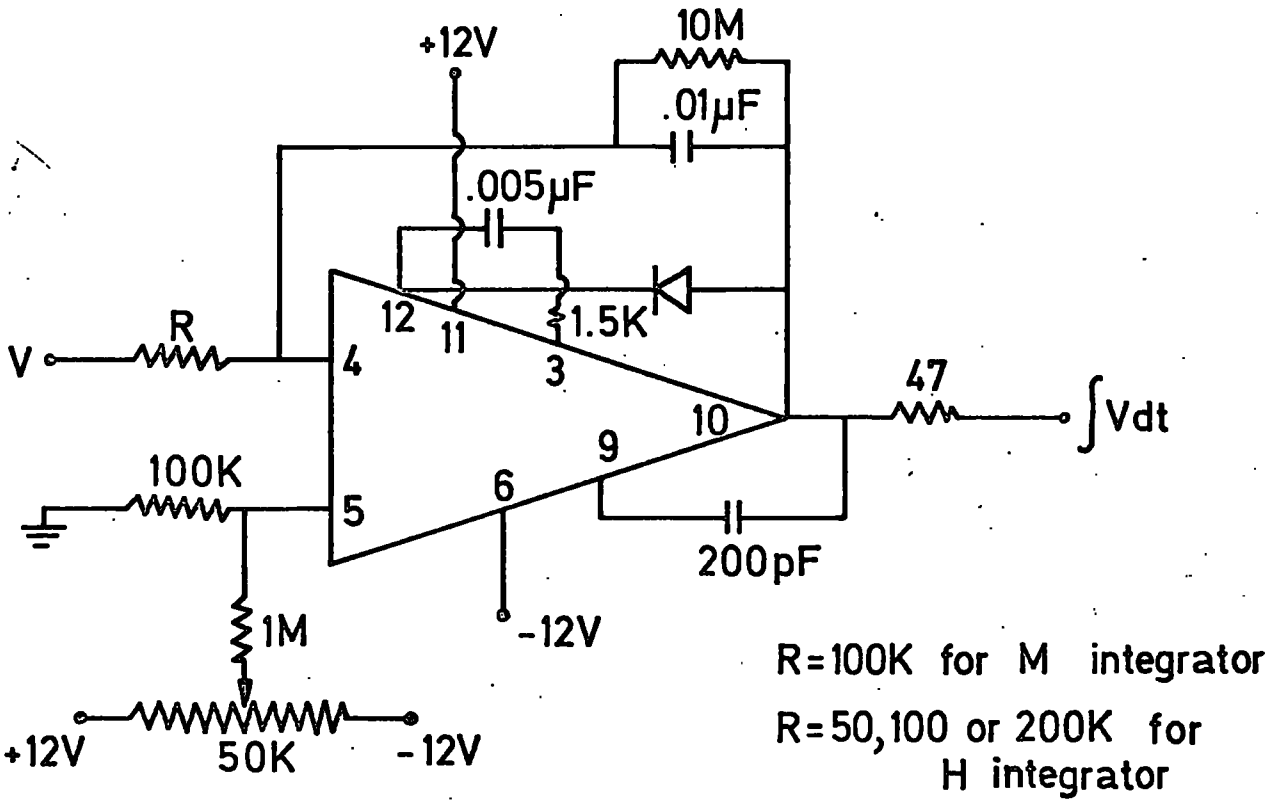

FIG. 3.9

Electronic integrator used in Fig. 3.8 to obtain the magnetisation of a specimen and the applied field directly

integrator identical to that shown in Figure 3.9. The theory of this measurement of magnetisation is reviewed in Appendix A.

To remove the dependence on the change of flux through the coil not linked with the specimen, i.e., dH/dt, the magnetisation coil is divided into three sections.

With the specimen situated in the middle of the central section of the pick up coil, the signal from this section is proportional to dM/dt + dH/dt. This section of the coil consists of 70 turns and is sufficiently long (8 mm) for the M signal not to be too sensitive to the vertical position of the specimen.

The two outer sections each contain 35 turns and are counterwound to the middle section. They are situated symmetrically about the middle section (see Figure 3.6) in order to remove the dependence of their output to the vertical position relative to the field. As these two sections are situated away from the specimen, they are relatively unaffected by its change of magnetisation, i.e., dM/dt, and their output is proportional to $-\frac{1}{2}$ dH/dt (minus sign as they are counterwound to the middle section). The total signal from all three sections should therefore be only dependent upon the rate of change of magnetisation of the specimen. The signal due to dH/dt is not completely removed, however, since the two outer coils are in a lower field region than the central section. The final balancing is achieved by tapping off a small signal from the field measurementcoil using the potentiometer, P1, as shown in Figure 3.8 which gives the entire circuit for the magnetisation and field strength detection system.

The signal from the potentiometer is applied in opposition to the signal from the M coil to balance out any residual signal due to dH/dt.

Ideally, with no specimen, a horizontal line for the M against H display should be obtained on the oscilloscope for the blanced system. As a result of eddy currents though, the display was found to have the form of an ellipse. This component is eliminated by adding a signal of equal and opposite magnitude and equal pahse until a straight line is obtained. The correction signal is derived from a coil referred to as the Phase Shift coil (Figure 3.6).

The Phase Shift coil is divided into two sections, each of eight turns. The output signal from the coil is applied to a phase shift circuit (Figure 3.8) consisting of a resistor, R, and capacitor, C, in series. As $RCw<1$, where w is the angular frequency of the signal, the circuit acts as a differentiator. Varying R, by means of potentiometer, P2, the required phase shift can be obtained. The amplitude of the signal can then be adjusted by means of potentiometer, P3. The signal is then added to the total signal from the M coil to minimise the noise.

To correct for the effects of residual noise, oscillograms of the M vs H display with and without specimen are photographed for the same value of capacitor charge, i.e., same value of applied field. The photographs are then projected and traced on to graph paper and subtracted from each other. The projection of the photographs also allows for the oscillograms to be magnified, and therefore improves the accuracy of measuring the parameters of critical field, etc.

Centring Coils

To obtain the maximum signal from the magnetisation coil, the specimen must be situated at the centre of the middle section. The position of the specimen is varied by means of the height

adjuster shown in Figure 3.7.

Rather than move the specimen up and down inside the coil assembly until the maximum magnetisation signal is obtained, two centring coils are incorporated into the system to facilitate the positioning of the specimen.

The two coils each consist of 15 turns. They are wound in opposition on top of the central section of the magnetisation coil, symmetrically above and below its mean position (Figure 3.6).

When centring the specimen, the moment integrator circuit is switched from the moment coils to the centring coils in order to integrate their output. A horizontal line is obtained on the oscilloscope if the specimen is midway between the centring coils. Otherwise a hysteresis loop is obtained which will reverse as the specimen passes through the mean position.

Calibration of Signals

H-Signal

A powder specimen of $ZnCr_2Se_4$ is used to calibrate the H signal. This compound is chosen because it has a well defined critical value of field, 64 KOe, at which the magnetisation saturates.

From the magnetisation versus field trace, the sensitivity of the field measurement was found to be 34 ± 1.3 KOe/cm on the (x 1,200 KOe) setting (see Figure 3.8).

M-Signal

By using a specimen of iron, whose saturation magnetisation is well known (37), it is possible to calibrate the M signal. To reduce the effects of eddy currents in the iron, powdered specimens were used.

To investigate the dependence of the M signal upon the size

of the specimen, three cylindrical samples, each containing different masses of powdered iron, were made. Each had different length to diameter ratios (the diameter being the diameter of the inside cavity of the specimen holder).

A trace of M against H was taken for each specimen and the signal corresponding to the saturation moments evaluated. The voltage corresponding to the saturation moment was then plotted against the mass of the specimen (Figure 3.10). Figure 3.10 shows that the signal is directly proportional to the mass of the specimen and does not, to first order, depend upon its length.

The calibration factor was found to be 0.0317, i.e., the magnetisation of a specimen in Bohr magnetons is given by:-

$$M = \frac{0.0317 \times (\text{M. Wt of Specimen}) \times (\text{Signal in mv})}{(\text{Mass of Specimen in mg})}$$

3.2.4 Temperature Control and Measurement

The Cryostat

The cryostat (Figure 3.11) was designed for containing liquid helium in order to measure the magnetic properties of specimens from 4.2°K to room temperature.

As the magnet is operated whilst immersed in liquid nitrogen (Section 3.2.2), it is not necessary for the upper nitrogen dewar to extend into the core of the magnet (which would require a larger diameter core and consequently lower field strengths). Instead, a hole is machined out of the base of the upper nitrogen dewar to accommodate the tail of the helium dewar. This allows the tail to protrude into the core of the magnet.

Both upper and lower liquid nitrogen dewars were machined out

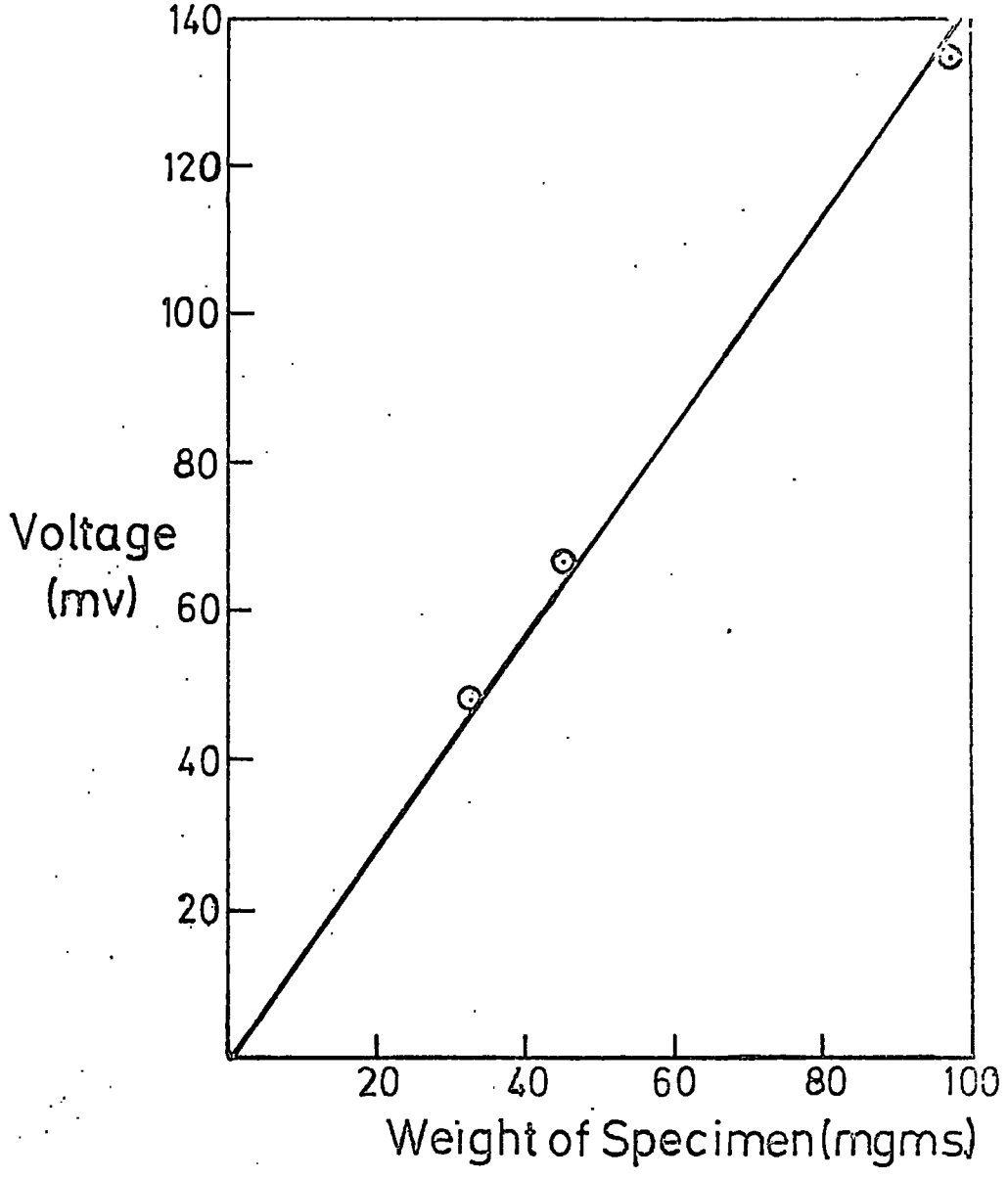
140
120
100
80
60
40
20
Voltage
(mv)
20
40
60
80
100
Weight of Specimen (mgms)

FIG. 3.10

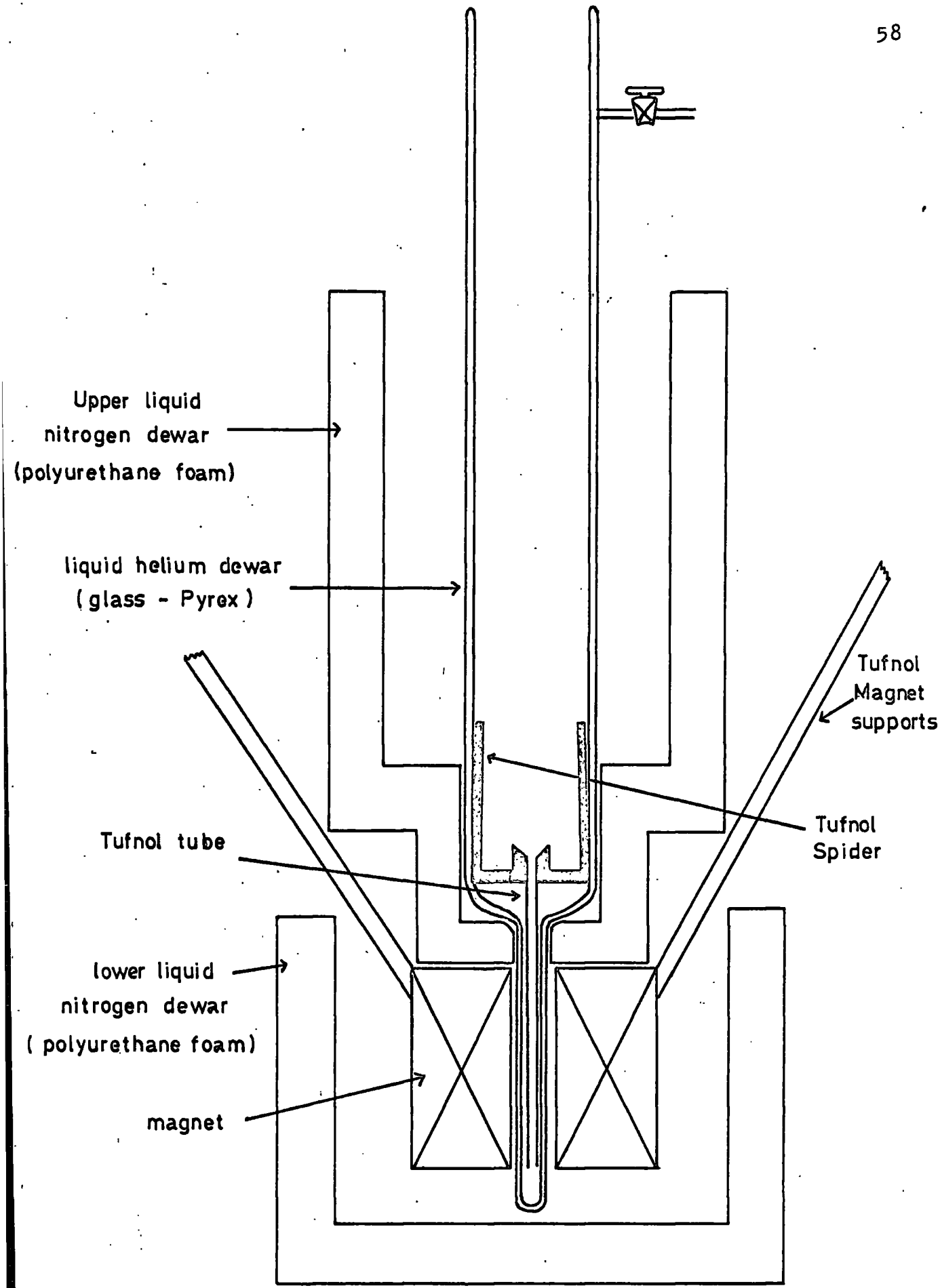

FIG. 3.11

Cryostat used for pulsed field magnetometer.

of polyurethane foam. Leakage of liquid nitrogen from the upper to the lower liquid nitrogen dewar, round the outside of the liquid helium tail, is avoided by applying vacuum grease round the inside of the hole. At liquid nitrogen temperatures the grease froze giving an effective seal.

Temperature Measurement

Throughout the major part of this study, temperatures are measured using a gold/copper : copper thermocouple. Both thermocouple wires are insulated with PTFE sleeving, and the junctions are made in a normal Bunsen flame.

The thermoelectric e.m.f.'s are measure using a Pye portable potentiometer and Scalamp Galvanometer to detect the potentiometer balance point. The reference junction is placed in liquid nitrogen. The other sensing junction is held as close to the specimen as possible in order to prevent "temperature lag". This is achieved by threading both thermocouple wires down the stainless steel tube and down the bore of the specimen holder.

A heater coil is incorporated into the system to facilitate measurements at a series of temperatures. The heater coil is wound, non-inductively, from constantan wire, round a tufnol tube. The tufnol tube is attached to a tufnol tripod which rests at the bottom of the liquid helium dewar (Figure 3.11), thereby locating the heater coil round the pick-up coil assembly. The voltage for the heater coil is obtained from the 24 volt supply by means of a potentiometer.

3.2.5 Mechanical Considerations

The dewar head is supported by a steel bridge (Figure 3.7).

The brass height adjuster is attached to the top plate of the dewar. The function of the height adjuster is to vary the vertical position of the quartz tube holding the pick-up assembly.

The lower end of the quartz tube is confined to the axis of the magnet by the hole in the tufnol tribpod. The upper end of the quartz tube is cemented into the inside of a brass tube using araldite. The upper end of the stainless steel tube holding the specimen is seated on top of the brass tube and sealed by an O-ring. The top of the stainless steel tube is threaded in order that the height of the specimen may be adjusted by screwing or unscrewing the wing nut which sits on top of the brass tube (Figure 3.7). In order to prevent air entering the system on removing the stainless steel tube to change specimens, an excess pressure of helium gas is maintained in the system.

3.3 DETERMINATION OF ORDERING TEMPERATURES

There is a variety of methods used to determine the ordering temperature, known as the Curie Temperature, T_c, of ferromagnetic materials.

One such method uses the relationship derived thermodynamically by Belov(38). He showed that, near the Curie temperature,

$$M^2_{H,T} = M^2_{O,T} + \frac{aH}{M_{H,T}}$$

where a is a constant. Therefore, if a plot is made of $M^2_{H,T}$ against $H/M_{H,T}$ for different temperatures, then T_c is that isotherm whose linear extrapolation passes through the origin, i.e., $M_{O,T} = 0$. This is a lengthy method, however, involving the accumulation of much data.

A much simpler method uses the fact that, for fields of the order of 10KOe, the spontaneous magnetisation, $M_{H,T}$, is, to within 1%, equal to the absolute spontaneous magnetisation, $M_{O,T}$, at temperatures not too near the Curie temperature. From the molecular field predictions by Weiss (39), the relationship

$$M_{O,T}^2 \propto (T_c - T)$$

may then be used to give T_c by extrapolating the M^2 against T curve on to the temperature axis.

Two methods of determining T_c used in this study are given below.

3.3.1 Pulsed Field Magnetometer Method

The pulsed field magnetometer described in the previous section may be used to determine the Curie temperature of a specimen.

From oscillograms of magnetisation, M, against field for various ~~fields~~ temperatures, a plot is made of M^2 against T at various temperatures. The intercept, $T_c(H)$, on the temperature axis is obtained for each constant-field curve and plotted against the field, H. From the resulting linear plot, $T_c(0)$ is obtained by extrapolating to H = 0.

This somewhat lengthy procedure was only adopted to check someof the Curie temperatures obtained by the method described below which, although not as accurate as the above method, is much quicker.

3.3.2 A C Susceptibility Method

In this method (40), the specimen forms the core of a small transformer whose output is then proportional to the initial permeability of the specimen.

The specimen in a powder form is held in a perspex holder which is attached to a stainless steel tube. An oscillator is used to apply a 500 Hz sinusoidal voltage across the input of the transformer, which induces an A C field at the centre of the core of the order of an oersted. To allow for the contribution to the output of the permeability of free space, a nulling transformer is placed in series with the transformer. By adjusting the movable ferrite core of the nulling transformer, the net output from both transformers, with no specimen, is zeroed. The signal, with a specimen in the core of the transformer, is amplified and detected using a Phase Sensitive Detector. This signal, which is proportional to the initial susceptibility χ, of the specimen, is applied to the Y-input of an X-Y pen recorder. The temperature of the specimen is obtained using a gold/copper : copper thermocouple which is threaded down the stainless steel tube so that the sensing junction may be held as near the specimen as possible to avoid any temperature difference between specimen and junction. The output from the thermocouple is applied to the X-input of the X-Y pen recorder.

For ferrimagnetic materials, as is the case in this study, the Curie temperature, T_c, is not as precisely defined in the χ v T plot, as is the Neel temperature for antiferromagnetic materials. This is a result of the dependence of χ upon both the spontaneous magnetisation and the anisotropy of the specimen. Both these parameters decrease with increasing

temperature in the region of T_c. Whereas the decrease in the spontaneous magnetisation decreases χ, the decrease in anisotropy yields an increase in χ as they are inversely dependent. Since paramagnetic susceptibility is present above T_c, a smooth variation of χ with T is obtained on passing through T_c. T_c is generally accepted to be the point of inflection of the curve.

It was found that there was a certain amount of hysteresis in the χ v T plots which gave an error in the value of T_c of $\pm 5^{\circ}K$. This is thought to be both dependent upon the thermal history of the specimen and also on the small temperature difference between specimen and surrounds. This method cannot be recommended for accurate measurement of T_c, but for the variation of T_c with composition for a series of compounds, as is required here, the inaccuracy can be ignored.

3.4 DETERMINATION OF MOLECULAR MOMENT

Ignoring polarisation effects, for the molecular moment of a compound to be determined from the absolute saturation magnetisation, $M_{0,0}$, an infinite magnetic field or absolute zero temperature is required. Nevertheless, an empirical relationship(41) was found to apply to ferromagnets at low temperatures between 1 and 30 KOe:-

$$M_{H,T} = M_{S,T} \left(1 - \frac{a}{H} - \frac{b}{H^2}\right) + cH$$

where $M_{S,T}$ is termed the saturation magnetisation at temperature, T, and $a > b \gg c$ are constants. The terms $\frac{a}{H}$ and $\frac{b}{H^2}$ are incorporated to account for domain and imperfection effects. The factor cH is relatively small at fields of 30KOe, but becomes significant as the field increases. This term is thought to arise from a redistribution of spin states resulting in an in-

crease in the domain magnetisation above the spontaneous value, $M_{O,T}$.

At fields of the order of 10 KOe and above, the saturation magnetisation can be regarded as being equal to $M_{O,T}$. The usual procedure is to extrapolate an $M_{H,T}$ v $\frac{1}{H}$ plot to $\frac{1}{H} = 0$, i.e., an infinite applied field. In the present study, however, the applied fields are large enough and the Curie temperatures are high enough above $4.2^{o}K$ to enable the saturation magnetisation to be measured directly.

From this measurement, using the calibration for the M coil (section 3.2.3), the molecular moment for the specimen is obtained.

CHAPTER FOUR

EXPERIMENTAL RESULTS

Specimens of different composition of the pseudo-binary series, $Dy(Co,Ni)_2$, were made in an arc furnace and subsequently annealed in a furnace for three days at 600°K (see Chapter 3).

4.1 THE SHAPE OF THE HYSTERESIS CURVE

Oscillograms of magnetisation against field were taken for the various compositions (with the specimen in solid form) at liquid helium temperatures using pulsed fields of the order of 15 to 160 KOe. One such curve for DyCoNi is shown in Figure 4.1. It has three striking features:-

(a) the initial magnetisation curve has a well-defined critical field, H_c, at which the magnetisation increases more rapidly;

(b) H_c is such that the initial magnetisation curve is displaced outside the subsequent hysteresis loops;

and, (c) the coercivity of the material is not constant but decreases from one half cycle to the next.

From the drawings of four oscillograms for DyCoNi at 4.2°K for different applied fields, shown in Figure 4.2, it is apparent that the critical field is dependent upon the maximum applied field. This dependence is plotted in Figure 4.3. Taylor et al(25) also noticed the dependence of H_c upon the maximum field. It will be shown in Chapter 5, however, that H_c is a function of the rate at which the field is applied and not the maximum

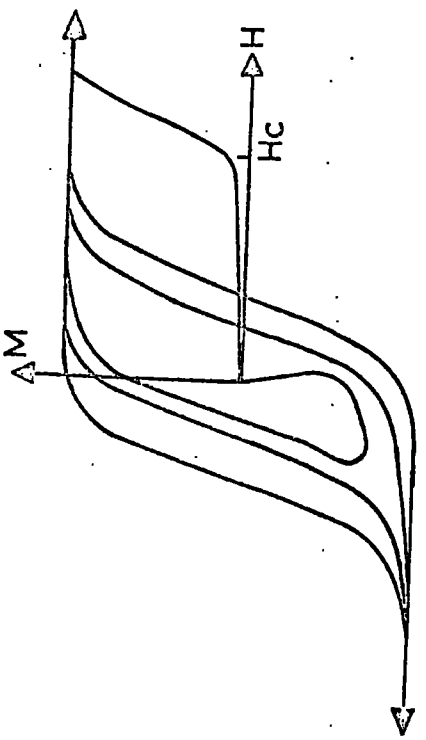

FIG. 4.1

Typical hysteresis curve showing critical field, H_c

field as is inferred in Figures 4.2 and 4.3.

To attempt to show that the shape of the hysteresis curve described above is not due to eddy currents, powder specimens were made and studied using the same techniques. No appreciable difference was observed in the shape of the subsequent oscillograms or in the values obtained for the critical field.

The possibility of the observed changes in magnetisation being attributed to the heating of the specimen was discounted by a calculation (see Appendix B) of the increase of specimen temperature in applied fields of the order of 100 KOe. A temperature rise of the order of $16\ ^{o}K$ was predicted. By monitoring the temperature of the specimen directly, using a Solatron digital voltmeter, an increase in temperature of approximately $3^{o}K$ was recorded for large applied fields. These values of temperature rise are too small to have any appreciable effect on the magnetisation curve of the specimen, which at $4.2^{o}K$ is well below the ordering temperature. Further, one would expect a greater influence on the shape of the final quadrant of the hysteresis loop rather than the initial quadrant, as is observed, if the effect were due to spurious heating of the specimen. Furthermore, one would also expect the critical field to decrease with increasing applied field rather than the observed increase. Finally, as these measurements are concerned primarily with the initial quadrant of the curve, then the effect of specimen heating may be neglected.

4.2 VARIATION OF CRITICAL FIELD WITH COMPOSITION

For a constant maximum applied field, oscillograms of the resulting magnetisation against field were taken for each com-

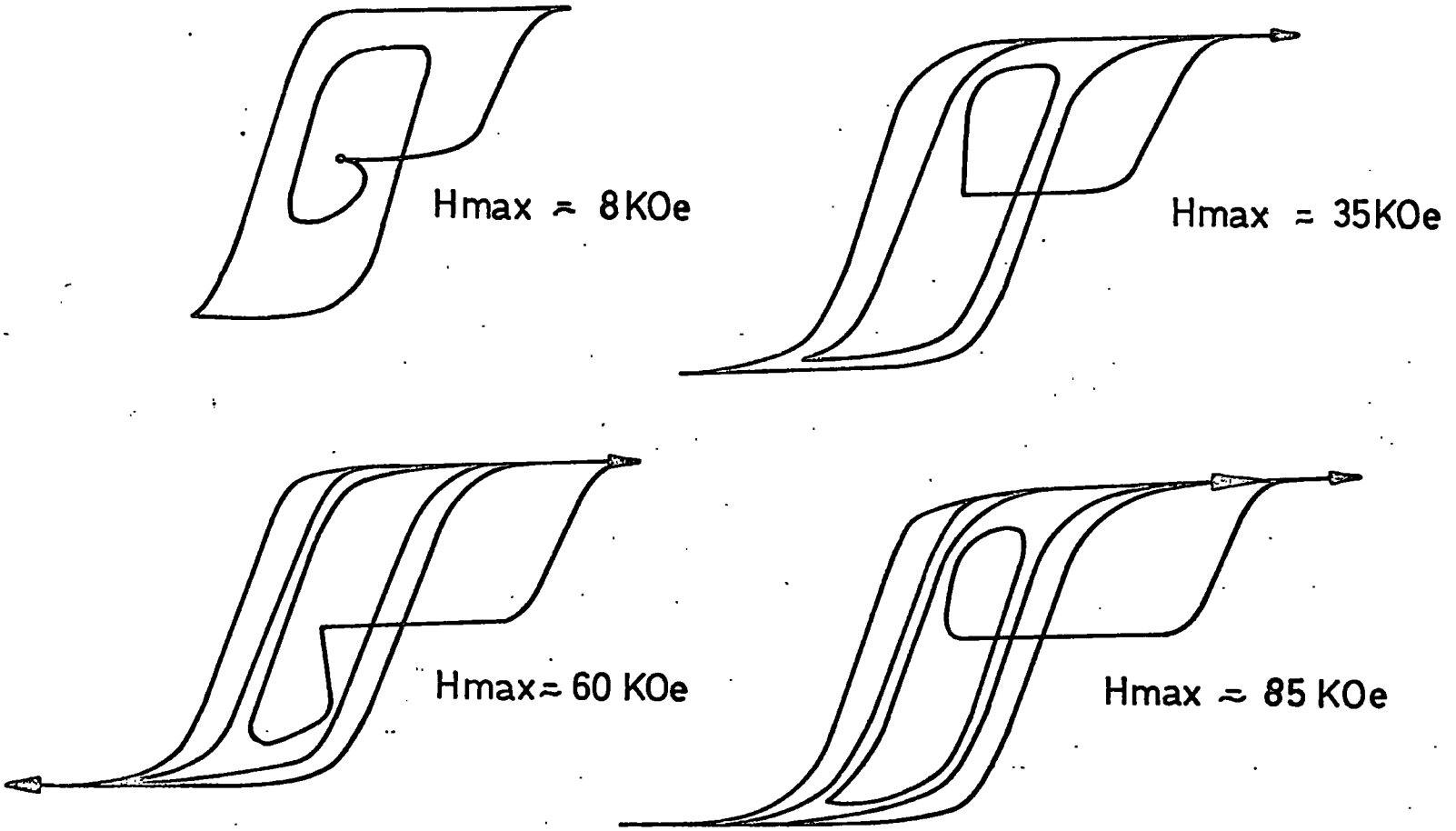

FIG. 4.2

Four typical magnetisation versus applied field oscillograms for different maximum applied fields, Hm

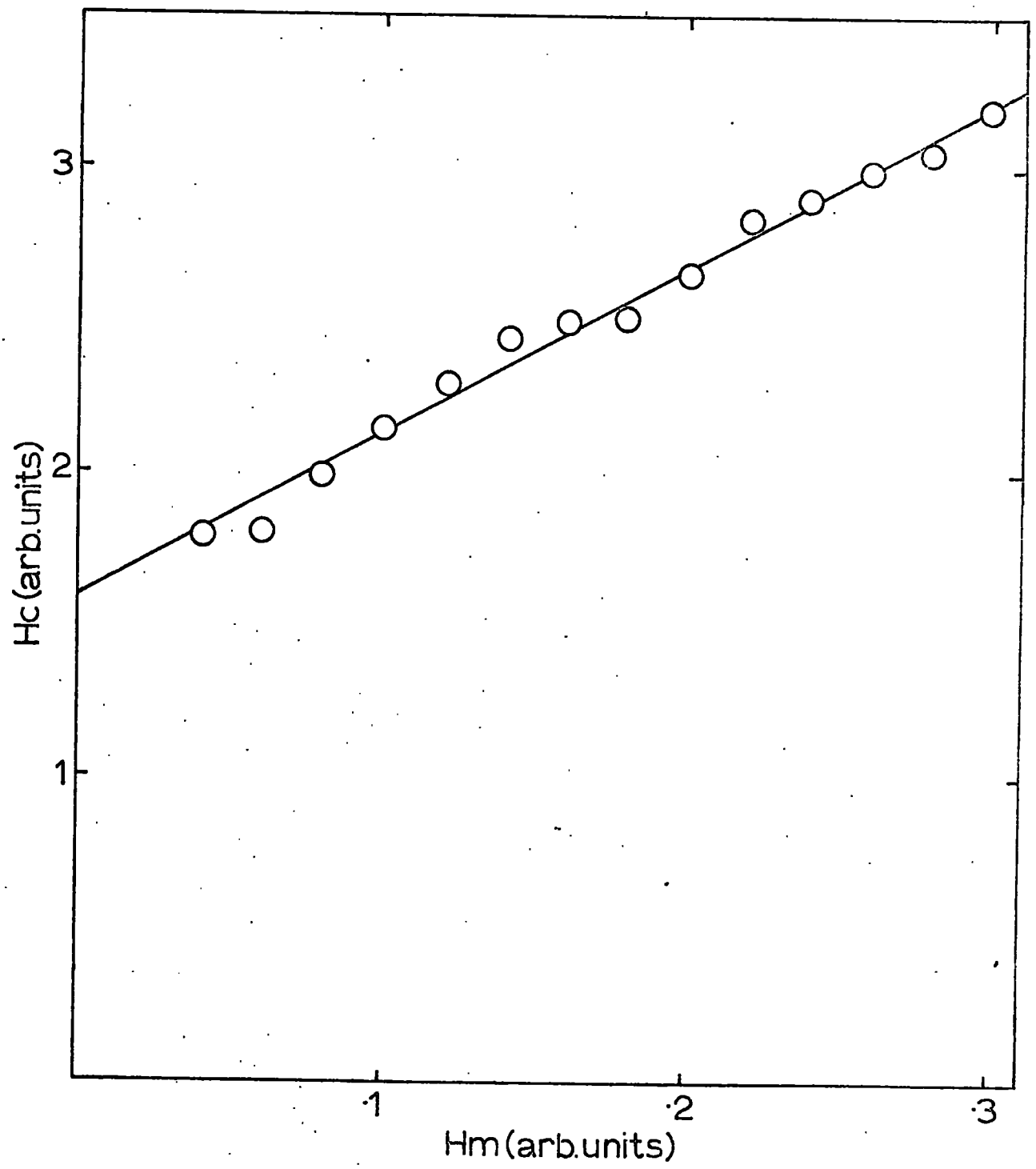

FIG. 4.3

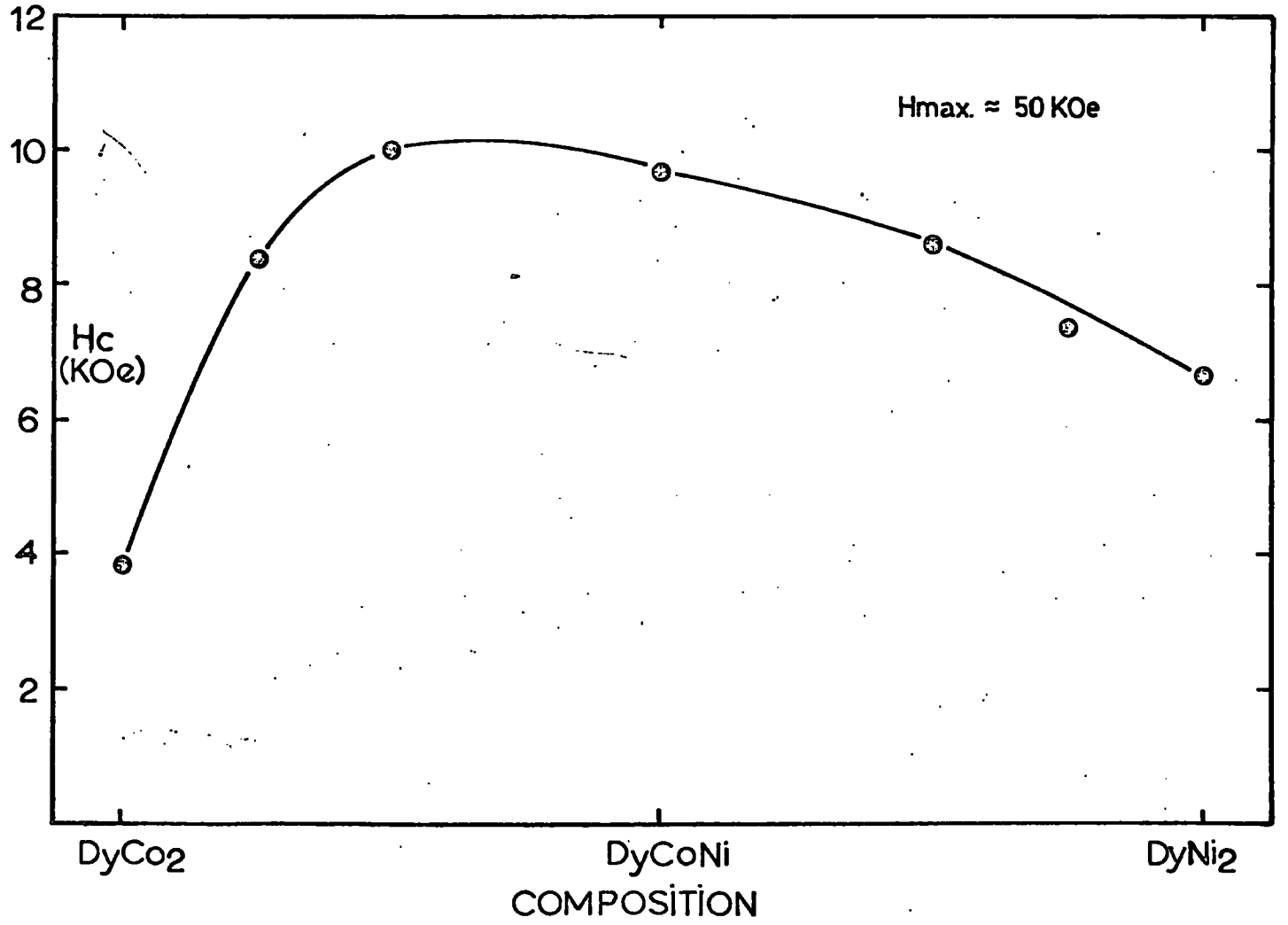

FIG. 4.4 Variation of critical field, H_c, with composition for constant maximum applied field

position at 4.2°K. The resultant variation of the critical field with composition is plotted in Figure 4.4. The initial increase of H_c at the cobalt rich end of the series, the broad maximum and the subsequent decrease at the nickel rich end of the series have been attributed to variations in the degree of pinning of the narrow domain wall with change of composition.

To demonstrate the applicability of the theory due to Zijlstra (see Chapter 2) measurements of the variation of the ratio of anisotropy constant to exchange constant are required. To determine the variation of exchange energy, measurements of the ordering temperature were taken for each composition. From Figure 4.5 it is apparent that the exchange energy initially decreases markedly as the nickel concentration is increased, but then changes less appreciably towards the nickel rich end of the series.

From the saturation value of magnetisation obtained from oscillograms for each composition, the molecular moment in Bohr magnetons was calculated using the expression in Chapter 3, section 3.2.3. The resulting variation with composition is given in Figure 4.6.

To demonstrate the applicability of the narrow domain wall pinning theory further, the rare earth component of the intermediate compound, DyCoNi, was gradually replaced by Terbium. The resulting variation of the critical field, at constant temperature and applied field, for the $(Dy_{1-x}\ Tb_x)CoNi$ series is shown in Figure 4.7.

4.3 TEMPERATURE DEPENDENCE OF THE CRITICAL FIELD

If, as proposed by Zijlstra, the energy barrier to domain

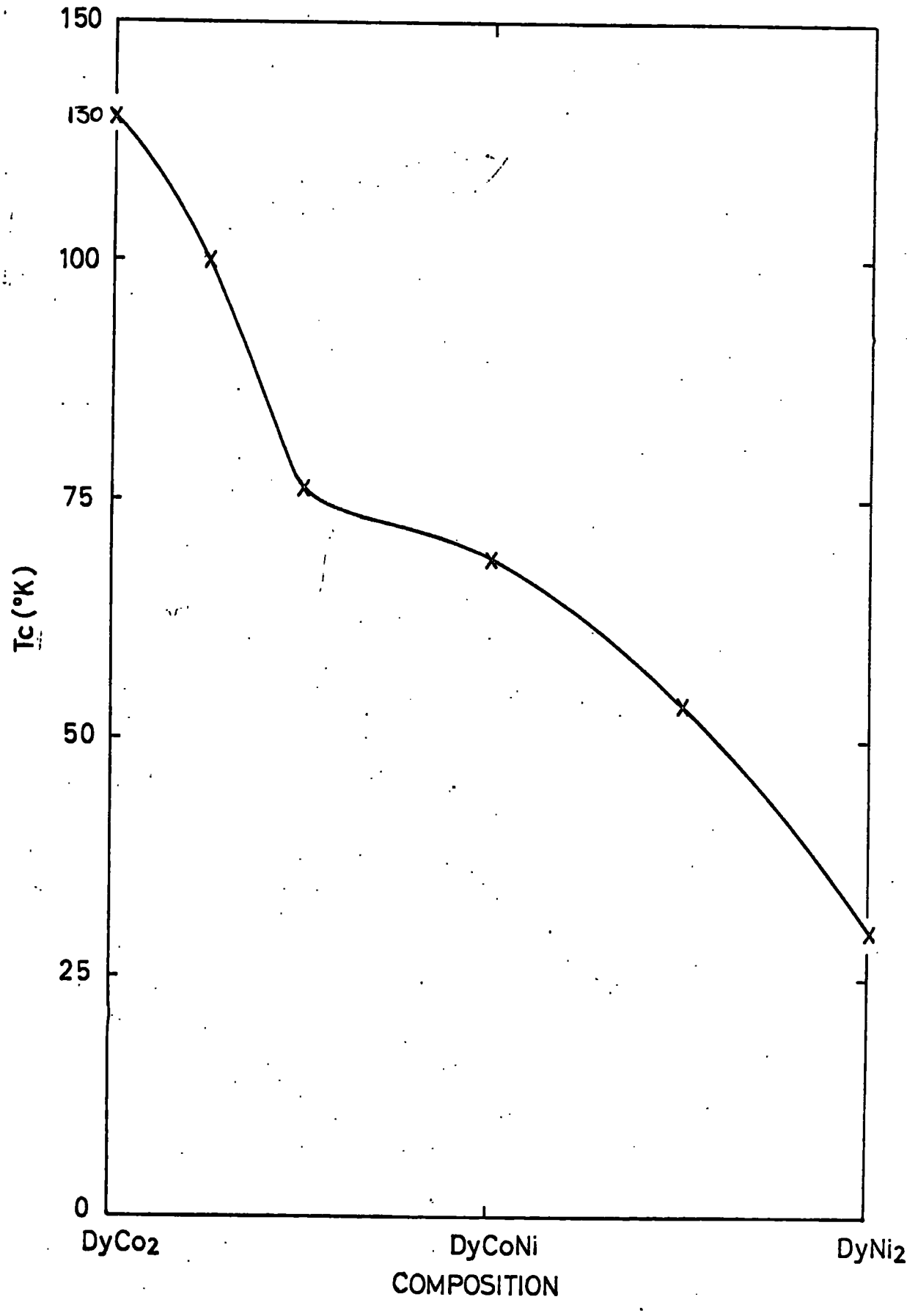

FIG. 4.5

Variation of ordering temperature across the series.

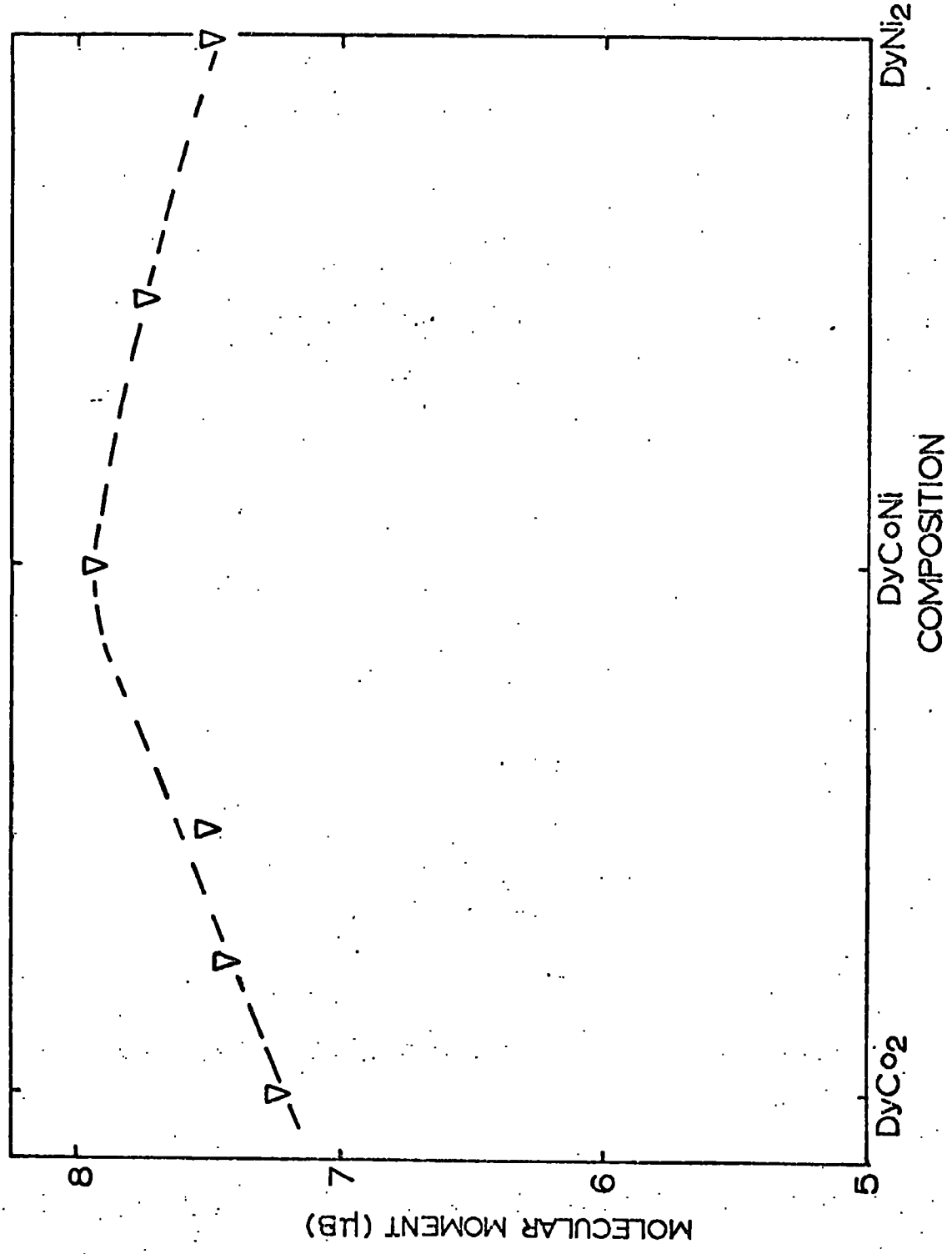

Fig. 4.6

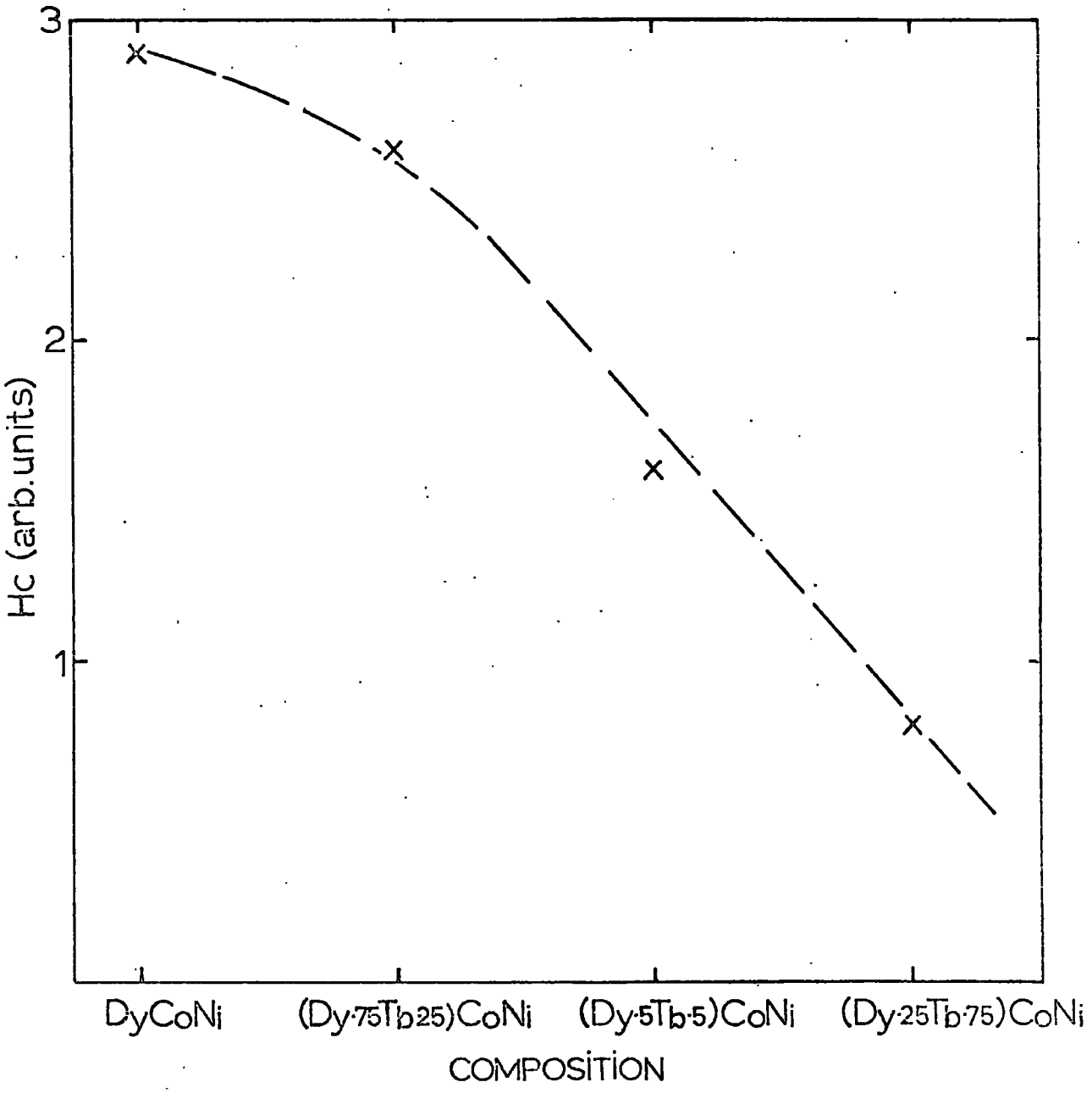
3
2
1
Hc (arb.units)
DyCoNi
(Dy·75Tb25)CoNi
(Dy·5Tb·5)CoNi
(Dy·25Tb·75)CoNi
COMPOSITION

FIG. 4.7

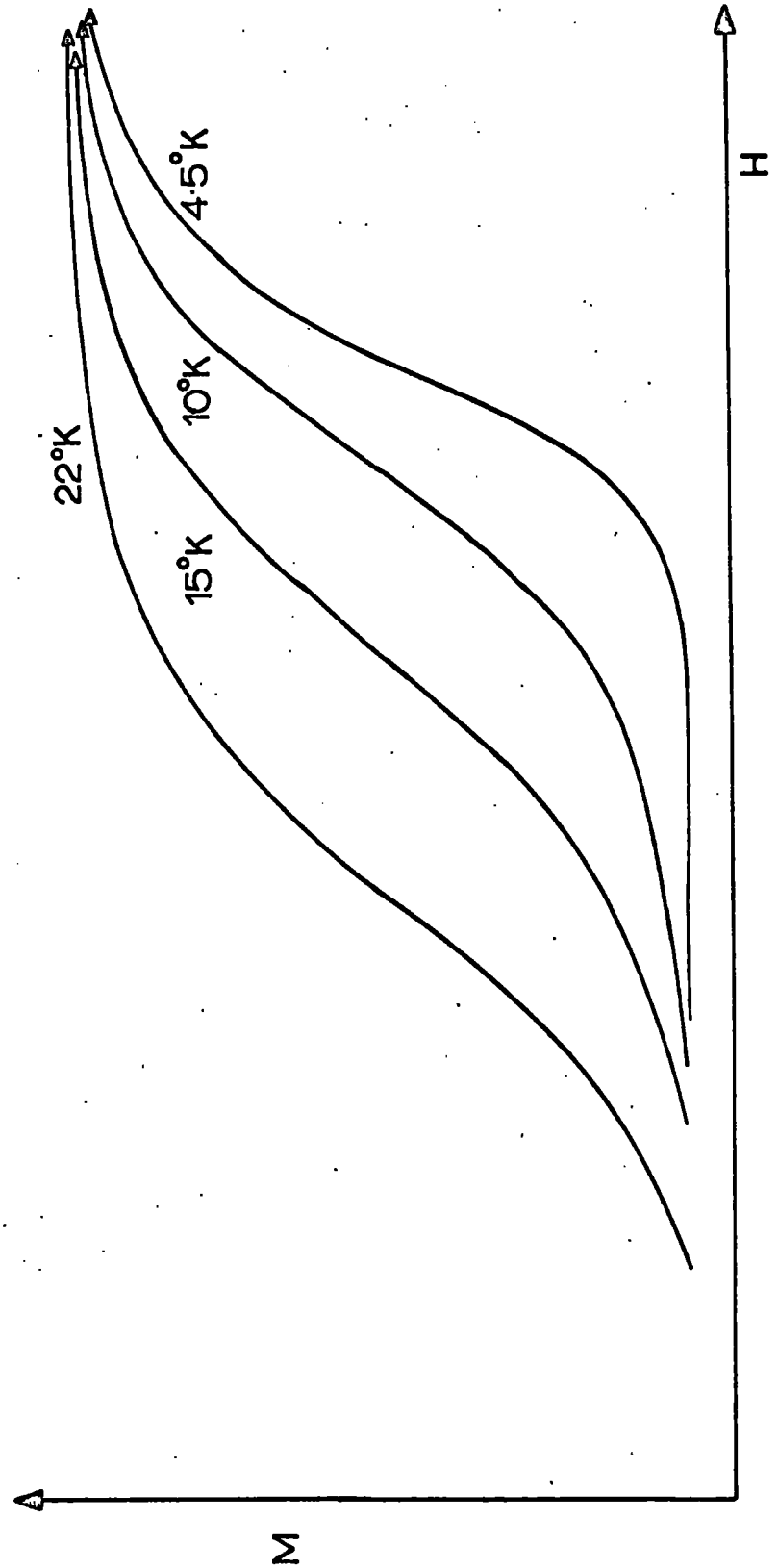

FIG. 4.8 Four initial magnetisation versus field curves for different temperatures

wall motion (and hence H_c), is a function of the ratio of the anisotropy to exchange energies, then one would expect H_c to be temperature dependent. Further, one would expect the critical field to decrease as the anisotropy decreases with increasing temperature, since the exchange energy is almost independent of temperature.

To investigate this dependence of H_c upon temperature, oscillograms of magnetisation against field were taken for the intermediate compound at different temperatures for a constant applied field. The specimen was first cooled to $4.2^{\circ}K$ and then allowed to warm up gradually. To enable quick, direct measurements of the temperature of the specimen to be made, a Solatron digital voltmeter was used to measure the thermal e.m.f. in preference to a potentiometer.

Four of the initial magnetisation curves at different temperatures for the same applied field are drawn in Figure 4.8. Figure 4.8 shows that not only does H_c decrease with increasing temperature as proposed above but also the magnetisation growth with applied field below H_c increases with temperature, whilst the gradient of the curve, after H_c, decreases.

This may be explained by considering the effect of the increase of thermal energy given to the spins. The increase in energy means that the probability that the wall can move from its pinning site (see Chapter 5) is enhanced. The magnetisation at a given field therefore increases and, consequently, the magnetisation at the critical field is more appreciable. As a result, the specimen is nearer saturation at the critical field at higher temperatures. This means that after the critical field the magnetisation does not increase as much as

it did for the lower temperatures. This is why the gradient of the lines after the critical field decrease with increasing temperature.

The measurements of critical field at different temperatures were repeated for different maximum applied fields, and the resultant variations are shown in Figure 4.9 for DyCoNi.

The fact that the lines are parallel in Figure 4.9 shows that the rate at which H_c decreases with increasing temperature is independent of the rate at which the magnetic field is applied.

This is further notified by the measurements performed upon another specimen in the series, $Dy\ Co_{0.5}\ Ni_{1.5}$, as shown in Figure 4.10. Furthermore, the rate at which the critical field decreases with temperature for $Dy\ Co_{0.5}Ni_{1.5}$ is equal to, within experimental error, that for the intermediate compound. This should be expected since the size of the anisotropy determines the size of the critical field (neglecting the exchange energy as mentioned above) and, since the major contributor to the anisotropy is the cobalt ions, then the variation of H_c for both compounds is governed by the variation of the anisotropy of the cobalt ions with temperature in both instances.

4.4 RATE OF CHANGE OF MAGNETISATION MEASUREMENTS

To study further the mechanism by which the magnetisation increases below the critical field in the materials under consideration, particular attention was given to that part of the magnetisation curve. From Figure 4.1 it is obvious that the gradient is very small in this region. This makes it difficult to take accurate measurements of the magnetisation or

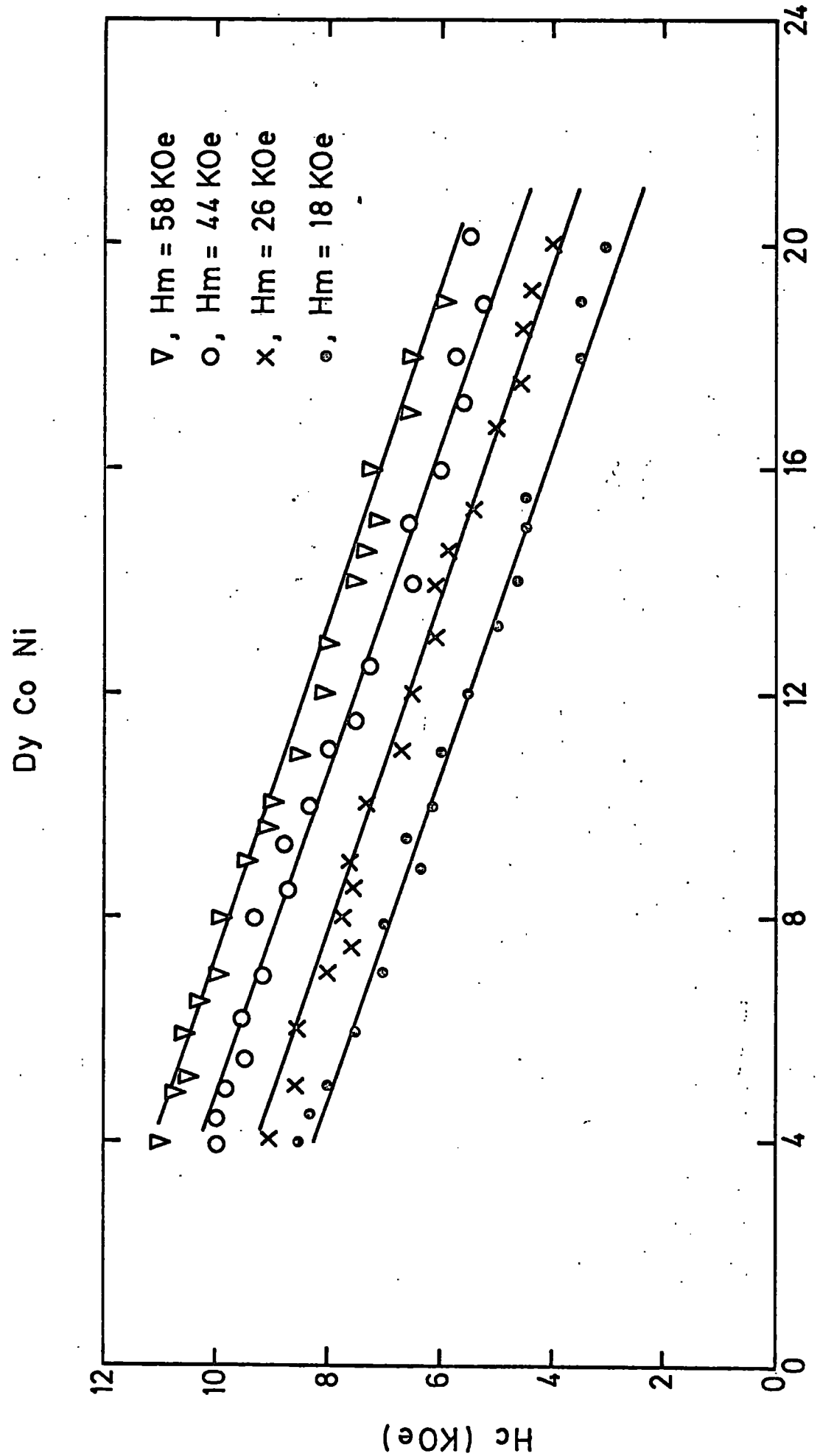

FIG. 4.9 Variation of critical field with temperatures at different maximum applied fields for DyCoNi

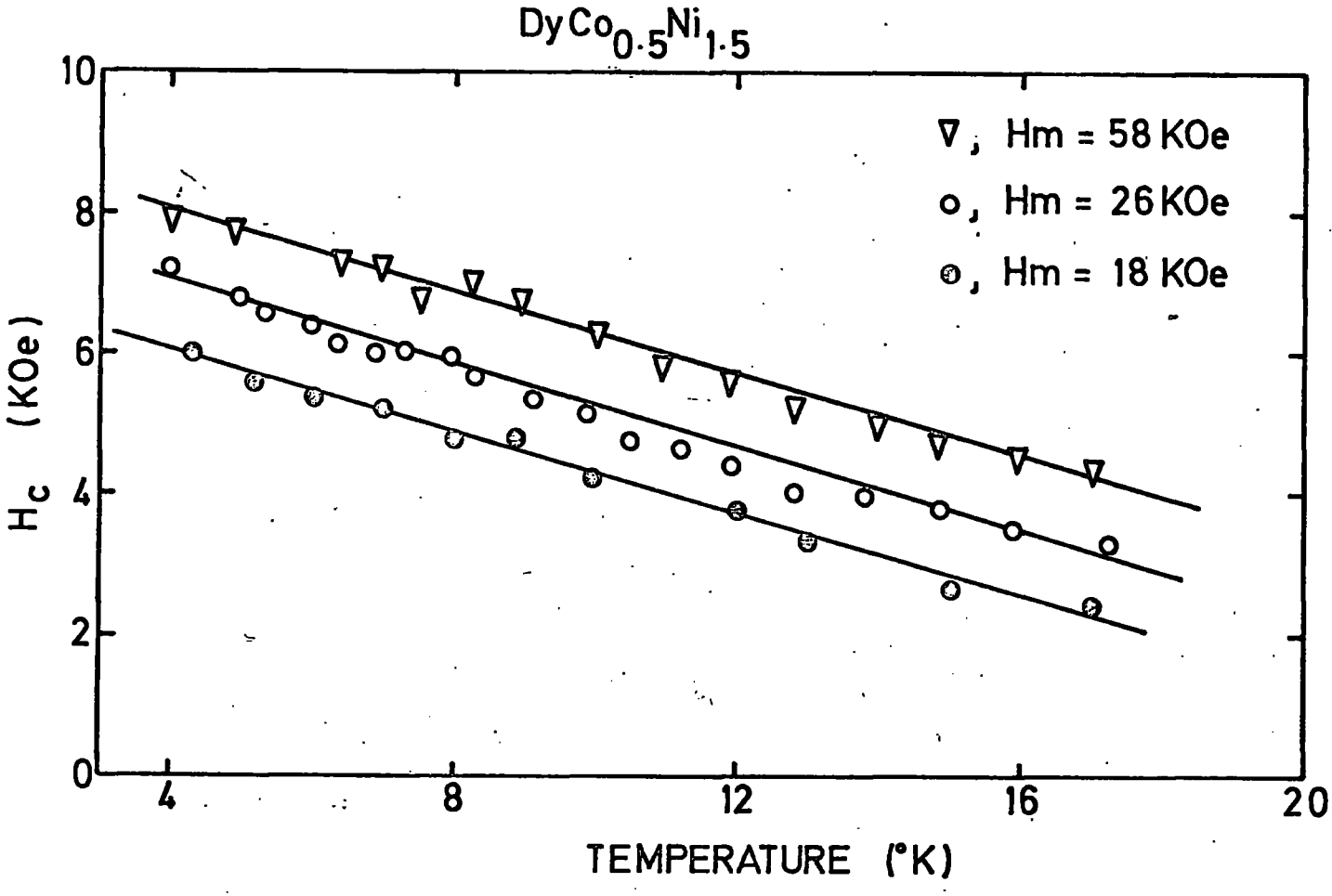

Fig. 4.10 Variation of critical field with temperature at different maximum applied fields for $DyCo_{0.5}Ni_{1.5}$

magnetisation rate ($\frac{dM}{dt} = \frac{dM}{dH_i} \times \frac{dH_i}{dt}$) at these low fields.

It was found to be much more accurate if the magnetisation rate was measured directly from the output of the magnetisation pick-up coil. Figure 4.11 shows how the magnetisation rate varies with field. Initially the magnetisation rate is quite small, but it then increases to a peak before decreasing to zero at saturation. The peak corresponds to the mobility of the wall after it has enough energy to overcome the energy barrier to motion and can then move freely through the specimen except for eddy current damping. The value of the field, H_p, at which the peak occurs is not equal to the critical field, H_c, but is just somewhat larger, as is demonstrated in Figure 4.12.

To check that the magnetisation rate measurements are a measure of the domain wall mobility at different fields, the shape of the initial magnetisation rate curve for a given field was plotted in Figure 4.13. For the same specimen at the same temperature, but for fields less than the one used to plot the shape of the curve, the positions and magnitudes of the initial magnetisation rate peaks for different fields were plotted on the same graph (see insert in Figure 4.13). To within experimental error, these points lie on the peak shape for the higher field. We can therefore conclude that the magnetisation rate depends only upon the field at a constant temperature, i.e., interaction between domain walls can be ignored.

Becker(42) has shown that the magnetisation reversal in permalloy tape is achieved by a nearly uniform motion of the domain walls rather than by a change of density of walls. If

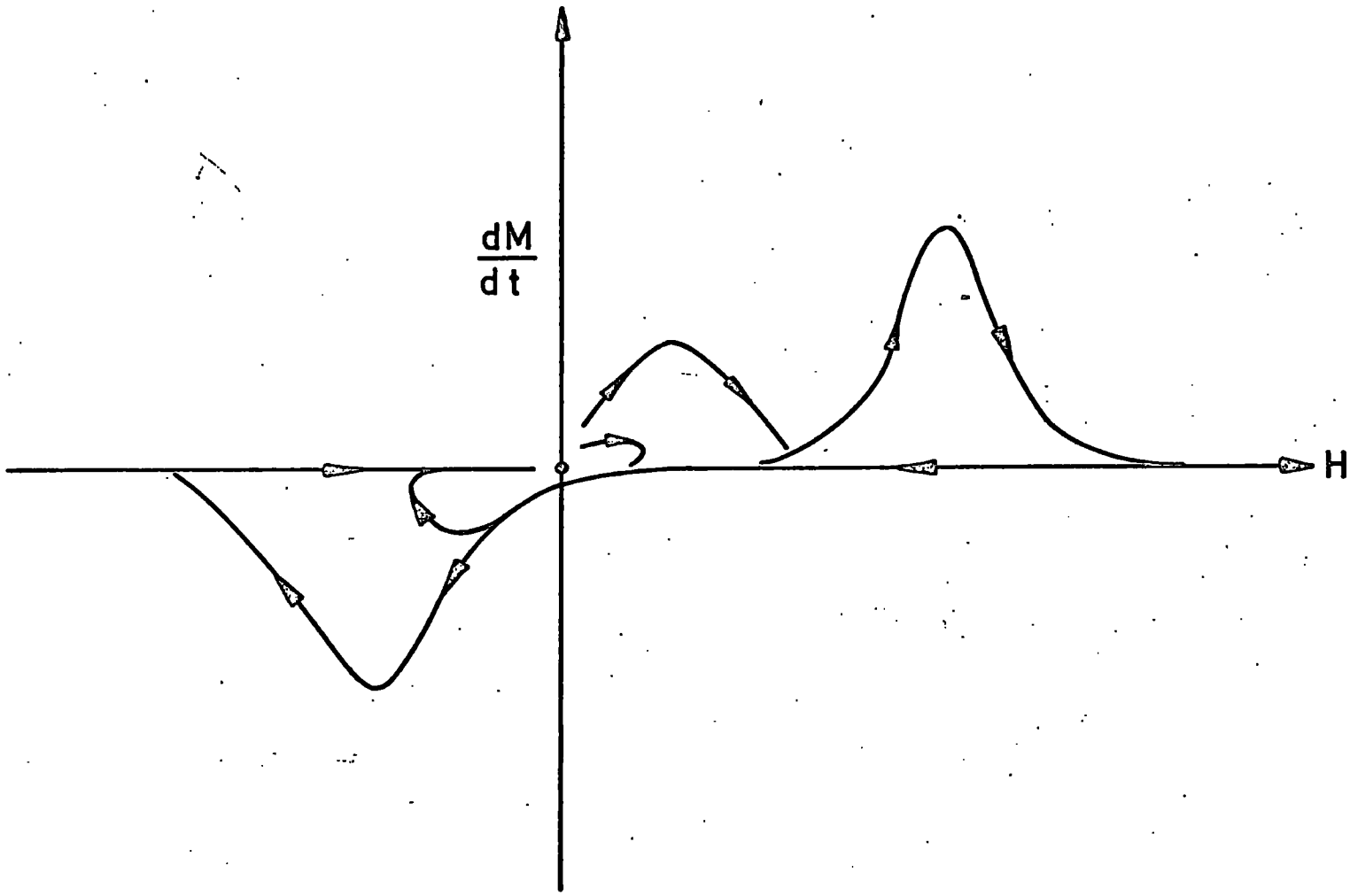

FIG. 4.11 Variation of magnetisation rate with applied field, as the field reverses

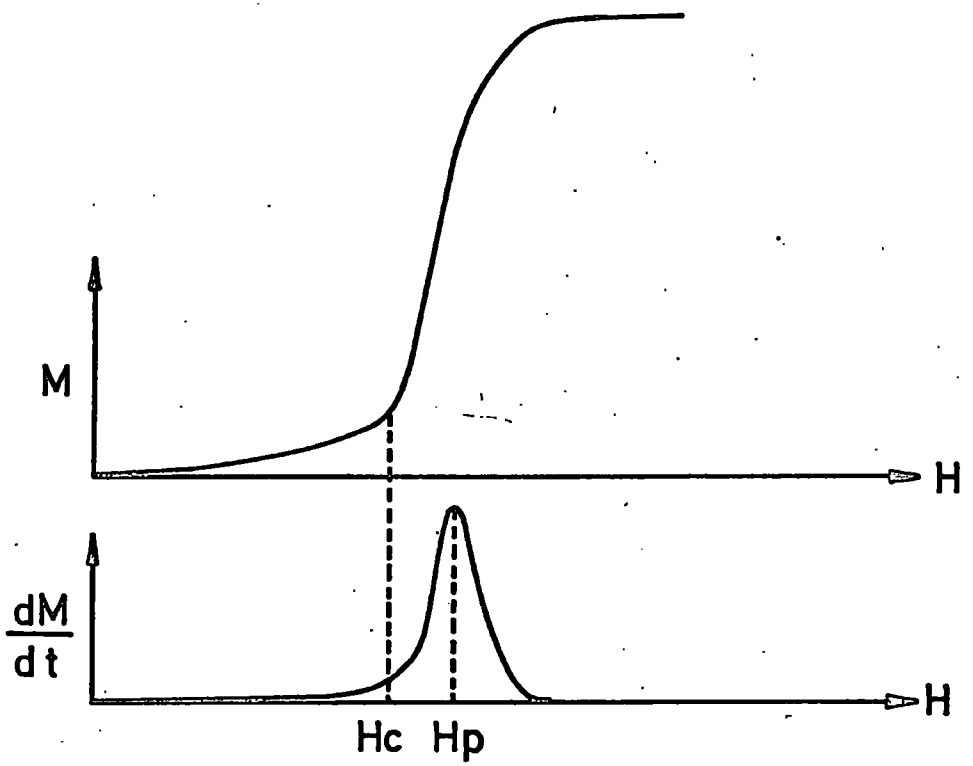

FIG. 4.12

Relation between mangetisation rate and magnetisation of a specimen for small applied fields

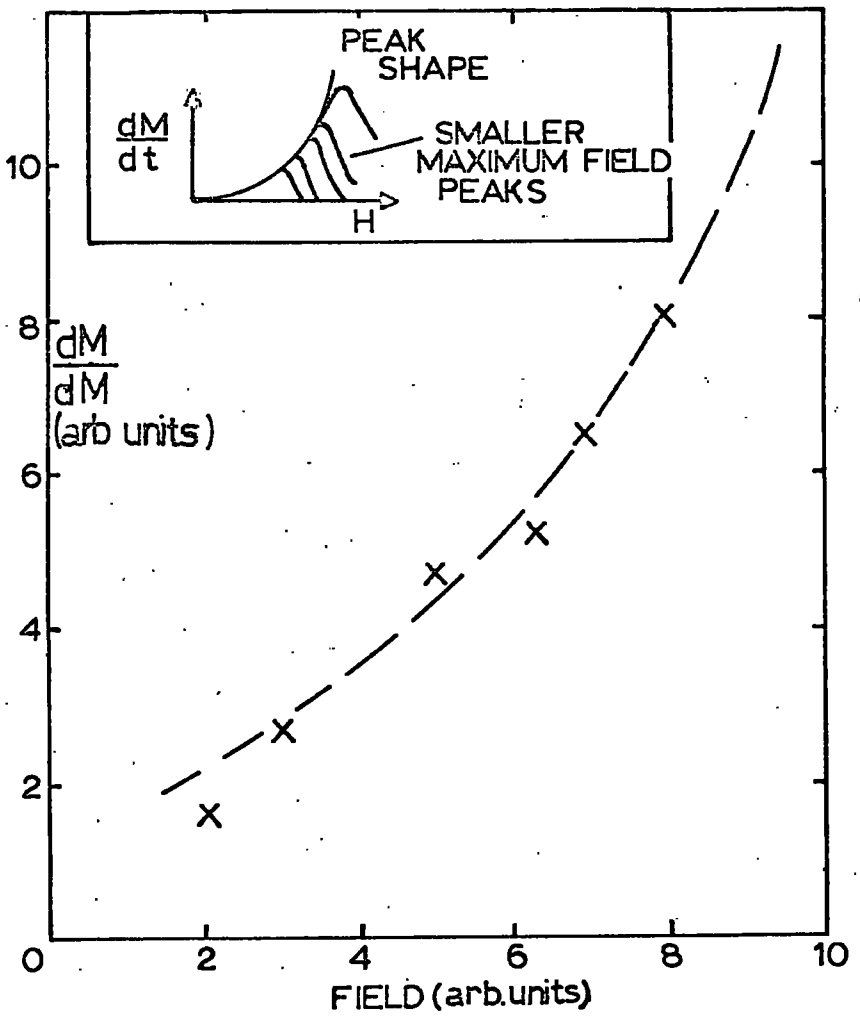
PEAK
SHAPE
dM
dt
SMALLER
MAXIMUM FIELD
PEAKS
H
dM
dM
(arb units)
0
2
4
6
8
10
FIELD (arb.units)

FIG. 4.13

we assume this to be the case in this series of compounds, as seems likely from the preceding paragraph, then not only the peak height but also the peak shape is a representation of the field dependence of the domain wall mobility.

The variations of magnetisation rate with field for the specimen DyCoNi at various temperatures in the range 4.2 to 20°K, for a constant maximum applied field, were measured and are given in Figure 4.14.

As the temperature of the specimen is increased, the initial peak of magnetisation rate remains at the same position on the field axis, H_p, at 10 KOe, but varies in magnitude, dM/dt peak. With a further increase of the temperature of the specimen, however, the peak begins to decrease and occurs at lower fields. This variation is plotted in Figure 4.15 for the intermediate compound.

The variation of the height of the initial peak of magnetisation rate, dM/dt peak, with temperature for a constant maximum applied field is shown in Figure 4.16 for DyCoNi. For a small temperature range, the peak remains constant but as the temperature increases further the peak decreases. This was expected after the results shown in Figure 4.8 and also after noticing that the initial gradient of the magnetisation curve remained constant for a small temperature range in the magnetisation against field oscillograms taken whilst studying the variation of H_c with temperature.

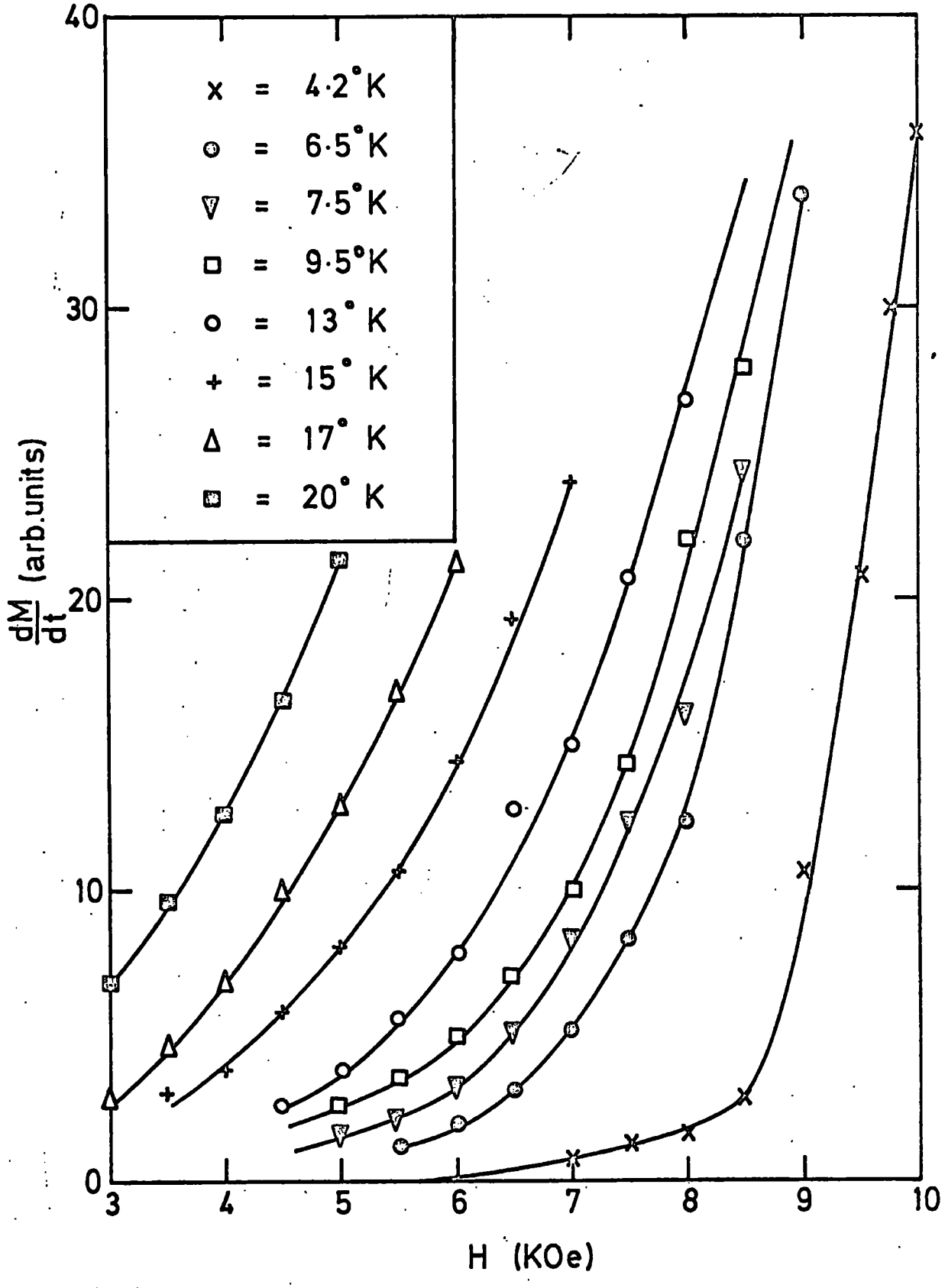

FIG. 4.14

Variations of magnetisation rate with applied field at various temperatures for the intermediate compound, DyCoNi.

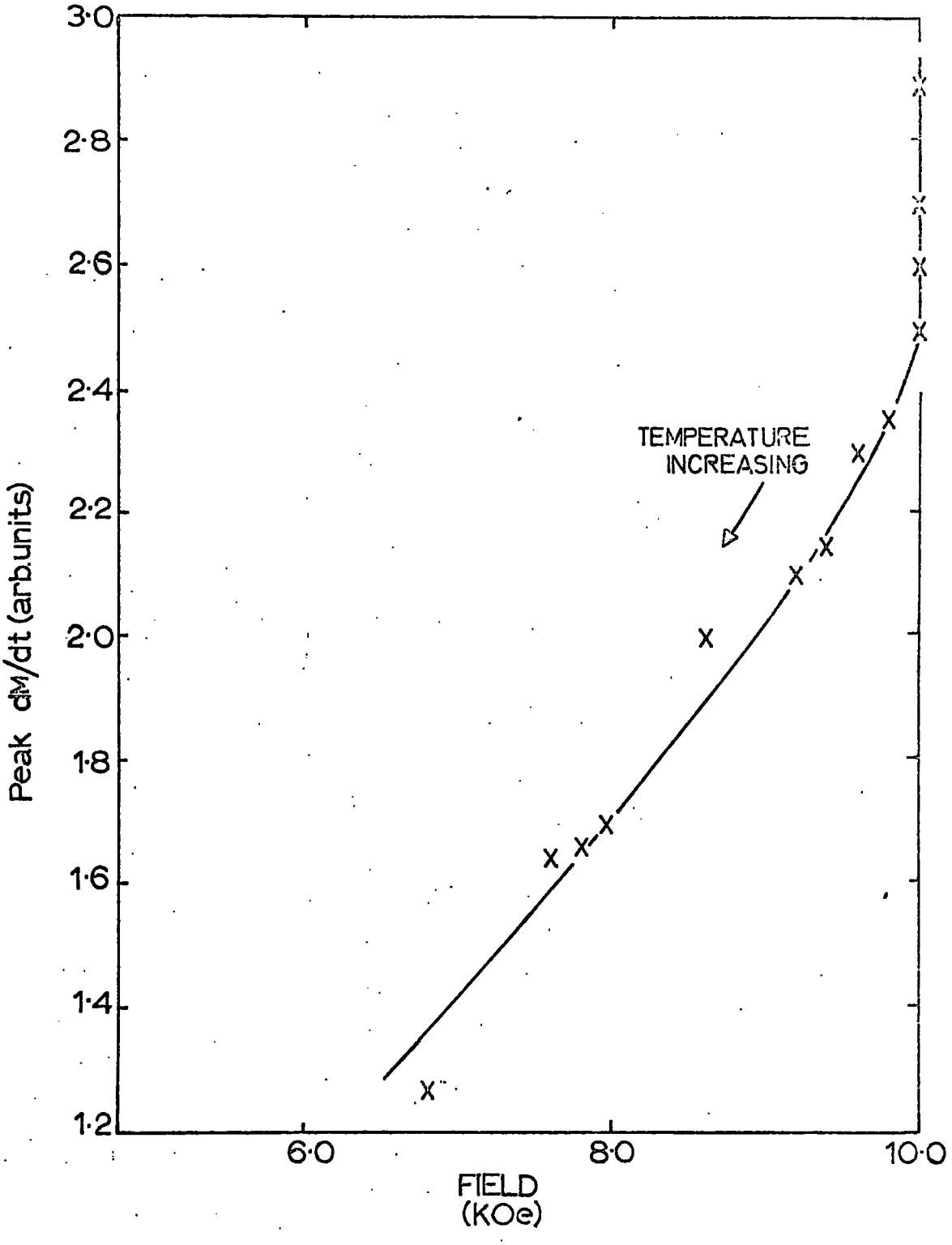
3·0
2·8
2·6
2·4
2·2
2·0
1·8
1·6
1·4
1·2
Peak dM/dt (arb.units)
TEMPERATURE
INCREASING
6·0
8·0
10·0
FIELD
(KOe)

FIG. 4.15

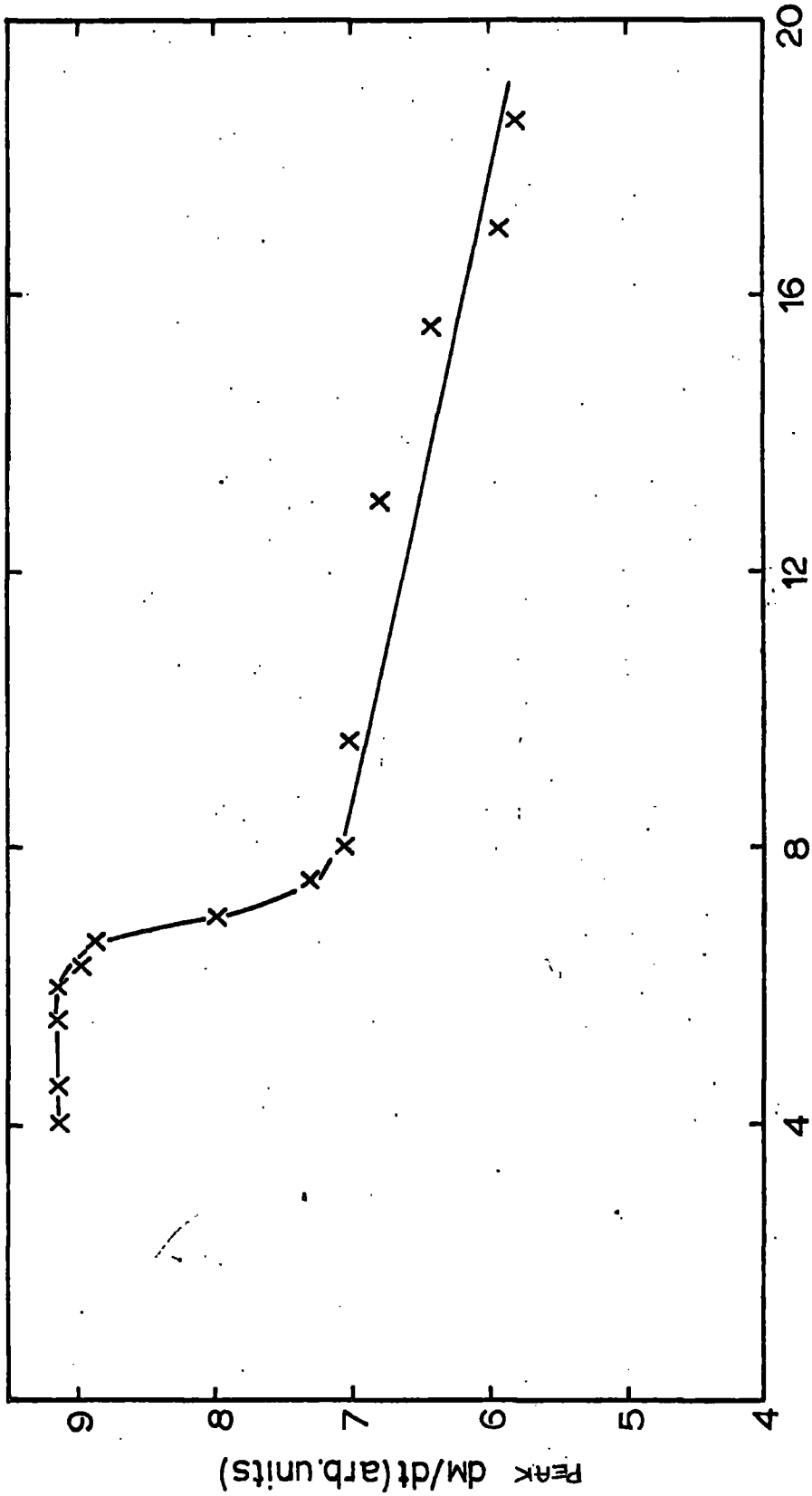

FIG. 4.16
Variation of maximum value of magnetisation rae with temperature for a constant maximum applied field for the intermediate compound.

CHAPTER FIVE

THEORY AND DISCUSSION

5.1 APPLICATION OF NARROW DOMAIN WALL THEORY

Taylor et al(25) have proposed that the critical field observed in the series $Dy(Co,Ni)_2$ may be explained by assuming the domain walls in these materials to be narrow and intrinsically pinned. The variation of the critical field, H_c, with composition, as shown in Figure 4.4, may then be explained by considering the variation of the rate of anisotropy to exchange energy, and therefore the degree of pinning (see Chapter 2) across the series.

From the initial rapid decrease in ordering temperature, and hence exchange energy, as the cobalt content is decreased, Figure 4.5, the net result will be to increase the K/E ratio. This means, therefore, that a larger field is required to release the domain wall from its pinning site, i.e., H_c increases. If the cobalt content is decreased further, however, the ordering temperature changes less appreciably, but now the anisotropy decrease due to the reduction in number of highly anisotropic cobalt ions is the major change, and the K/E ratio will consequently decrease. The critical field decreases towards the nickel rich end of the series, therefore, as shown in Figure 4.4.

A further ratification of the applicability of the narrow domain wall pinning theory is demonstrated by explaining the variation of the critical field for the series $(Dy_{1-x}Tb_x)CoNi$.

Egami(22) has measured the intrinsic coercivity for both

pure Dysprosium and pure Terbium. He found them to be 1.1 KOe and 30 Oe at 4.2°K respectively. This means, therefore, that the domain wall is more strongly pinned in Dysprosium than it is for Terbium. One would therefore expect a decrease in critical field as the Terbium content of the above series was increased. That this is found to be the case, Figure 4.7, further strengthens the validity of the use of the narrow domain wall pinning theory for the materials considered in this study.

5.2 THE SHAPE OF THE INITIAL MAGNETISATION CURVE

Before the processes governing the mobility of the domain wall at fields below the intrinsic coercivity are considered, the shape of the whole of the initial magnetisation curve in the first quadrant of the hysteresis loop is described and accounted for.

The shape of the family of hysteresis loops shown in Figure 4.2 can be understood if one considers the behaviour of the time-dependent magnetisation in time varying fields. The variation of the applied magnetic field is given in Appendix C. For present purposes, however, where both the specimen and pick-up coil assembly are in a fixed position on the Z axis of the magnet (see Figure 3.2), we need only consider the variation of the applied field with time. This may be expressed as:-

$$H = H_m \sin wt$$

where H_m is the first maximum field (as we are only concerned with the initial magnetisation curve here), $w = 2\pi f$, where f is the frequency of the field, and t is the time after the start of the discharge.

If we now consider the initial magnetisation curve for the

series, as represented diagramatically in Figure 5.1, it is apparent that it is possible to divide the curve into two separate regions:-

(a) below H_c, where the magnetisation is increasing slowly with the field and $4\pi\frac{dM}{dt} < \frac{dH}{dt}$ and,

(b) above H_c, where the magnetisation is increasing much more rapidly and is such that $4\pi\frac{dM}{dt} > \frac{dH}{dt}$.

Between these two regions, at H_c $4\pi\frac{dM}{dt} = \frac{dH}{dt}$, i.e., the magnetisation is increasing with time at the same rate as the field. If we use this as a definition of the critical field, it becomes apparent why the values for H_c in pulsed fields are much larger than those obtained in static fields, since dH/dt is much greater, and consequently a higher field is needed before the condition $4\pi\frac{dM}{dt} = \frac{dH}{dt}$ is satisfied.

This is also the reason for the decrease in coercivity in these materials as the field is reversed since, on cycling, the subsequent maximum decreases from one half cycle to the next. As a result dH/dt will decrease on cycling since:-

$$\frac{dH}{dt} = H_m w \cos wt$$

$$\text{i.e.,} \quad \frac{dH}{dt} \propto H_m$$

Therefore, H_c is not a direct function of H_m (Figure 4.3), but is dependent upon the rate of change of field.

The time taken, t_c, for the magnetisation rate to increase to the value of the sweep rate, i.e., $\frac{dH}{dt}$, at H_c also varies with composition and with the rate of change of field since:-

$$H_c = H_m \sin w t_c$$

$$\therefore \quad t_c = \frac{1}{w} \sin^{-1} \frac{H_c}{H_m}$$

$$\sim \frac{1}{w} \frac{H_c}{H_m} \qquad \text{for } H_c < H_m$$

Table 5.1 shows the variation of t_c for the composition range at $4.2^{\circ}K$ for a fixed maximum field (and hence sweep rate).

5.3 INCREASE IN MAGNETISATION BELOW H_c

Whether the magnetisation increases below the critical field depends upon P, the probability that the domain wall is able to move at these fields. The magnetisation of a specimen at time, t, for the initial part of the hysteresis loop, i.e., from zero magnetisation to saturation, may be expressed approximately as:-

$$M(t) = M_o[1 - \exp(-t/\tau)]$$

where M_o is the equilibrium magnetisation at the applied field and temperature. For the large fields employed in this study M_o may be replaced by M_s, the saturation magnetisation.

τ in the above expression is a time constant and is inversely proportional to P. From the above expression it is clear that for this region we may write, to a first order:-

$$\frac{dM}{dt} \propto \frac{1}{\tau}$$

$$\therefore \quad \frac{dM}{dt} \propto P$$

i.e., the increase in magnetisation is directly related to the probability of the domain wall moving one lattice spacing.

Composition	t_c (msecs)
$Dy\ Co_2$	.049
$Dy\ Co_{1.75}\ Ni_{0.25}$	.092
$Dy\ Co_{1.5}\ Ni_{0.5}$	.105
Dy Co Ni	.110
$Dy\ Co_{0.5}\ Ni_{1.5}$	.108
$Dy\ Ni_2$	.074

TABLE 5.1

Variation of time taken to reach the critical field with composition

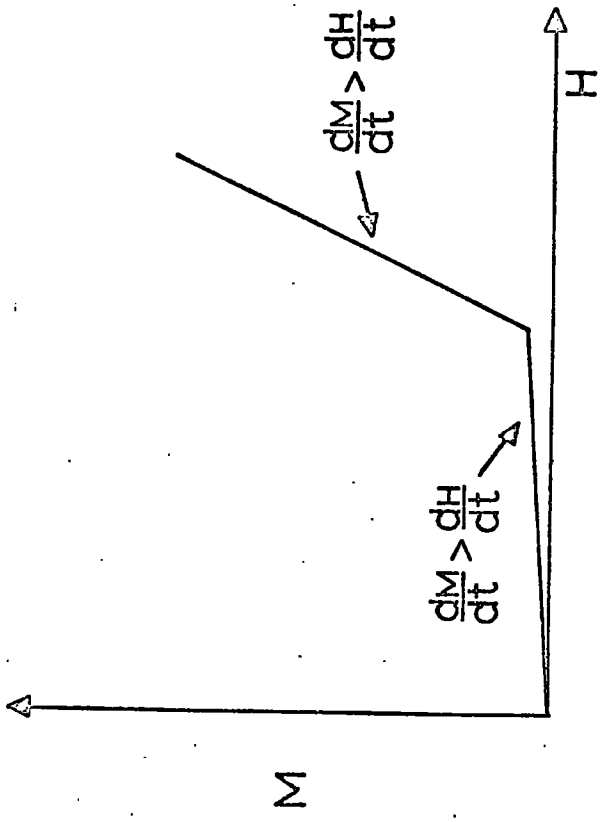

FIG. 5. 1

The initial increase in magnetisation in the hysteresis loops and the increase in magnetisation rate before the peak is reached (at which the wall has completely escaped its pinning site) mean that P is finite for these low values of field and that the wall is not completely pinned but its mobility reduced.

As mentioned in Chapter 1, the present problem of determining the mechanism of magnetisation growth below the critical field is analogous to that of the escape of dislocations from states bound by the Peierl's potential. Gilman(43), Glen(44), Mott(45) and Weertmann(46) have considered this problem. They have found that the process governing the creep of dislocations at high temperatures is not necessarily the same as the predominant process at lower temperatures. That is, the thermal activation process usually used to explain the movement of dislocations is not apparent at low temperatures due to the larger effect of the dislocation tunnelling through the Peierl's potential.

The fact that the magnetisation rate remains constant for a small finite temperature range, i.e., is temperature independent, as illustrated in Figure 4.16, suggests that a comparison between the present problem and that of dislocations may be viable.

Using this analogy, Egami(26) has developed a theory of domain wall diffusion at low fields, i.e., less than the critical field, in terms of thermal activation at the higher temperatures and tunnelling of the wall through the potential barrier at low temperatures (near liquid helium temperature).

Although the domain wall is not a particle in the usual

sense, since the motion of the wall does not result in any transport of matter, the dynamics of the wall closely rememble those of a particle with finite mass. This is due to the gyromagnetic property of the spins involved in domain wall motion (see section 2.2.1). This isomorphism can be extended to predict the tunnelling of the domain wall through an energy barrier such as the one obtained in the materials under consideration, as shown by Egami.

Taylor(25) has also proposed a model of thermal activation to explain the observed increase in mobility of the domain wall. The expression used by Taylor, however, is not identical to that used by Egami. Further, Barbara et al(24) have also proposed an empirical expression to account for the magnetisation rate increase in DyCoNi following from the analogy they draw with the movement of domain walls in the ferroelectric barium titanate(47).

These models are described further below, and their applicability is tested using the results obtained.

5.4 TAYLOR'S MODEL

5.4.1 Thermal Activation

Taylor(23) was the first to notice the phenomenon of magnetic wall diffusion below the critical field and the subsequent time-dependent magnetisation of the specimen, DyCoNi. This phenomenon, mow referred to as the magnetic after effect, was explained by Taylor as due to the magnetic moments needing energy, which he considered may be derived from the application of a magnetic field or from thermal excitation, to increase

the domain wall mobility. Therefore, by considering the energetics of the situation, Taylor proposed that the probability that the domain wall will be able to move one lattice spacing, and hence the magnetisation rate resulting from the wall motion (see section 5.3) will be given by the expression:-

$$P = A \exp\left\{-\frac{(\Delta E - 2MH)}{KT}\right\} \quad \ldots\ldots 5.1$$

where A is a constant of proportionality, K is Boltzmann's constant. 2MH is the energy given to the molecular magnetic moment due to the application of the field, and KT is the thermal energy of the spin.

From equation 5.1, it is possible to understand the initial shape of the hysteresis curve and its change with temperature. If, at constant temperature, the applied field is such that the energy of the magnetic spins due to the application of the field is less than the height of the energy barrier, ΔE, to domain wall motion then the inertia of the wall will be appreciable. As a result, the magnetisation will not increase markedly for small applied fields. Increasing the field, however, will also increase the energy of the spins, and at some particular field the spins will have enough energy to surmount the energy barrier. The domain wall will then be able to move through the specimen unrestricted except for eddy current damping until saturation is reached. Referring to Figure 4.1 it is clear that equation 5.1 can be used to describe the variation of magnetisation with field at constant temperature.

Using this model, it is also possible to account for the observed changes in the initial magnetisation against field curve with temperature as obtained in Figure 4.8. From

equation 5.1 it is obvious that as the temperature is raised the probability that the wall will move one lattice spacing, P, will become larger. The mobility of the wall at a fixed field will therefore increase, resulting in a steeper initial gradient of the curve. As the wall becomes more mobile, the condition used to define the critical field, i.e., the field at which the magnetisation rate is equal to the rate of change of field (see section 5.2), is satisfied at smaller fields, and therefore H_c decreases, Figure 4.9.

It must be remembered, however, that the energy barrier, ΔE, is also temperature dependent due to its dependence upon the anisotropy of the material. Therefore, as the temperature is raised, the reduction of the energy barrier to domain wall motion leads to an increased mobility of the wall. It is therefore for these two reasons together that the initial magnetisation curve changes as it does with temperature.

The magnetisation rate is directly proportional to the probability of the domain wall being able to move. Therefore, from the variation of the magnetisation rate with both temperature and field, it is possible to test the validity of Taylor's model directly. Figure 4.14 is a plot of magnetisation rate, $\frac{dM}{dt}$, against applied field for DyCoNi at various temperatures between 4.2 and 20°K. To check the relationship 5.1 directly, the magnetisation rate has been re-plotted on a logarithmic scale in Figure 5.2. It is immediately apparent that the logarithm of the magnetisation rate, $\ln \frac{dM}{dt}$, is linearly dependent upon the applied field for the whole temperature range considered here.

Another striking feature of Figure 5.2 is the gradual

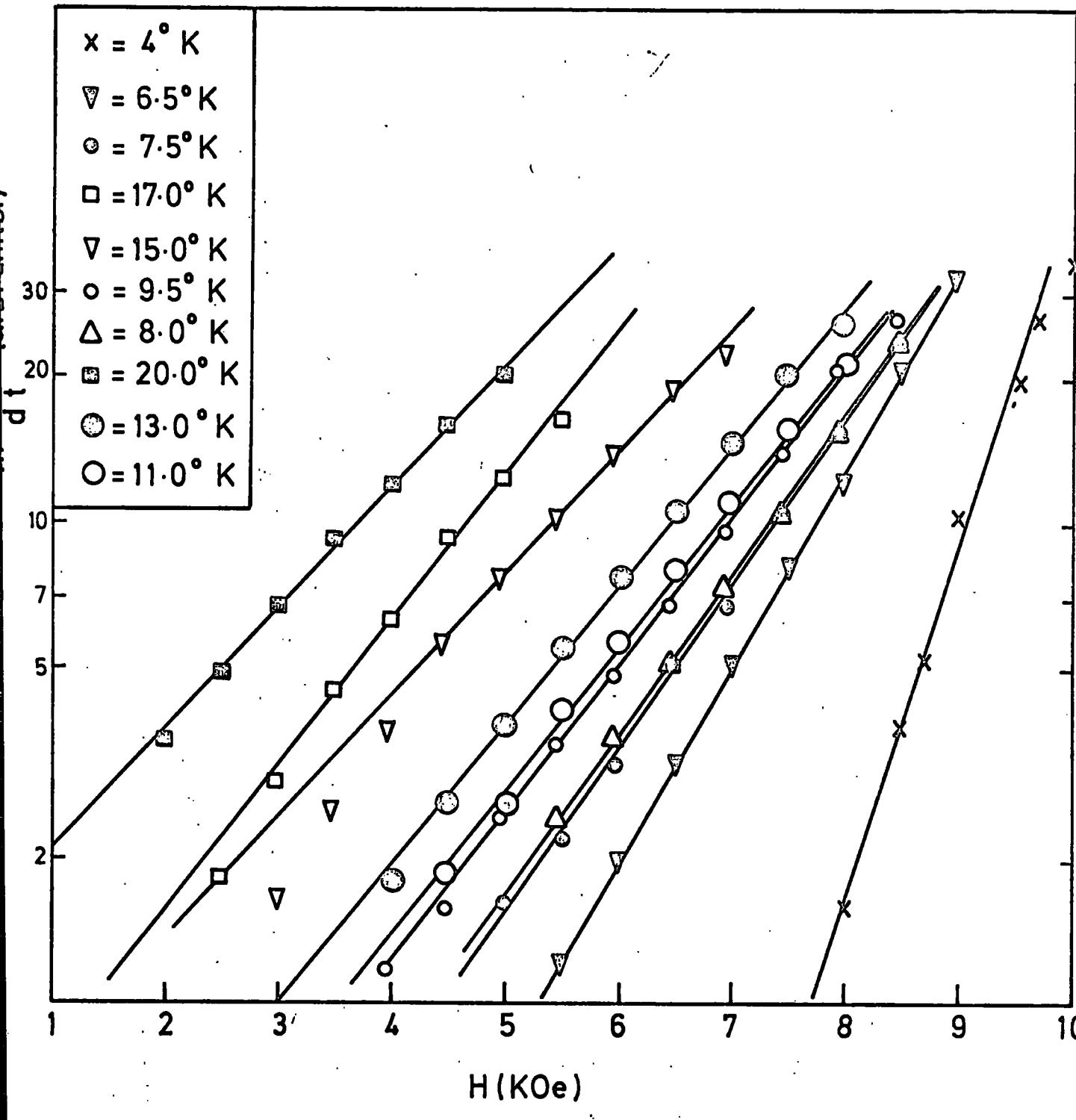
x = 4° K
▽ = 6·5° K
⊙ = 7·5° K
□ = 17·0° K
▽ = 15·0° K
○ = 9·5° K
△ = 8·0° K
▣ = 20·0° K
◎ = 13·0 ° K
○ = 11·0° K
30
20
10
7
5
2
1
2
3
4
5
6
7
8
9
H (KOe)

FIG. 5.2

decrease in the gradient of the isotherms as the temperature is increased. This means that an increase in applied field has a greater effect upon the magnetisation rate at lower temperatures than it does at the higher temperatures.

This might be expected keeping in mind the analogy between the present situation and that of bound dislocations as mentioned in the previous section. If the two situations are analogous, then it would be expected that tunnelling would be the predominant process at the lower temperatures and thermal activation to control domain wall motion at higher temperatures.

Therefore, as the temperature is decreased, one would expect the increase in the gradient of the lines in Figure 5.2 since tunnelling is a strong function of applied field, as will be shown subsequently.

Further evidence is obtained for the supposition that thermal activation gives way to tunnelling at the lower temperatures by plotting the magnetisation rate, again on a logarithmic scale, against the reciprocal of absolute temperature, as in Figure 5.3. The marked discontinuity at the temperature, $T \sim 13^{\circ}K$, infers that the process governing the change of magnetisation rate with temperature is different at temperatures above 13° than for those below $13^{\circ}K$.

Again, drawing the analogy with dislocations, one can assume that the process involved for temperatures higher than $13^{\circ}K$ is thermal activiation. In this temperature region the lines appear parallel, to within experimental error. This means that the temperature changes the magnetisation rate at the same rate independent of applied field for the thermal activation process, as would be expected from equation 5.1.

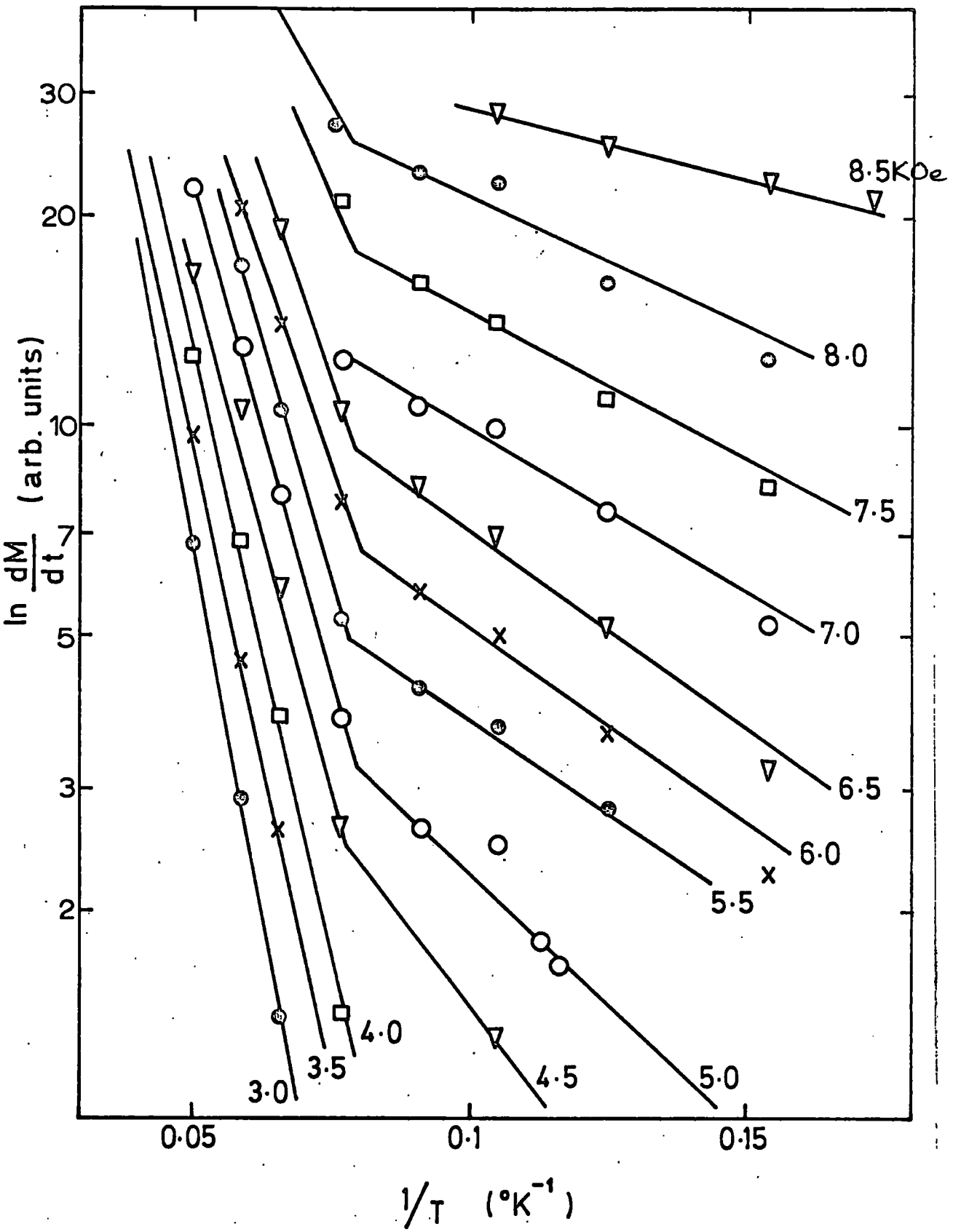
30
20
10
7
5
3
2
ln dM/dt (arb. units)
8·5KOe
8·0
7·5
7·0
6·5
6·0
5·5
5·0
4·5
4·0
3·5
3·0
0·05
0·1
0·15
1/T (°K⁻¹)

FIG. 5.3

Below 13°K it is not so easy to define which process or processes are involved in the change of magnetisation rate. From Figure 5.3 one can see that, although the isofields have a much smaller gradient below 13°K, andhence are not so temperature-dependent as before, they are still temperature-dependent. The degree of this dependence remains the same down to liquid helium temperatures. For these low fields it seems likely that in this temperature region the magnetisation rate is governed by a mixture of both processes, i.e., the magnetisation rate may be thought to be governed by a "thermally assisted tunnelling" process.

For the higher field strength isofields the dependence becomes less marked as can be seen by the reduction in gradient in Figure 5.3. This trend suggests that, for high enough fields, the magnetisation rate will become temperature independent. This is shown to be so in Figure 4.16, which shows the variation of the peak of magnetisation rate (see Figure 4.11) with increasing temperature. It is obvious that the peak magnetisation rate, which occurs at slightly higher fields than those considered in Figure 5.3, is independent of temperature for a small finite range of low temperatures (between 4 and 7°K approximately).

5.4.2 Determination of Molecular Moment

If we assume that equation 5.1 holds for temperatures greater than 13°K, which seems likely from the above arguments, then it should be possible to derive the molecular moment of the intermediate compound using the results given in Figure 5.2.

Referring to equation 5.1, the gradients of the isotherms

in Figure 5.2 will be given by:-

$$\frac{dM}{dt} = A \exp\left\{\frac{-\Delta E + 2MH}{KT}\right\}$$

$$\therefore \quad \ln \frac{dM}{dt} = \ln A \, \frac{-\Delta E}{KT} + \frac{2MH}{KT}$$

$$\therefore \quad \frac{\partial\left(\ln\left(\frac{dM}{dt}\right)\right)_T}{\partial H} = \frac{2M}{KT}$$

Therefore, if the gradient of the isotherms are plotted against the reciprocal of their temperature, as shown in Figure 5.4, then the molecular moment of DyCoNi may be obtained from the gradient, since:-

$$\frac{d\left\{\partial \ln\left(\frac{dM}{dt}\right)_T / \partial H\right\}}{d\left(\frac{1}{T}\right)} = \frac{2M}{K}$$

As would be expected, the points for the lower temperature isotherms deviate from the straight linepredicted above. This is obviously a result of equation 5.1 no longer being applicable to the lower temperature regions. However, using the straight line obtained for the higher temperature isotherms:-

$$\frac{2M}{K} = 1.43 \times 10^{-3} \pm 0.4 \times 10^{-3} \ (\text{KOe}^{-1}{}^{\circ}\text{K})$$

Now, using $1\ \mu_B = 9.3 \times 10^{-21}$ erg/Oe, then,

$$M = \frac{1.43 \times 10^{-3} \times 1.6 \times 10^{-16}}{2 \times 9.3 \times 10^{-21}} \ \mu_B \text{/mol}$$

$$= 12.3 \pm 3.0 \ \mu_B \text{/mol}$$

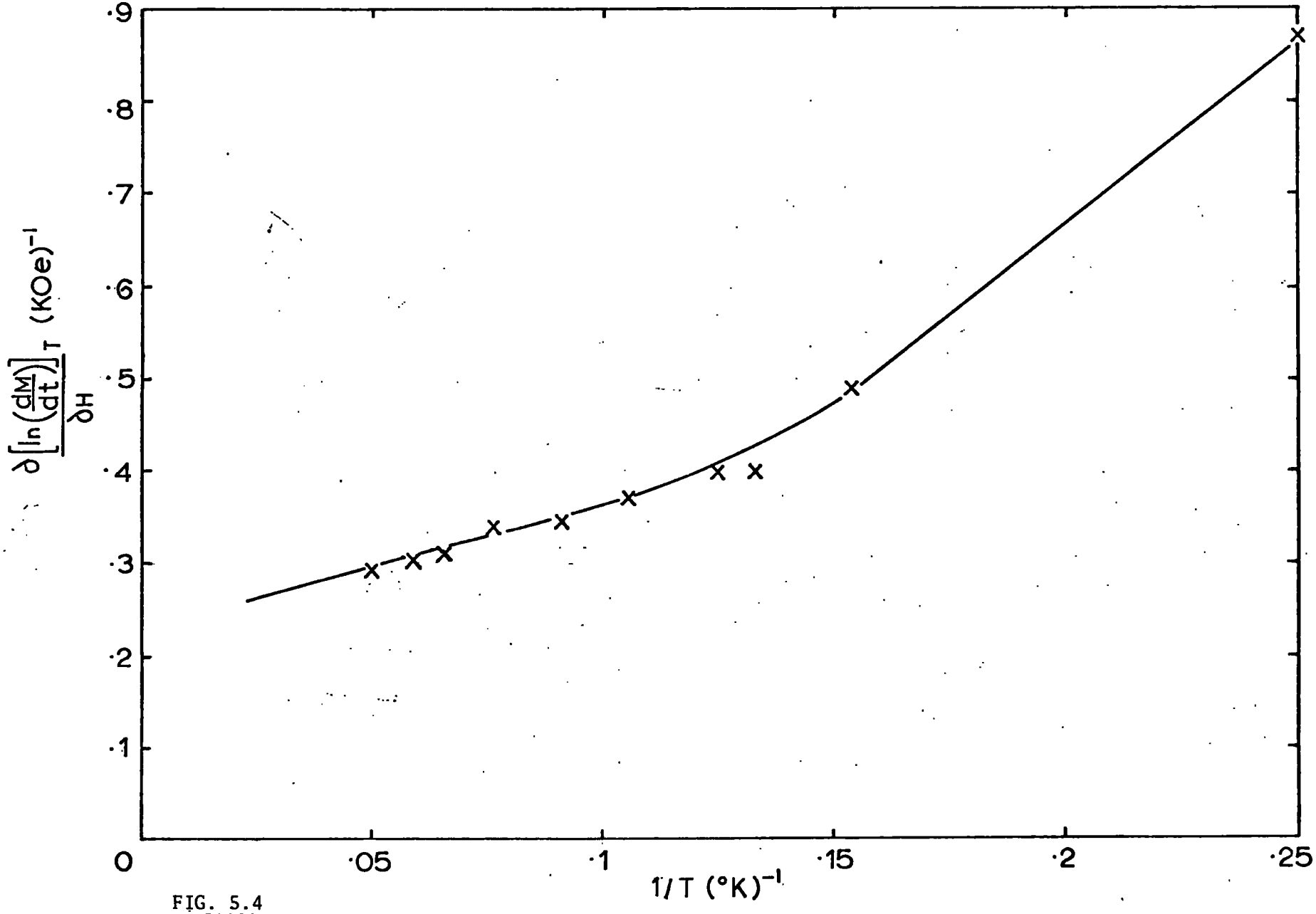

FIG. 5.4

This is in remarkably good agreement with the value of 8 μ_B/molecule derived from magnetisation against field oscillograms (see Figure 4.6).

5.4.3 Tunnelling Probability

Zener(48) has investigated the breakdown of solid dielectrics. He has found that the tunnelling rate for electrons is proportional to the exponential of the inverse of the electric field. Gilman(43) has used the results of Zener's theory and has shown that a relationship between the creep of dislocations, bound by the Peierl's force, and the exponential of the inverse of the applied stress may be used to describe the increase of disloaction creep at low temperatures. Furthermore, Barbara et al(24) have studied the variation of domain wall mobility in DyCoNi at 4.2°K with the exponential of the inverse of the reciprocal field, following the analogy they draw with the motion of domain walls in the ferroelectric varium titanate.

The results obtained by Barbara et al show that this relationship does hold for 4.2°K. They have not repeated the experiment at different temperatures, however. In Figure 5.5 the applicability of the above relationship is shown for different temperatures. From Figure 5.5 it is clear that, although the relationship $\ln \frac{dM}{dt} \propto f(\frac{1}{H})$ does hold for the lower temperatures, it can not be applied to the higher temperature results. This, of course, is to be expected, as tunnelling is only expected to predominate at low temperatures.

Gilman(43) has calculated the transition temperature between the thermal activation and tunnelling processes governing the motion of dislocations bound by the Peierl's force by equating the two rates of increase of creep for both processes.

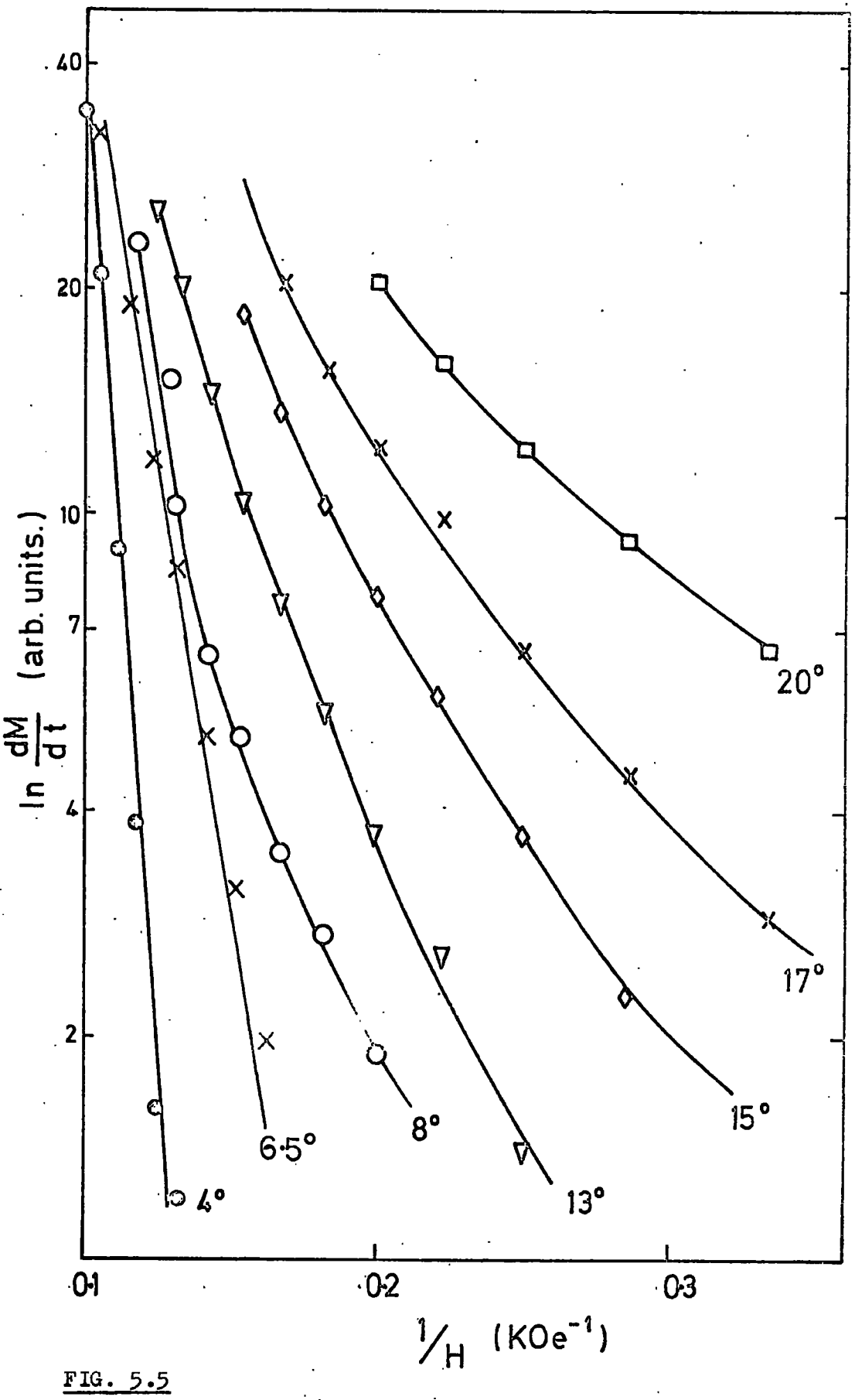

FIG. 5.5

He predicted that, for temperatures below T_t the transition temperature, tunnelling would predominate, where:-

$$T_t = \frac{2sV}{K} \quad \ldots\ldots \quad 5.2$$

s being the local stress, and V the atomic volume. Therefore, by analogy, one would expect the transition temperature in DyCoNi to occur at

$$T_t = \frac{2MH}{K}$$

Using $\frac{2M}{K} = 1.43 \times 10^{-3}$ from Figure 5.5, and assuming an applied field of 10KOe, a value of $14^{\circ}K$ is obtained. Although, as mentioned above, the transition at $13^{\circ}K$ in Figure 5.3 is not necessarily the transition temperature, T_t, it nevertheless suggests that the results are compatible with the theory. It should also be mentioned that the discontinuity in Figure 5.3 seems, to first order, to be independent of applied field. This is in conflict to equation 5.2 and further suggests that the discontinuity is not between thermal activation and solely tunnelling.

5.5 EGAMI MODEL.

5.5.1 Formation of Domain Kinks

Egami(27) has drawn the analogy between the present situation and dislocations much more closely than Taylor. He has suggested that the domain wall does not move in its entirety under the influence of an applied magnetic field, but proceeds by displacement of small sections of the wall. Once such a

displaced section is formed, it may spread across the whole area of the domain wall with very little energy being expended, thereby resulting in the whole domain wall being displaced. This situation is analogous to the formation of kinks in dislocations, and the displaced areas of the domain wall will therefore be referred to as kinks.

Therefore, using the above argument as his basis, Egami has developed a theory of nucleation and growth of kinks to predict how the magnetisation and magnetisation rate of materials with narrow domain walls will vary with an applied magnetic field at various temperatures.

Egami has considered the case for a perfect crystal, i.e., no lattice defects. He has shown that kinks may be formed at any place along the domain wall - homogeneous nucleation, or at specific sites such as at the surface of the crystal, at intersections of walls, or at spike domains in uniaxial crystals - this situation is referred to as heterogeneous nucleation. However, due to the strong stray fields at the surface, surface nucleation is inhibited unless the stray field energy is less than the anisotropy energy. Similar strong stray fields occur at the spike domains, and therefore nucleation will not occur. The kink energy is unlikely to be affected by intersecting domain walls, and therefore following these considerations it is believed that homogeneous nucleation is dominant in the domain diffusion process.

The most likely shape for the nucleus is that of a disc as shown schematically in Figure 5.6.

5.5.2 Thermal Activation Model

Considering the domain wall as a continuous sheet and

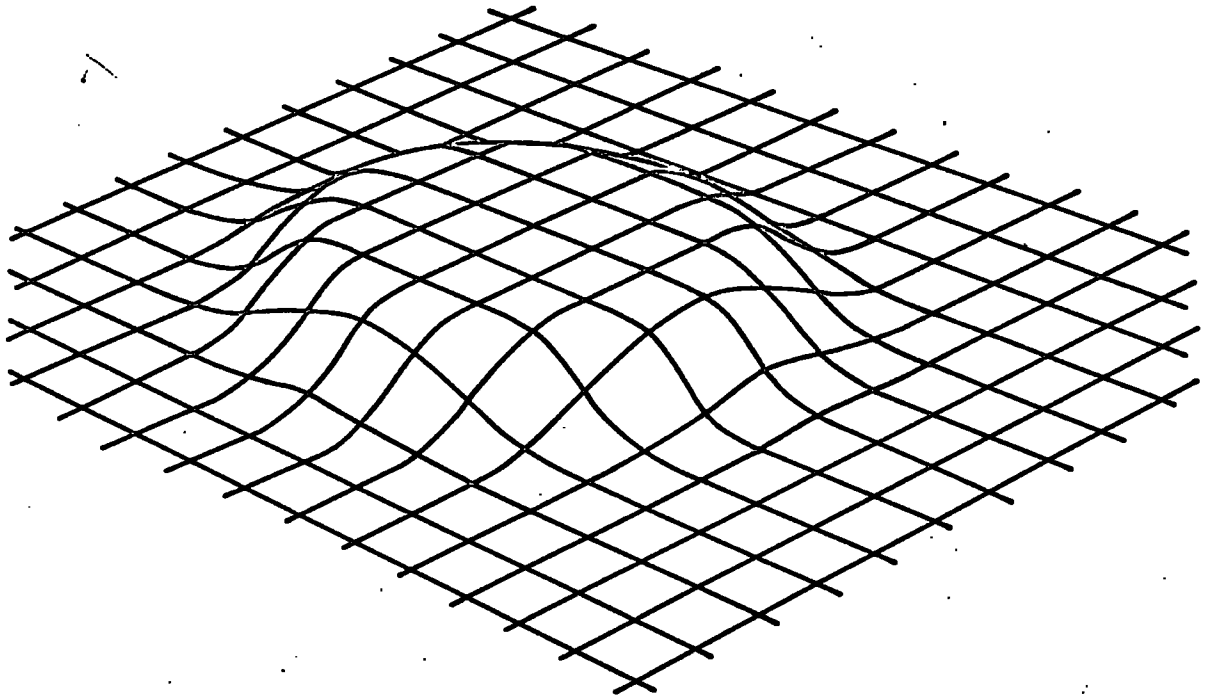

FIG. 5.6

A pictoral view of a disc shaped nucleus in a domain wall (from Egami(27))

and introducing the energy barrier, similar to the Peierl's potential, as a potential dependent only upon the position of the domain wall with respect to the atomic sites, Egami has shown that the activation energy for the homogeneous nucleation process is proportional to the reciprocal of the applied field. Using a micro-magnetic continuum approximation to describe the domain wall kinks, Egami has found that the activation energy, E_e, for the homogeneous nucleation process should be given by:-

$$E_e = <57^2 J \frac{16}{n} \frac{H_c}{H} G_{Th}\left(\frac{H}{H_c}\right) \quad \ldots\ldots \quad 5.3$$

where $G_{Th} \frac{H}{H_c}$ is a function which approaches unity as H goes to zero and is zero for $H = H_c$, n is the domain wall width in terms of the lattice constant.

The dependence of the nucleation activation energy upon the reciprocal of the applied field may be understood simply if one considers a disc-shaped nucleus of radius, r. The kink energy will be given by $2\pi r E_k$, where E_k denotes the kink energy per unit length. Therefore, in an applied magnetic field, H, the energy associated with the nucleus, E_n, is given by:-

$$E_n = 2\pi r E_k - 2\pi r^2 MH$$

where M is the magnetisation per unit area of the atomic layer, and hence the term $2\pi r^2 MH$ is the Zeeman energy term.

E_n will therefore be a maximum at E_c given by:-

$$\frac{dE_n}{dr} = 0$$

$$\therefore \quad 0 = 2\pi\delta - 4\pi r_c MH$$

$$\therefore \quad r_c = \frac{\delta}{2MH} \qquad \ldots\ldots\ldots 5.4$$

$$\therefore \quad E_c = \frac{\pi\delta^2}{2MH} \qquad \ldots\ldots\ldots 5.5$$

$$\text{i.e.,} \quad E_c \propto \left(\frac{1}{H}\right)$$

Equation 5.5 is in agreement with equation 5.3 if one takes $G_{Th}(H/H_c)$ as unity, i.e., small fields, and uses:-

$$E_k = \frac{4}{a}\left[\frac{\leq 57^2 \; J. \; V_1}{n}\right]^{\frac{1}{2}}$$

as the kink energy where V_1 is the height of the Peierl's potential.

Following this treatment, Egami has predicted that the domain wall mobility will be proportional to the exponential of the inverse of the magnetic field, viz:-

$$\frac{dM}{dt} \propto \exp\left\{\frac{16}{n} \; \frac{\leq 57^2 \; J}{KT} \; \frac{H_c}{H} \; . \; G_{Th}\left(\frac{H}{H_c}\right)\right\} \quad \ldots\ldots 5.6$$

This is in direct contrast to the dependence upon the exponential of the applied magnetic field as postulated by Taylor. In fact, it has the same form as the relationship used by Taylor for the low temperature, quantum mechanical tunnelling, situation. Referring to Figure 5.5, the relation- above

ship appears to hold for the low temperature isotherms but not for the higher temperature isotherms. This is in direct contrast to what one would expect of a thermal activation model. Figure 5.7 is a plot of the magnetisation rate, again on a logarithmic scale, against the reciprocal of the applied magnetic field multiplied by the absolute temperature of the specimen, i.e., 1/HT, for temperatures below 13°K.

For this plot the linear relation is obtained as expected following equation 5.6. For temperatures above 13°K, however, as in Figure 5.8, the points lie on a common straight line, almost parallel to those shown in Figure 5.7, for high magnetisation rates. These deviations may result from the low magnetic fields employed since the kink will contain magnetic free dipoles unless it runs parallel to the magnetisation in both of the domains separated by the domain wall and kink. Therefore, the effective field inside the nucleus will be smaller than the applied field and may introduce errors at low field measurements. Bearing this in mind, one might be able to consider the isotherms in Figure 5.5 to be straight lines at higher fields which deviate at lower fields.

5.5.3 Tunnelling Probability

Egami has considered the quantum mechanical tunnelling of the domain wall through the barrier potential at low temperatures. The rate at which the wall tunnels through the barrier is strongly dependent upon the magnetic field. This is due to the reduction in height of the barrier and also the decrease in width of the barrier caused by the application of a magnetic field. Figure 5.9 is a schematic representation

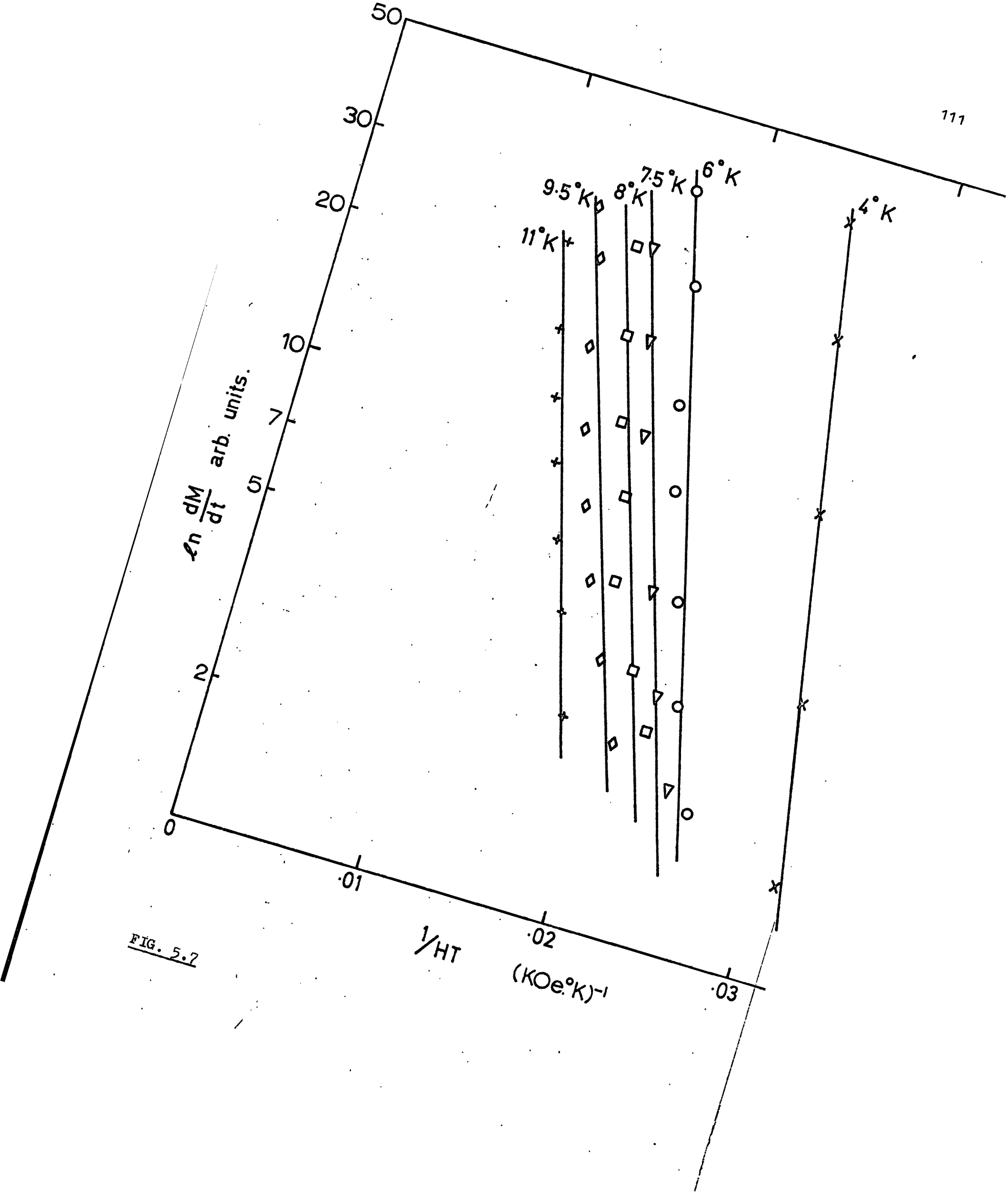
50
30
20
10
7
5
2
0
ln dM/dt arb. units.
9.5°K
8°K
7.5°K
6°K
11°K
4°K
·01
·02
·03
1/HT
(KOe.°K)-1

FIG. 5.7

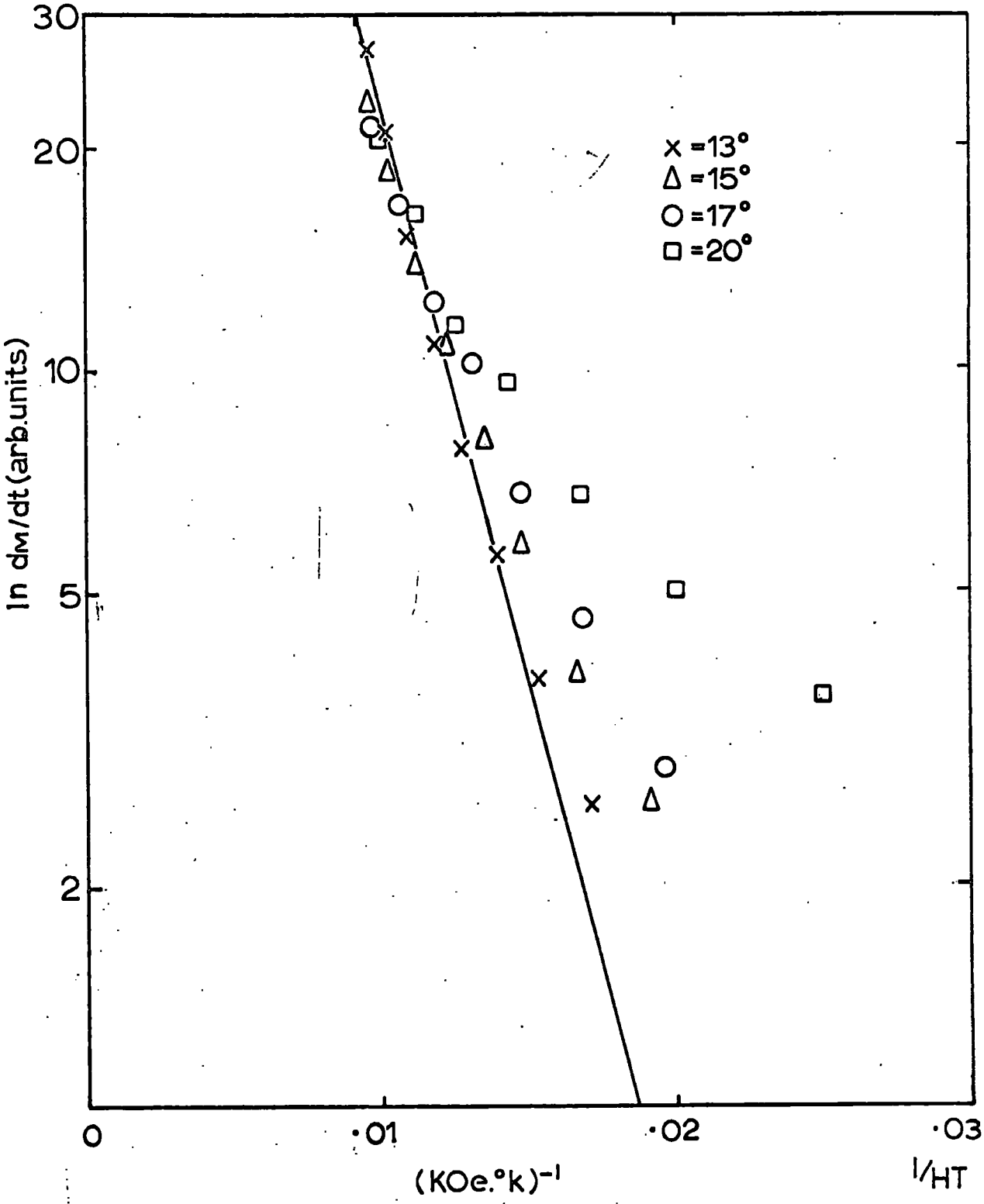

FIG. 5.8

of this effect.

The variation of the potential energy of the wall, V(x), with its position, x, is then given by:-

$$V(x) = \Delta E \sin^2 (\pi x) - 2g\mu_B JHx$$

where $\Delta E \sin^2 (\pi x)$ describes the change in barrier potential with position (following the analogy with the Peierl's force), and the $2g\mu_B JHx$ is the Zeeman energy term.

The new width, x_1, of the barrier in Figure 5.8 may be derived from considering the above equation analytically:-

If we assume the potential of the wall to be zero at $x = x_1$, then:-

$$\Delta E \sin^2 (\pi x_1) - 2g\mu_B JHx_1 = 0$$

Now, if we adopt a hyperbola to describe the shape of the barrier potential so that it is possible to solve the above equation analytically, i.e.,

$$\Delta E \left\{1 - \frac{4}{c^2} \left(x_1 - \frac{c}{2}\right)^2\right\} - 2g\mu_B JHx_1 = 0$$

where c is the lattice spacing, then, solving we obtain:-

$$x_1 = \left\{\frac{4\Delta E}{c} - 2MH\right\} \frac{c^2}{4\Delta E}$$

Therefore, for an applied magnetic field, $H = \frac{2\Delta E}{cM}$, the barrier will have zero width, and therefore the domain wall will be able to move unhindered except for eddy current

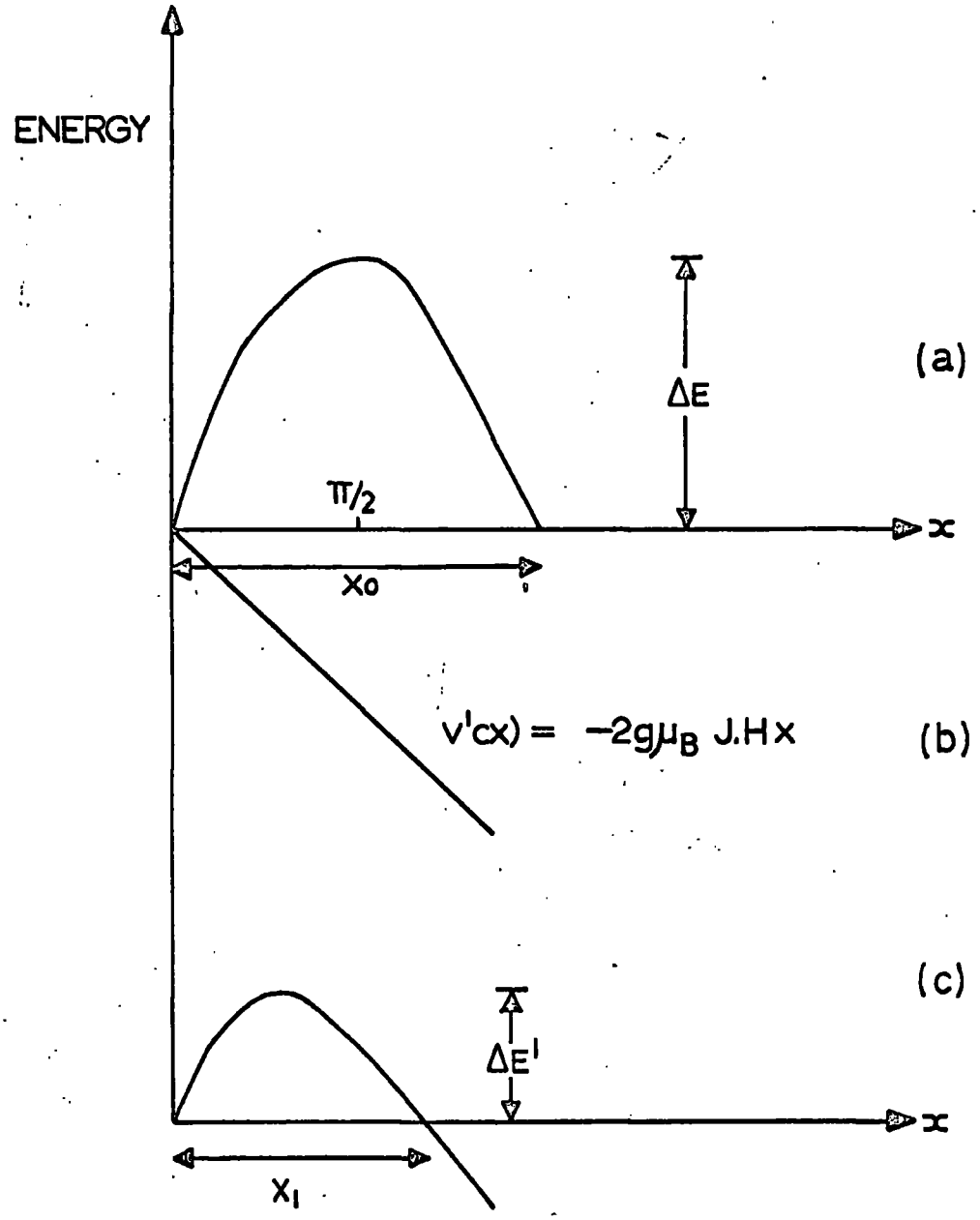

FIG. 5.9

Schematic representation of the change in the barrier potential to domain wall motion with applied field.

damping. Egami(49) has used an audio amplifier to obtain various sweep field rates and has found that for sweep rates above 10^5 Oe/sec the coercive force of pure Dysprosium does reach a maximum value.

Egami has shown that at low temperatures the tunnelling of the domain wall through the potential barrier will increase the domain mobility such that:-

$$\frac{dM}{dt} \propto \exp\left\{ \frac{-50S}{n^{3/2}} \frac{<57^2 J}{(V_1 K_2)^{\frac{1}{2}}} \cdot \left(\frac{H_c}{H}\right)^2 G_{Th}\left(\frac{H}{H_c}\right)\right\}$$

where $G_{Th}\left(\frac{H}{H_c}\right)$ is a function which approaches unity at zero applied field and is zero at $H = H_c$.

The dependence of the magnetisation rate upon the inverse of the applied field squared may be further demonstrated using the simple model in the last section. The probability that tunnelling will take place is proportional to the area of the nucleus:-

$$\text{i.e.,} \qquad \ln P_t \propto r_c^2 \propto \frac{1}{H^2} \qquad \text{see equation 5.4}$$

Figure 5.10 is a plot of magnetisation rate on logarithmic scale against $\frac{1}{H^2}$. As might be expected, if the above dependence holds, the isotherms for the lower temperatures are straight lines, but become more curved as the temperature is increased, even at the higher field values.

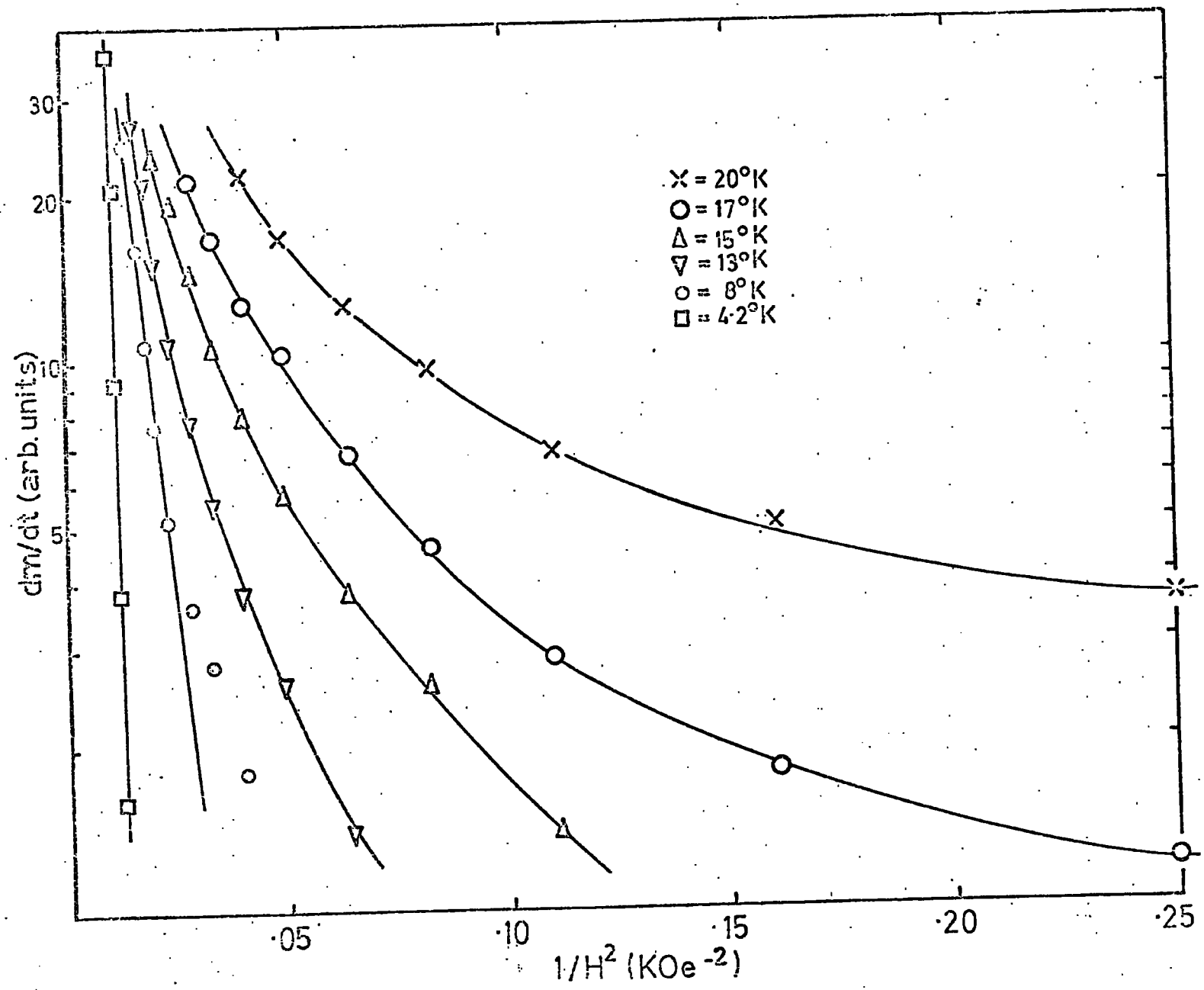
30
20
10
5
dm/dt (arb. units)
·05
·10
·15
·20
·25
1/H² (KOe⁻²)
× = 20°K
○ = 17°K
△ = 15°K
▽ = 13°K
○ = 8°K
□ = 4·2°K

FIG. 5.10

CHAPTER SIX

CONCLUSION

The assumption that the critical field in the pseudo-binary series, $Dy(Co,Ni)_2$ is due to the domain wall being narrow and having to overcome a potential energy barrier before it is able to move seems to be valid.

The success of the theory is demonstrated in the explanation of the variation of critical field across the series (and also the $(Dy_{1-x}Tb_x)CoNi$ series). This has been shown to be caused by the change in the ratio of anisotropy to exchange constants and hence the change in the height of the barrier (following Zijlstra's narrow domain wall theory) across the series.

It is obvious from oscillograms of magnetisation against magnetic field and magnetisation rate against field that the wall is not motionless below the critical field but has a reduced mobility.

From Figure 4.16 the initial mobility of the domain wall is seen to be independent of temperature at low temperatures, i.e., near liquid helium temperature. As the temperature is increased, though, the role of thermal activation of the domain wall becomes more important, after passing through a transition period. This is therefore similar to the case of dislocations bound by the Peierl's potential as suggested, where the creep at low temperatures is temperature independent and governed by tunnelling of the dislocation. Although the domain wall is not a particle in the

normal sense, it does resemble a particle due to the gyromagnetic property of the spins and the tunnelling of the wall through the barrier may be predicted.

Of the two models considered to account for the variation of the mobility of the domain wall at low fields, i.e., less than the critical field, Taylor's model seems to be a better fit to the results obtained. Figure 5.2 shows that the magnetisation rate does appear to increase exponentially with applied field. Further, from Figure 5.4 and equation 5.1, the value of $12\mu_B$ for the molecular moment for DyCoNi is so near to the measured value of $8\mu_B$ that one must consider Taylor's model for thermal activation to be a good one. Egami's model for thermal activation does not compare so favourably with experiment, however. Figure 5.5 shows that the dependence upon the reciprocal of the applied field does not seem to apply at high temperatures but does apply at the lower temperatures. This dependence is predicted by Taylor to account for the change in magnetisation rate when tunnelling is dominant, and would therefore be a better representation for Figure 5.5. Also Barbara et al record the same dependence at low temperatures. However, the dependence of tunnelling upon the increase of the applied field squared proposed by Egami, as shown in Figure 5.9, also seems to be applicable to the results taken at low temperatures.

Perhaps the deviations from the predicted relationships of Egami are due to the small fields considered at those points, since effective field in the kinks will probably be smaller than the applied field. Taking this into account,

it is possible to draw straight lines through the high field points in Figure 5.5 and also this would account for the deviation from the common line in Figure 5.8 at the low fields.

Therefore, although it is not possible to say definitely which is the better model, Taylor's model seems to be a more fruitful representation of the experimental results.

FUTURE WORK

It would be desirable if the work done in this thesis was repeated using single crystal specimens so that parameters such as anisotropy can be measured and hence a definite value of the energy barrier to domain wall motion, ΔE, can be obtained. With a single crystal it would also be possible to use a rotating specimen magnetometer to study the time-dependent mangetisation.

Further work may also be performed on other systems such as the $Tb(Co,Ni)_2$ series adopted in Chapter 4, and perhaps $Ho(Co,Ni)_2$, Dy_3Al_2 and pure Dysprosium to see if the relationships proposed in Chapter 5 hold equally well.

Also measurements of the coercive field for a larger variation of field sweep rates might be taken to investigate their interdependence further, as mentioned in Chapter 5.

APPENDIX A

MAGNETISATION MEASUREMENT

The flux in the M pick-up coil in the presence of a specimen is a result of (a) the magnetic moment of the specimen, and (b) the demagnetising field of the specimen (assuming the contribution of the applied field is removed, as described in section 3.2.3).

To measure the magnetisation of the specimen, however, we must show that the signal from the pick-up coil is independent of the shape of the specimen and is proportional to the magnetic moment, δ, of the specimen.

The contribution to the output of the M coil due to the specimen depends upon the rate of change of the lines of induction due to the specimen. The definition of δ used is:-

$$\delta = \mu_o I.S$$

where I is the current in amperes flowing in an elementary circuit of area, δm^2.

Consider a spherical sample, radius a, of magnetic moment, δ, and uniform magnetisation, M, parallel to the axis of a coil of one turn, radius R, placed concentrically with the specimen.

The flux due to the specimen is given by:-

$$\phi_1 = \int_0^{\pi a^2} B.ds \quad \ldots\ldots\ A.1$$

The demagnetising field inside the spherical sepcimen is given by:-

$$H_D = \frac{-M}{3\mu_o} \qquad \therefore \quad B = \mu_o H_D + M$$

$$= -\tfrac{1}{3}M + M = \tfrac{2}{3}M.$$

Thus equation A.1 becomes:-

$$\phi_1 = \tfrac{2}{3}M \times \pi a^2$$

$$= \tfrac{2}{3} \cdot \frac{\delta}{\frac{4}{3}\pi a^3} \cdot \pi a^2$$

$$= \frac{\delta}{2a}$$

The contribution of the volume round the specimen inside the coil is given by:-

$$\phi_2 = \int_a^R B.ds$$

To obtain a value of the field outside the spherical specimen of moment, δ, one can imagine the entire specimen to be replaced by a small dipole of moment, δ, situation at its centre. We may therefore write:-

$$\phi_2 = -\int_a^R \frac{\delta}{4\pi r^3} \cdot 2\pi r.dr$$

where r is the distance from the centre of the specimen in the plane of the coil.

$$\therefore \quad \phi_2 = -\frac{\delta}{2}\int_a^R \frac{1}{r^2}\,dr = \frac{\delta}{2}\left[\frac{1}{r}\right]_a^R$$

$$= \frac{\delta}{2R} - \frac{\delta}{2a}$$

Thus the total flux, ϕ, is given by:-

$$\phi = \phi_1 + \phi_2 = \frac{\delta}{2a} + \frac{\delta}{2R} - \frac{\delta}{2a} \quad \ldots\ldots\ldots \quad A.2$$

$$= \frac{\delta}{2R}$$

The total flux is therefore independent of the size of the specimen.

This may also be shown by integrating B from the coil to infinity as the lines of flux are continuous and conserved, i.e.,

$$\phi = \int_R^{\infty} \frac{\delta}{4\pi r^3} \cdot 2\pi r \, dr$$

$$= \frac{\delta}{2R}$$

Therefore it has been shown that, despite the demagnetising field, the induced signal in the pick-up coil is a measure of the moment. In fact, it is due to the demagnetising field that equation A.2 simplifies. Although it has only been shown here that this is the case for spherical samples, it is also possible to show, by the calibration experiment outlined in section 3.2.3, that the same applies to non-spherical samples.

APPENDIX B

MAGNETO-CALORIC EFFECT

It can be shown(50) that the change of magnetisation which results from an adiabatic change in applied magnetic field produces a reversible temperature change given by:-

$$T = \frac{-T}{C}\left(\frac{\partial M}{\partial T}\right)_H \cdot \Delta H \quad \ldots\ldots\ldots \text{B.1}$$

Since $\left(\frac{\partial M}{\partial T}\right)_H < 0$ there will be an increase in temperature of the specimen, ΔT, for an increase in magnetic field, ΔH.

C is the Debye specific heat; therefore:-

$$C = 12\,\frac{\pi^4}{5}\,k\left(\frac{T}{T_D}\right)^3 \quad \text{erg/}^\circ\text{K/mol}$$

where k is Boltzmann's constant and T_D is the Debye temperature.

$$\therefore C \sim 12 \times \frac{10^2}{5} \times 1.6 \times 10^{-16} \times \left(\frac{4}{200}\right)^3 \quad \text{erg/}^\circ\text{K/mol}$$

$$\sim 3.0 \times 10^{-20} \quad \text{erg/}^\circ\text{K/mol}$$

Using $M \sim M_s\left\{1 - \left(\frac{T}{T_c}\right)^2\right\}$

where M_s is the saturation magnetisation, and T_c the ordering temperature,

$$\therefore \left(\frac{\partial M}{\partial T}\right) = -2\,M_s\,\frac{T}{T_c^2}$$

$$= -2 \times 6 \times 9.5 \times 10^{-21} \times \frac{4}{(70)^2}$$

$$12 \times 10^{-23} \quad \text{erg/mol/}^\circ\text{K/Oe}$$

Therefore, for an applied field of 100 KOe, substituting into equation B.1,

$$\Delta T \sim \frac{4}{3.0 \times 10^{-20}} \times 12 \times 10^{-23} \times 10^{5}$$

$$\sim 16^{\circ}K$$

APPENDIX C

THE FORM OF THE MAGNETIC FIELD

To derive an equation to describe the magnetic field in a pulsed field magnetometer, the differential equation for the LCR circuit must be solved to give an expression for the current flowing in the circuit.

The differential equation is:-

$$L\frac{d^2i}{dt^2} + R\frac{di}{dt} + \frac{i}{C} = 0$$

With boundary conditions of i being zero and C being charged to a voltage, V, when t = 0 (the instant that the pulse starts) the solution of i is:-

$$i = \frac{V}{L} e^{-\frac{R}{2L}.t} \frac{\sin wt}{w}$$

where $w = \left(\frac{1}{LC} - \frac{R^2}{4L^2}\right)^{\frac{1}{2}}$

for t = 0: $i = i_o = \frac{V}{Lw}$

$$\therefore \quad i = i_o e^{-t\lambda} \sin wt \quad \ldots\ldots \quad C.1$$

where $\lambda = \frac{R}{2L}$.

From equation C.1 we are able to write an expression for the ideal form of the field:-

$$H(z,t) = H_o(z) e^{-\lambda t} \sin wt \quad \ldots\ldots \quad C.2$$

where $H_o(z)$ is the value of H(z,t) at t = 0 at z along the z axis of the solonoid.

REFERENCES

1. Nevitt, M V, 1963, Electronics and Alloy Chemistry of Transition Metals, edited by P A Beck, p 101

2. Westbrook, J H, 1967, Intermetallic Compounds, Wiley

3. Laves, F, 1939, Naturwissenschaften, 27, 65

4. Laves, F, and Witte, H, 1935, Metallwirtschaften, 14, 645; ibid, 15, 840

4a. Van Vleck, J H, 1932, Theory of Electric and Magnetic Susceptibilities, O U P, Chapter 11

5. Ruderman, M A, and Kittel, C, 1954, Phys Rev, 96, 99

6. Kasuya, T, 1956, Prog Theor Phys, 16, 45, 58

7. Yosida, K, 1957, Phys Rev, 106, 893

8. Stoner, E C, 1947, Repts Prog Phys, 11, 43

9. Friedel, J, 1954, Adv Physics, 3, 466

10. Buschow, K H J, 1971, Phys Stat Sol (a) 7, 199

11. Kramers, H A, 1930, Proc Acad Sci Amst, 33, 959

12. Vickery, R C, Sexton, W C, Novy, V, and Kleber, E V, 1960, J Appl Phys, 31, 366S

13. Piercy, A R, and Taylor, K N R, 1968a, J Appl Phys, 39, 1096; Taylor, Adv Phys, 20, 551

14. Wallace, W E, 1964, J Chem Phys, 41, 3857

15. Jaccarino, V, 1961, J Appl Phys, 32, 102S

16. Feron, J L, Lemaire, R, Paccard, D, and Pauthenet, R, 1968, C R Acad Sci, Paris, 267, 371-4

17. Taylor, K N R, and Primavesi, G J, 1972, J Phys F 2, 761

18. Barbara, B, Becle, C, Lemaire, R, and Pauthenet, R, 1968, J Appl Phys, 39, 1084

19. Buschow, K H J, 1969, Phys Letters, 29A, 12

20. Barbara, B, Becle, C, Lemaire, R, and Paccard, D, 1970, Compt Rend, 271, 880

21. Zijlstra, H, and Van den Broek, J J, 1971, I E E E Trans Magn, 7, 226

22. Egami, T, and Graham, C D, 1971, J Appl Phys, 42, 1299

23. Taylor, K N R, Phys Letters, 1971, 35A, 153

24. Barbara, B, Fillion, G, Gignoux, D, and Lemaire, R, 1972, Solid Stat Comm, 10, 1149

25. Taylor, K N R, Melville, D, Primavesi, G J, 1972, J Phys, F 2, 584

26. Egami, T, 1973, Phys Stat Sol B, 57, 211

27. Egami T, not yet published

28. Weiss, P, 1907, J de Phys, 6, 661

29. Bloch, F, 1930, Z F Physik, 61, 206

30. Landau, L, Liftshitz, E, 1935, Physik Zeits Sowjetunion, 8, 153

31. Trammel, G T, 1963, Phys Rev, 131, 932

32. Zijlstra, H, 1970, I E E E Trans Magn, 6, 179

33. Kittel, C, 1949, Rev Mod Phys, 21, 541

34. Döring, W, 1948, Z Naturf, 3a, 373

35. Kittel, C, Galt, J K, 1956, Sol Stat Phys, 3, 439

36. Allain, Y, de Gunzbourg, J, Krebs, J P, and Miedan-Gros, A, 1968, Rev Sci Instr, 39, 1360

37. Allain, Y, Varret, F, Miedan-Gros, A, 1965, Compt Rend, Acad Sci Paris, 260, 4677

38. Allain, Y, Belov, K P, 1961, "Magnetic Transitions" Consultants

39. Weiss, P, Forrer, R, 1929, Ann Phys (Paris), 12, 297

40. Salmans, L R, Strnat, K, Hoffer, G I, Tech Dept, AFML-TR-68-159, 1968

41. Steinhaus, W, Kussman, A, Schoen, E, 1937, Phys Z, 38, 777

42. Becker, J J, 1959, J Appl Phys, 30, 387

43. Gilman, J J, J Appl Phys, 39, 608b

44. Glen, J W, 1956, Phil Mag, 1, 400

45. Mott, N F, 1956, Phil Mag, 1, 568

46. Weertmann, J, J Appl Phys, 29, 1685

47. Miller, A C, and Gabriel, W, 1960, Phys Rev, 117, 1460

48. Zener, C, 1934, Proc Roy Soc (London), 145, 523

49. Egami, T, 1972, A I P Conf Proc, Vol 5, 1457

50. Morrish, A H, Physical Princ of Magnetism, Wiley, 273

TO BE PUBLISHED .....

Field Induced Transitions in Rare Earth Intermetallic Compounds

by

K.N.R. Taylor, J. Hunter and C.A. Poldy

Physics Department,
University of Durham,
England.

Introduction

In the pure rare earth metals the competition of the exchange interaction and the high magnetocrystalline anisotropy is known to lead to a variety of complex magnetic structures in the ordered phase. A similar situation is now being shown to exist in many of the intermetallic compounds, particularly those rich in the rare earth elements.

The strength of the exchange interaction between the rare earth ions is never large, transition temperatures almost invariably being well below room temperature, and usually less than 100K. Consequently it is frequently possible to induce antiferromagnetic-ferromagnetic transitions in those materials with antiparallel spin ordering.

A second type of critical field behaviour has been observed in many of the ferromagnetically ordered materials. This arises, however, as a result of the large energies required to move a domain wall in a material for which the exchange interaction strength is small and the magnetocrystalline anisotropy is large. Trammell (1962) was the first to point out that domain walls would be very narrow under these circumstances and that the normal continuum treatment of domain wall motion would be invalid. Egami (1971), Zijlstra (1970) and Barbara et al. (1971) investigated the situation further and showed that a finite excitation energy would be required for the wall motion and that this would show itself in the form of a large 'intrinsic' coercivity in this type of material. Further, Taylor et al. (1972), showed that in certain materials the magnetization process associated with these walls can occur relatively slowly and give an "intrinsic magnetic aftereffect."

We have recently carried out a series of measurements on various intermetallic phases for which these types of magnetic behaviour are likely to occur as a result of the relatively low ordering temperatures

and high anisotropies. Some of these materials are antiferromagnetic and others ferromagnetic, but in both cases the observed behaviour arises as a result of comparable exchange and crystal field interaction energies.

Experimental

The specimens were all prepared by melting together stoichiometric quantities of the purest metals available. This was done in an argon arc furnace and after a series of homogenizing melts was followed by a lengthy anneal.

The magnetic properties were measured at 4.2K using a pulsed field magnetometer and the ordering temperatures determined from the same measurements or from the use of a permeability bridge.

The specimens studied were the series A_3B (where A = a rare earth and B = cobalt or nickel), $Gd_3(Co,Ni)$, $(Tb,Y)_3Co$, Dy_nCo_m and various pseudo-binaries based on the DyCoNi composition.

The magnetization curves are shown for the A_3B series, the $Gd_3(Co,Ni)$ compositions and the Dy_nCo_m compounds in Figs. 1-3, and their form will be discussed in the following.

Discussion

The form of the magnetization curves of the A_3Co and A_3Ni compounds shown in Fig. 1 clearly represent a wide variety of different magnetic behaviours. The neodymium, terbium, dysprosium and possibly the holmium compounds have open hysteresis loops and it is tempting, in the first instance to assume that these are ferromagnetic materials. Both Gd_3Co and Gd_3Ni however exhibit a clearly defined critical field and it appears that these are both antiferromagnetic.

In order to investigate the two types of behaviour more fully we examined the properties of two series of pseudobinary compounds from this series, namely the $Gd_3(Co,Ni)$ and $(Tb,Y)_3Co$ compositions.

(a) $Gd_3(Co,Ni)$

The magnetization results for these materials, as well as for up to 10% substitution of iron into Gd_3Co, are shown in Fig. 2. As may be seen, the form of the magnetization curve changes progressively from the limiting composition $Gd_3(Fe_{.1}Co_{.9})$ to Gd_3Ni. The critical field progressively increases as the average 3d-electron concentration increases and further the sharpness of the field induced transition is higher near to the cobalt compound.

The behaviour of Gd_3Co has been associated with a metamagnetic spin-flip transition in an antiferromagnetic material for which the exchange interaction between the two sublattices is appreciably smaller than the interaction within a single sublattice. For such a system the critical field strength is given by

$$H_c = \frac{2M}{6}\,\frac{1}{\chi_i} \pm \frac{a}{2M}$$

where M is the sublattice magnetization, χ_i the initial susceptibility and a is an anisotropy term involving the magnetocrystalline and dipolar anisotropies. The $\pm$ signs relate to the direction of easy magnetization relative to the axial lattice parameter. Fig. 3(a) shows the variation of H_c with $1/\chi_i$ for all the compounds studied and it is clear from this that in the cobalt region a spin flip process is adequate to describe the observed results. With increasing nickel concentration, however, the observations deviate markedly from the linear relation and we must look for some other mechanism to account for the observations.

If we use the gradient of Fig. 3(a) to obtain the sublattice magnetization we obtain a value of $5.8\mu_B$ per ion which is somewhat less than the theoretical $gJ = 7\mu_B$ value for a fully aligned sublattice. This value in turn may be employed in the expression $H_c = \frac{nM}{2}$ to obtain n the inter sublattice exchange constant. From the form of the results n clearly increases with increasing 3d electron concentration and it seems likely that the departure from linearity in Fig. 3(a) occurs when the ratio of the intra to inter-sublattice exchange constants ($^{n'}/n$) has become too small for the spin flip process.

Under these conditions, the spin behaviour can be expected to show a change to spin-flop transitions for which

$$H_c^2 = \frac{2b}{3} \frac{1}{\chi_i} \mp \frac{ab}{M^2} \mp \frac{b^2}{M^2}$$

where b is again a term in the anisotropy constants.

As Fig. 3(b) shows, this relation is reasonably well obeyed between $Gd_3(Co_{.75}Ni_{.25})$ and $Gd_3(Co_{.2}Ni_{.8})$ and we assume that the field induced transition in this region is indeed a spin-flop process. As n continues to increase further to the Gd_3Ni composition the ($^{n'}/n$) ratio has become sufficiently small that the Neel treatment is unsatisfactory and agreement with the elementary theory is perhaps not to be expected in this region.

(b) $(Tb,Y)_3Co$

With increasing yttrium composition these materials show a relatively slow decrease of the critical field (intrinsic coercivity?) to approximately 80% yttrium, beyond which it falls quite rapidly (Fig. 4). In contrast the magnetization and ordering temperature fall linearly across the series.

If we take this material to be ferromagnetic at all concentrations and assume that the critical field is due to the presence of narrow domain walls then we can anticipate that the value of the critical field will be given by

$$H_c = \frac{\pi}{aM_s} \Delta E$$

where M_s is the saturation magnetization per unit volume, a is the average spacing between magnetic ions and ΔE describes the energy barrier inhibiting domain wall motion.

Assuming that K/W is large then $\Delta E/K$ will be approximately constant (Van den Broek and Zijlstra 1971) and we can write the critical field as a function of terbium concentration (c) as follows:-

$$H_c = \left(\frac{\pi}{aM_s}\right) \left(\frac{\Delta E}{K}\right) K = \text{const. } c^{1/3}$$

This variation is shown in Fig. 4, normalized to the H_c value at Tb_3Co and it is evident that there is a satisfactory agreement between the experimental and theoretical curves. Consequently it would appear that this material is indeed ferromagnetic but its magnetic properties are affected by the presence of narrow domain walls.

(c) Dy_nCo_m

It is difficult to tell from Fig. 1 the precise nature of the magnetic behaviour of Dy_3Co, although the form of the hysteresis loop is reminiscent of a ferromagnetic material exhibiting a magnetic aftereffect. This comparison is more marked if the Dy_3Co curve is compared with those for the Dy_4Co_3 and $DyCo_2$ specimens shown in Fig. 5, since it is known that the latter specimen does exhibit time dependence at 4.2K. Clearly at $DyCo_3$ any effect of this type has disappeared,

due presumably to the increased exchange interaction W in this compound.

If the critical field values in these materials are also related to the presence of narrow domain walls then we can anticipate that any change in the ratio K/W will affect the critical field strengths.

As shown in Fig. 6, the ordering temperatures increase continuously with increasing cobalt concentration and assuming that to a first order the anisotropy energy is constant in the series then the resulting decrease in K/W is consistent with the change in the critical fields. Interestingly, if we pursue this argument further and assume that the anisotropy in Dy is also at this constant value than the ordering temperature of Dy metal compared to that of the compounds should allow us to predict a value of H_c is dysprosium metal. As shown in Fig. 6 there is a close similarity between predicted and observed values.

(d) $DyCo_2$ Based Compounds

We have already shown elsewhere that the rate of change of the magnetization in Dy $(Co,Ni)_2$ pseudobinaries depends on the applied magnetic field strength (Taylor et al. 1972), and Barbara et al. have established a relation of the form

$$\frac{dM}{dt} \propto \exp^{-Ho}/H$$

to describe this variation.

This effect appears to be related to the excitation energy required for the motion of narrow domain walls and we have named this type of magnetization process the "Intrinsic Magnetic Aftereffect."

In the Dy $(Co,Ni)_2$ series the equiatomic composition DyCoNi has one of the biggest critical field values and the observations showed a decrease in H_c for compositions to either side of this. This was inter-

preted in terms of the changes in exchange and anisotropy in crossing the series. If pseudobinaries of the form (Tb,Dy)CoNi and (Dy,Ho)CoNi are prepared then essentially the same is true. The introduction of Tb into the system increases the exchange but probably leaves K relatively constant, while substitution of holmium decreases both K and W. In both cases the critical field is found to decrease on moving away from the dysprosium compound, and again the changes in the $^{K}/_{W}$ ratio are thought to be responsible.

Figure Captions

Fig. 1 The magnetization curves at 4.2K for the A_3B compound series.

Fig. 2 The composition dependence of the magnetization curve in the $Gd_3(Co,Ni)$ series showing the change in the critical field value. Results are also shown for up to 10% iron substitution.

Fig. 3 (a) The variation of the critical field value with the reciprocal initial susceptibility showing the spin flip transition region near to Gd_3Co.

(b) The spin flop transition region illustrated by the linear relation between H_c^2 and $1/\chi_i$ in the intermediate composition range.

Fig. 4 Comparison of the observed critical field values with a theoretical curve derived for the magnetization process in a specimen containing narrow domain walls.

Fig. 5 The magnetization curves for the Dy_nCo_m compounds.

Fig. 6 The variation of the critical field, ordering temperature and magnetic moment for the compounds represented by Dy_nCo_m.

REFERENCES

Barbara, B., Becle, C., Lemaire, R. and Paccard, D., 1971, J. Phys. C1 299.

Egami, T., 1971, J. Appl. Phys., 42, 1299.

Taylor, K.N.R., Primavesi, G.J. and Melville, D., 1972, J. Phys. F.2, 584.

Trammel, G.T., 1963, Phys. Rev. 131, 932.

Van den Broek, J.J. and Zijlstra, H. 1971, I.E.E.E. Trans. Mag. 7, 226.

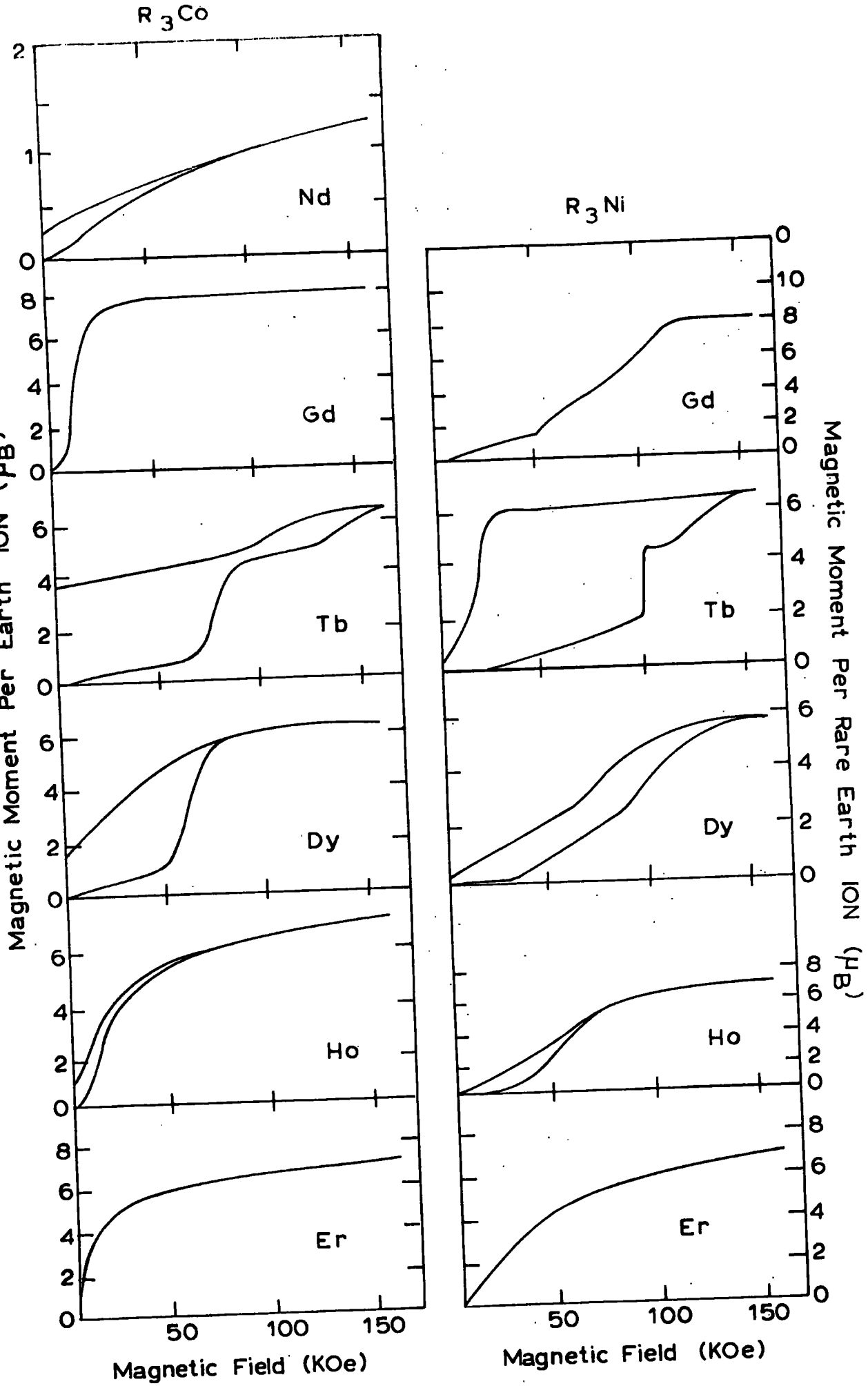
R3Co
R3Ni
Nd
Gd
Tb
Dy
Ho
Er
Magnetic Moment Per Earth ION (μB)
Magnetic Moment Per Rare Earth ION (μB)
Magnetic Field (KOe)
Magnetic Field (KOe)
50
100
150

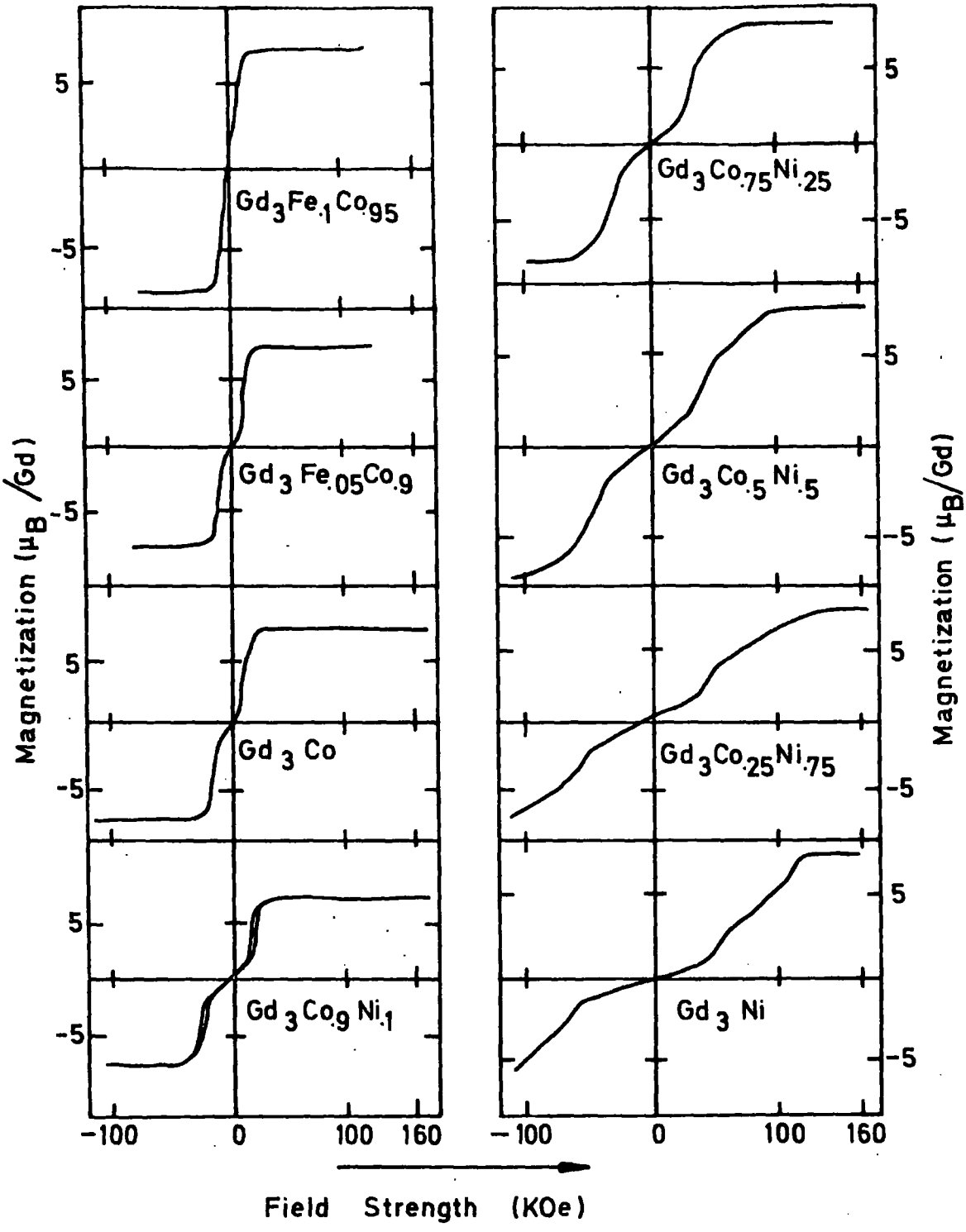
Gd3Fe.1Co.95
Gd3Fe.05Co.9
Gd3Co
Gd3Co.9Ni.1
Gd3Co.75Ni.25
Gd3Co.5Ni.5
Gd3Co.25Ni.75
Gd3Ni
5
-5
-100
0
100
160
Magnetization (μB/Gd)
Field Strength (KOe)

FIG. 2.

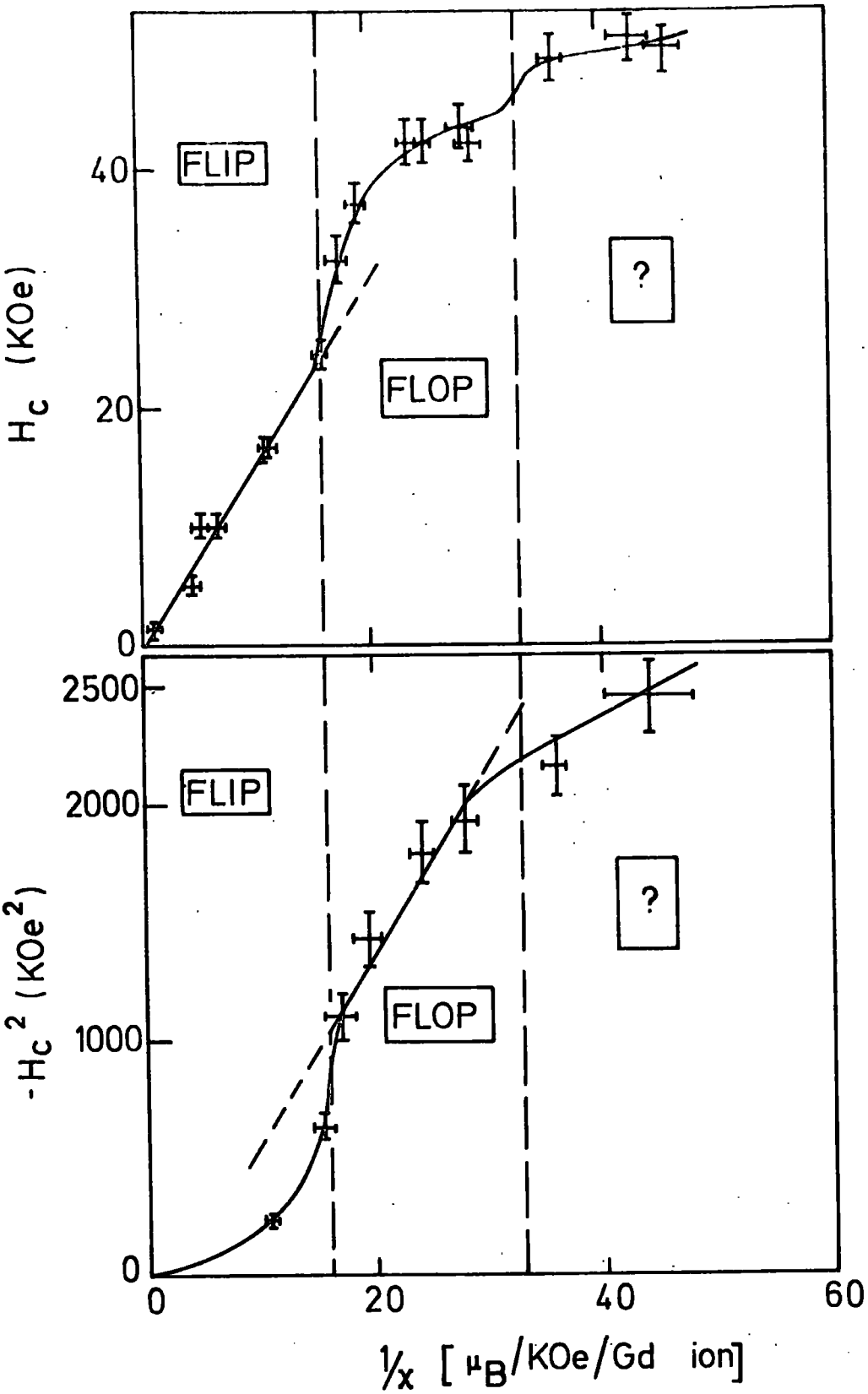
FLIP
FLOP
?
FLIP
FLOP
?
H_c (KOe)
$-H_c^2$ (KOe^2)
0
20
40
60
1000
2000
2500
$1/\chi$ [μ_B/KOe/Gd ion]

FIG. 3

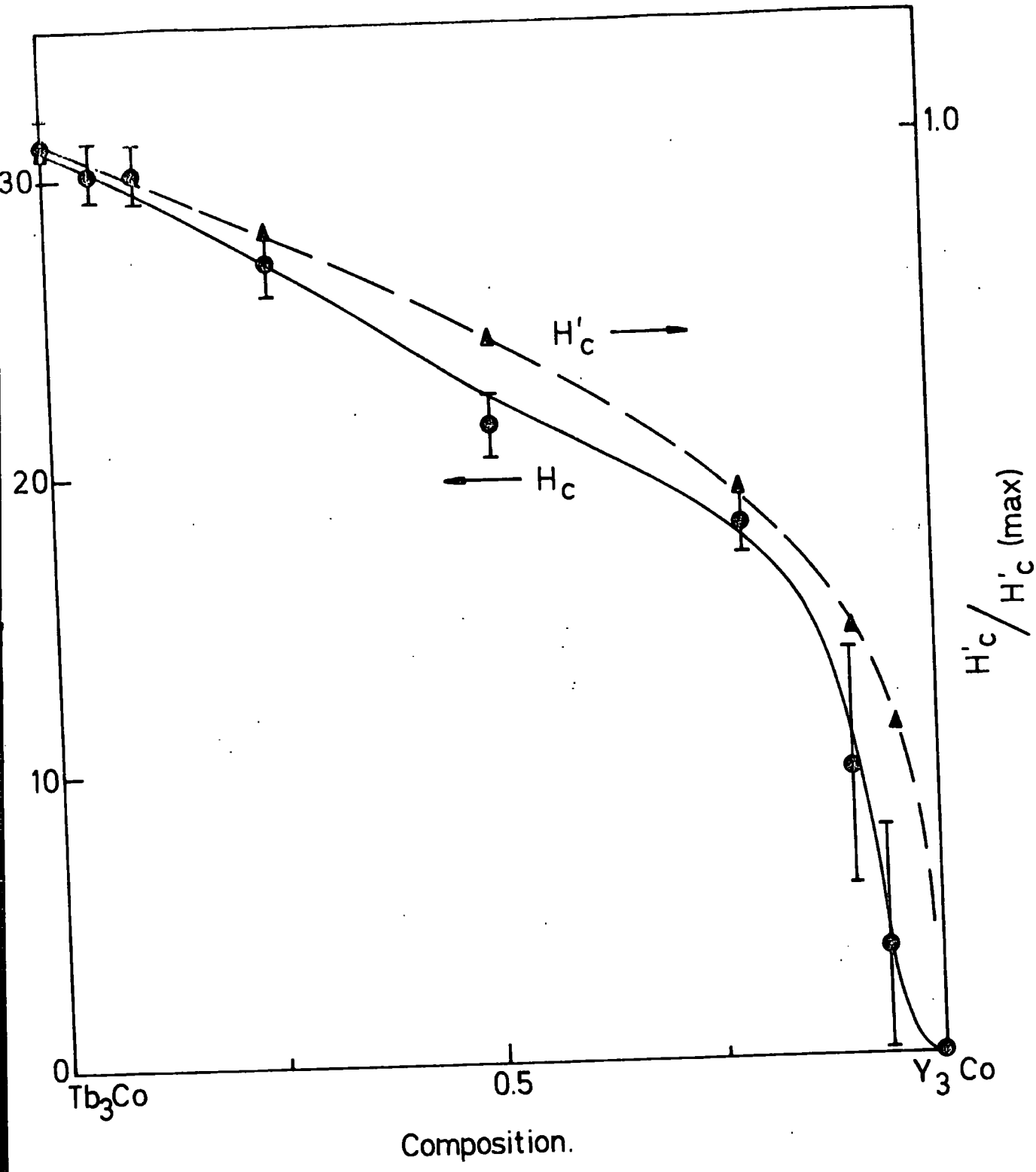

FIG. 4.

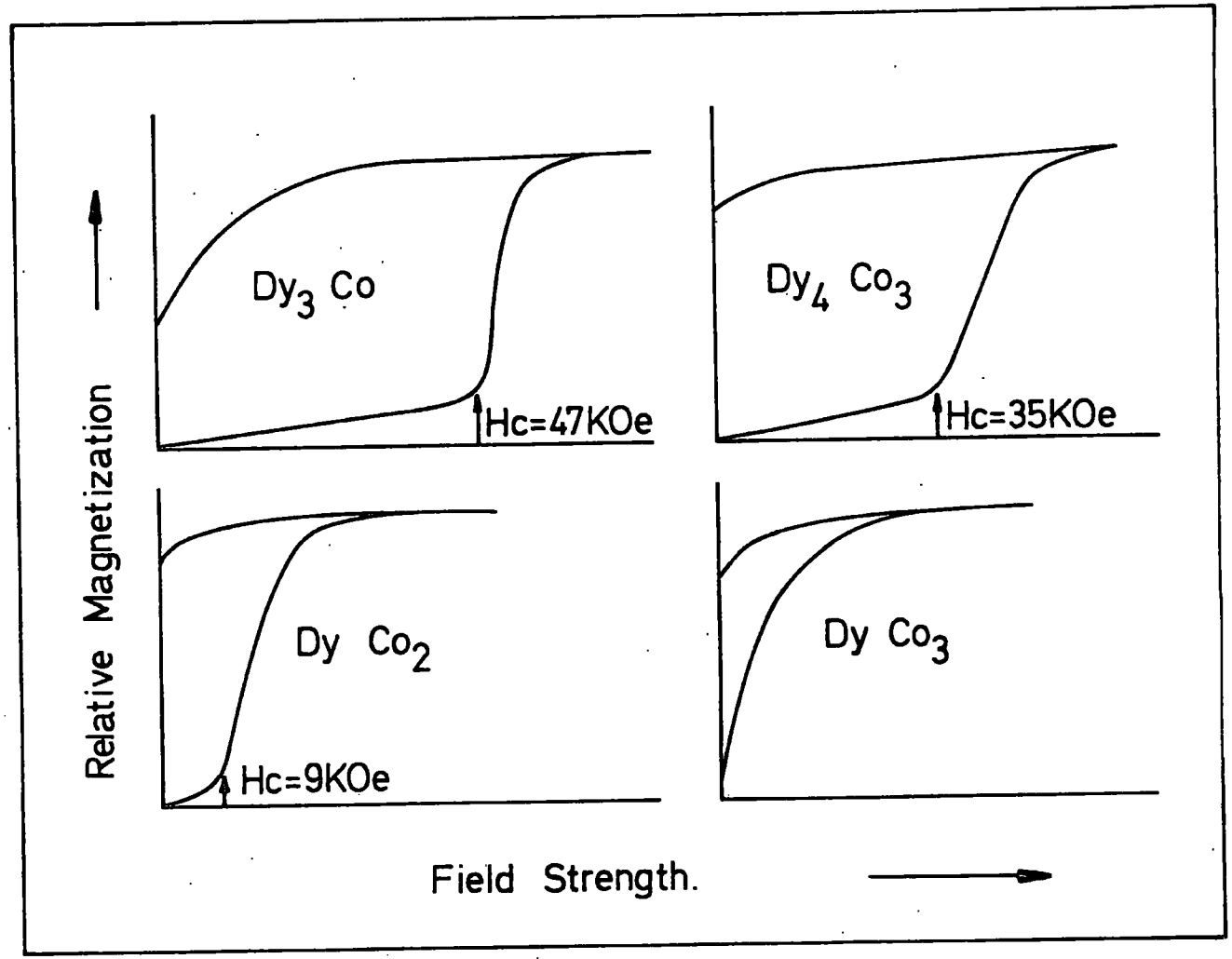
Relative Magnetization
Dy3 Co
Hc=47KOe
Dy4 Co3
Hc=35KOe
Dy Co2
Hc=9KOe
Dy Co3
Field Strength.

FIG.5.

FIG 6